Vapor bubble nucleation, dynamics and heat flux in turbulent Rayleigh-Bénard convection

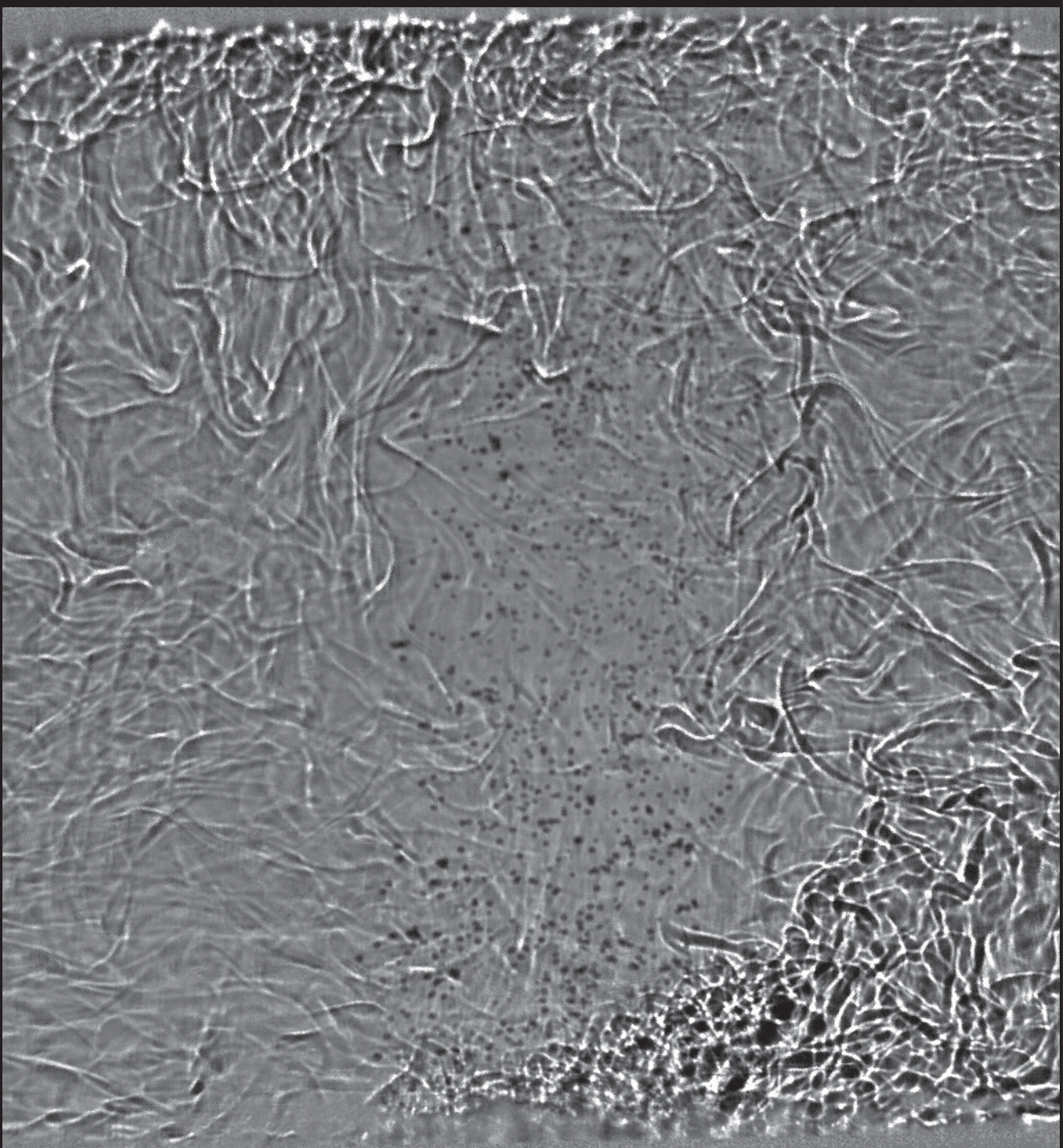

Daniela Narezo Guzmán

Vapor bubble nucleation, dynamics and heat flux in Rayleigh-Bénard convection

Daniela Narezo Guzmán

Comittee members:

Chairman:	
Prof. Dr. Ir. Leen van Wijngaarden	Universiteit Twente
Promotors:	
Prof. Dr. Detlef Lohse	Universiteit Twente
Prof. Dr. Guenter Ahlers	University of California Santa Barbara
Co-promotor:	
Prof. Dr. Chao Sun	Universiteit Twente, Tsinghua University
Members:	
Prof. Dr. Andrea Prosperetti	John Hopkins University
Prof. Dr. Hans J.G.M. Kuerten	Universiteit Twente, Technische Universiteit Eindhoven
Assoc. Prof. Dr. Cees W.M. van der Geld	Technische Universiteit Eindhoven
Prof. Dr. David M.J. Smeulders	Technische Universiteit Eindhoven

The work in this thesis was carried out at Prof. Ahlers Group in the Physics Department of the University of California in Santa Barbara and financed by an European Research Council (ERC) Advanced Grant and by the US National Science Foundation through grant DMR11-58514.

Nederlandse titel: Dampbel nucleatie, dynamiek en warmtestroom in turbulente Rayleigh-Bénard convectie

Cover:
Lateral shadowgraph image of 2-phase turbulent Rayleigh-Bénard convection. The area at the bottom plate where bubble-nucleation occurred is centrally located. The rising bubbles are detectable as dark dots located above the nucleating area and across the cell; the thermal plumes (coherent elongated structures) can be distinguished to be forming the large scale circulation.

Back cover:
Lateral shadowgraph image of 1-phase turbulent Rayleigh-Bénard convection.

Publisher:
Daniela Narezo Guzmán, Physics of Fluids, University of Twente,
P.O. Box 217, 7500 AE Enschede, The Netherlands
pof.tnw.utwente.nl

ISBN: 978-90-365-4015-5

VAPOR NUCLEATION, DYNAMICS AND HEAT FLUX IN RAYLEIGH-BÉNARD CONVECTION

DISSERTATION

to obtain
the degree of doctor at the University of Twente,
on the authority of the rector magnificus,
Prof. Dr. H. Brinksma,
on account of the decision of the graduation committee
to be publicly defended
on Friday the 18th of December 2015 at 16:45

by

Daniela Narezo Guzmán
Born on the 22^{nd} of October 1983
in Mexico City, Mexico

This dissertation has been approved by the promotors:

Prof. Dr. Detlef Lohse

Prof. Dr. Guenter Ahlers

and the co-promotor:

Prof. Dr. Chao Sun

Contents

1 Introduction

Liquid-vapor phase transitions are the core of many technological applications such as power and refrigeration cycles. A very large amount of the world's electrical energy is generated by vapor propelling the turbines in power stations. In addition, the high heat transfer associated to boiling and condensation is widely applied in the design of devices with high energy dissipation rates since these need to be cooled down rapidly. Boiling is an efficient mode of heat transfer, thereby widely used to control the temperature of electronic components in computers or of nuclear reactors. Boiling is also important in space applications [1] because the size of highly dissipative components can be significantly reduced. The development of new technologies for future applications crucially depends on the fundamental understanding of the underlying physical phenomena involved in boiling and thus on its controllability. However this has been hindered because of the complexity of the boiling process.

Boiling refers to a liquid at its saturation temperature which transitions into vapor by applying heat. Boiling differs from evaporation at a vapor/gas-liquid interface as it involves the creation of the interface itself. A full description of a boiling liquid is a complex problem because thermodynamics, fluid dynamics, as well as capillary and wettability phenomena, which vary with liquid and surface properties, come into play.

Pool-boiling refers to boiling at the surface of a body immersed in an extensive pool (pool dimensions are much larger than the bubble length-scale); in this flow convection arises but there is no externally forced flow. In pool-boiling the heat transfer q from the surface where vapor-bubbles form, depends of the temperature of the surface T_w. This dependency is depicted by the so-called boiling-curve [2], as shown in figure 1.1, where the horizontal axis is the difference between T_w and the saturation temperature of the liquid T_ϕ (at the system pressure), known as wall superheat. The details of the boiling curve change if a different liquid or a different surface are considered. The

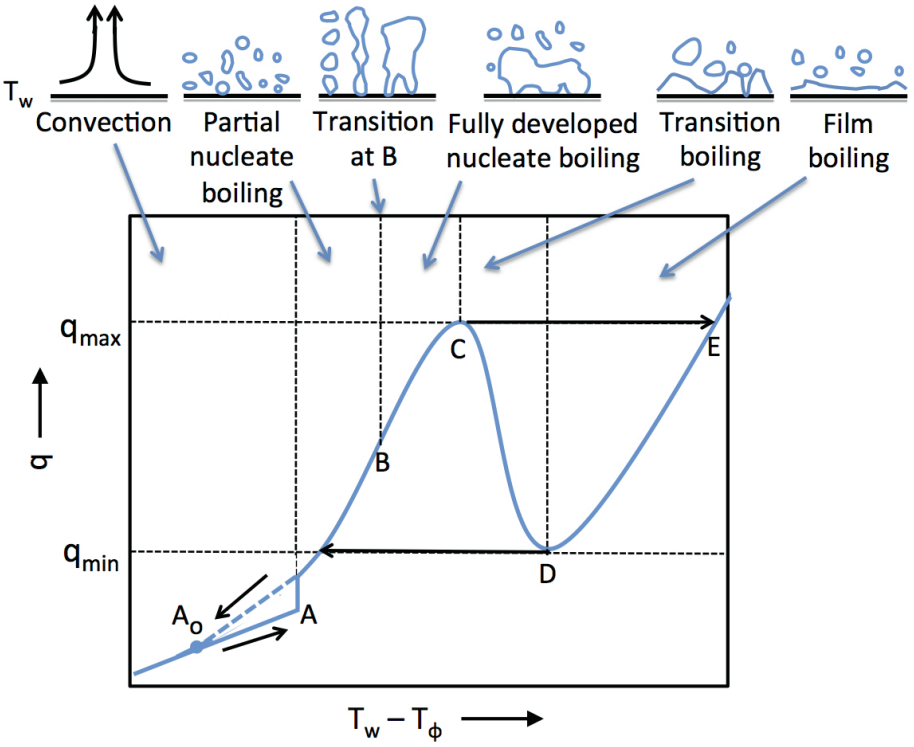

Figure 1.1: Pool-boiling curve of a horizontal surface representing the total heat transfer q from the surface to the flow as the surface temperature T_w is increased (solid blue line) and eventually becomes larger than the saturation temperature T_ϕ of the liquid at the prevailing pressure of the system. The different regions are separated by vertical dotted lines and for each region the surface and the vapor phase are depicted. For increasing $T_w - T_\phi$: (1) left from 'A': convection and conduction are the heat transfer mechanisms. (2) A-B: onset of nucleate boiling at 'A', isolated bubbles. (3) B-C: transition at 'B' - bubbles start merging vertically and horizontally. Large portions of surface covered by vapor. (4) C-D: critical heat flux at 'C' corresponds to q_{max}. Intermittent and unstable vapor regions. (5) D-E: minimum heat flux to sustain film boiling at 'D'. Film boiling is stable, the surface is dry. The horizontal arrows indicate system jumps (in the direction they point to) in case the surface is heat-flux-controlled. Dashed blue line: continuation of the partial nucleate boiling curve when superheat is decreased. In this thesis experiments in the region between 'A_o' and 'A' were measured for both decreasing and increasing superheat (indicated by arrows).

boiling curve in figure 1.1 is that of a horizontal surface, and can be divided into several regions. Natural convection is the first mode of heat transfer apart from heat conduction (region left from 'A'). Since the superheat is increased and becomes large enough, isolated vapor bubbles start forming at the surface at point 'A', referred to as onset of nucleate boiling (for increasing temperature). As the temperature of the surface is controlled, the sudden appearance of this added heat transfer mechanism does not change T_w, but does increase q, which appears as a vertical line starting at 'A'. After inception and for even larger wall superheat, a dramatic increase in q is observed as more sites activate and the nucleation frequency of a site becomes larger (region A-B). A transition at 'B' into the region with fully developed nucleate boiling takes place when the vapor is formed so rapidly that the bubbles start merging with other bubbles in the vertical direction because the bubbles depart from the surface at a very high rate, and also laterally with bubbles from neighboring sites. A further increase in superheat (past 'B') leads to a further increase in q. The rate of vapor generation is so large, that it impedes liquid from touching the surface over significant parts of it, where locally the heat flux is much lower than in the portions of the surface that are in contact with liquid. Because of intermittent dry portions with local small heat transfer, the overall heat flux rate is reduced. The region of fully developed nucleate boiling ends when the maximum or critical heat flux q_{max} of the system is achieved at 'C', where most of the surface is covered by vapor. In most applications the region of interest of the curve is left from 'C', as high heat removal rates at low superheat values are required. Delaying the critical heat flux in order to extend the region of interest is an active topic of research [3; 4].

If the wall superheat is increased beyond the point 'C' the so called transition boiling region (segment C-D) is encountered. It is characterized by a decreasing mean overall heat flux as the superheat increases. In this region rapid and intense fluctuations occur in the local heat flux or in the temperature of the surface (depending on the imposed boundary condition). The fluctuations originate from the unstable dry regions, which exist momentarily at a given location before collapsing, allowing the liquid to rewet the surface. If superheat is further increased the dry regions become more stable and less intermittent, therefore the time-averaged contribution of the dry regions or vapor blankets to the overall heat flux are reduced. The mean value of q thus decreases as $T_w - T_\phi$ increases until the point with minimum heat flux q_{min} is achieved, indicated by 'D'. If this trend is further continued, eventually the surface becomes hot enough to sustain a stable vapor film on the surface (for an indefinite time) and the entire surface is blanketed by a vapor film, thus making the transition to the film boiling region (segment D-E). In this region q monotonically increases as superheat becomes larger, as consequence of the increased conductive and convective heat transport across the vapor layer.

The boiling curve for a surface subjected to uniform and controlled q generally differs from the one discussed until here, obtained by temperature-control. For temperature-controlled and heat-flux-controlled boiling the curves look rather similar in the regions left from 'C', i.e. before the critical heat flux is achieved. When q is controlled and kept constant beyond 'C', the surface temperature increases because it is thermally isolated from the liquid by the vapor layer. The system transitions rapidly from 'C' to 'E' (indicated by an arrow), where film boiling is stably sustained.

Hence the system does not encounter the transition boiling region. Beyond point 'E' the boiling curves controlled by either parameter follow the same curve. Now, by reducing q the E-D segment can be followed, where 'D' corresponds to the minimum q that can sustain film boiling. As q is further decreased, the system rapidly transitions through the region D-C and returns to the nucleate boiling region (indicated by an arrow) before further reduction of q can be accommodated.

The boiling curves for increasing and decreasing superheat differ near the onset of nucleate boiling. If superheat is decreased towards 'A' and past it, the nucleation sites may remain active below the superheat required for the onset of nucleation (found when superheat is increased). In this way the boiling curve simply follows the nucleate boiling curve until it meets the convection curve (at '$A_\circ$').

In this thesis, the region left from 'A' was experimentally investigated by means of a temperature-controlled surface. By decreasing the surface temperature the continuation of the nucleate boiling curve (dashed blue line in figure 1.1) was accessed. Once '$A_\circ$' was reached and all nucleation sites were inactive, then the surface temperature was increased again before reaching 'A'. By comparing the boiling curve in the convection regime with the curve representing the continuation of nucleate boiling, the difference in q between them was computed. The formation of bubbles modified several aspects of the convective flow, including q, which is the subject of study of the present work. The experiments presented here were performed in a Rayleigh-Bénard (RB) convection cell, which is described below.

1.1 Bubble nucleation

The liquid-vapor phase change involved in the nucleation of a bubble is explained by thermodynamics. In general, thermodynamics studies the macroscopic properties of a system, which have a well defined value at each point in space. At a molecular level, thermodynamical properties fluctuate due to the random motion of the molecules. These fluctuations play a key role in phase stability and phase transitions [5]. Usually it is assumed that the liquid-vapor phase transition occurs at the equilibrium saturation conditions. However in real systems a liquid can be *superheated*, that is, be at a temperature larger than the saturation temperature T_ϕ, without a phase-change occurring [6]. In figure 1.1 such a superheated is depicted left from 'A' for the case when the surface superheat is increased. In such case the system is in a non-equilibrium condition or in a metastable state. As the system enters deeper into the metastable range the density and energy fluctuations in the liquid augment, and the chances that a perturbation will initiate a phase change increase. In a superheated liquid, density fluctuations may exceed the limits consistent with the liquid phase, resulting in localized regions where the molecular density is as low as that of the saturated vapor. It is due to these large fluctuations that small embryo vapor-bubbles can be initiated within the liquid, overcoming the energy penalty involved in the formation of an interface. Bubble nucleation in the bulk of a liquid volume is called *homogeneous nucleation*. For water at atmospheric pressure, homogeneous nucleation occurs at a superheat of about 120 K [7].

In daily life homogeneous nucleation is rarely observed because it occurs at very

large superheat values. We are more familiar with the formation of vapor bubbles at a hot surface like when we boil water in a pot, known as *heterogeneous nucleation*. Most real surfaces, as the bottom of a pot in our kitchens, are not smooth but have scratches, small cavities, etcetera, of sizes that vary from microscopic to macroscopic. In many situations, this type of surface imperfections or manufactured cavities on a surface can trap bubble embryos and act as nucleation sites. Furthermore, dust particles or other type of solid impurities in the liquid can also serve as nucleation sites. The energy penalty that comes with the formation of the liquid-vapor interface in the interior of a cavity is smaller than the one required for homogeneous nucleation, only achievable through large enough density fluctuations. Thus bubble formation can start at superheats much lower than those in homogeneous nucleation. The capacity of a cavity to trap gas and vapor, and house a bubble embryo depends on the specific liquid-solid receding and advancing contact angles, as well as the cavity shape and size [2; 7]. One expect that if the liquid wets the surface well, then the number of trapped bubble embryos is smaller than for a partially wetting liquid.

In both homogeneous and heterogeneous nucleation, an embryo bubble can either grow and become a bubble or collapse, and this will depend on several factors [2; 8–10]. In a simplistic view, the relative number of molecules in the gas phase is determining in this process. The gas phase is constituted by vapor and possibly by other gases as well (typically air). The number of vapor molecules in the embryo bubble can diminish due to condensation or increase due to evaporation at the bubble interface. The amount of gas molecules other than vapor depends on the relative concentration of the same gas in the surrounding liquid, on the partial pressure of the gas inside the bubble and on the coefficient of the Henry's Law, which in turn depends on temperature. A bubble embryo will grow if the expanding force of the pressure exerted by the vapor (and other gases, if any) can overcome the collapsing forces associated to both pressure exerted by the liquid at the interface and by the Laplace pressure, caused by the liquid cohesion forces at the interface, i.e. the surface tension.

Bubble nucleation depends on liquid and surface properties: surface landscape or roughness [11], wettability [12–14], surface tension, contact angle and contact line effects. Moreover, dissolved air in the liquid facilitates the initial nucleation process, thereby reducing the saturation temperature of the (degassed) liquid [15; 16]. Furthermore, bubble nucleation is also affected by flow velocity, system pressure, gravity and thermal properties of the surface, adding on to the complexity of the problem. The reviews in references [2; 17] provide an overview of the several parameters affecting vapor-bubble nucleation and wall heat flux in pool-boiling.

Bubble nucleation on a regular surface (no special surface treatment) takes place at random surface imperfections of different shapes and sizes; the number of sites actively nucleating becomes larger when the heat flux at the wall or when the wall superheat increase [15; 16; 18]. More nucleation sites in turn imply a larger heat flux from the surface and, because of that, varying these two parameters independently and disentangling this two effects is difficult when using a regular surface. Therefore a great simplification for the study of heat flux and other phenomena associated to heterogeneous bubble nucleation was achieved with the introduction of surfaces that have a controlled number of shape-designed cavities, which serve as nucleation sites. Typically, the sizes of the cavities are in the micrometer range and they are etched

into a silicon substrate [19–22]. These type of surfaces enabled well-controlled boiling conditions in the experiments presented in this thesis.

1.2 Bubble dynamics and heat transfer mechanisms

So far, the complexity of bubble nucleation at superheated surfaces has been explained. In this section the dynamical and thermal aspects of vapor bubbles in a liquid flow are discussed, as well as the different heat transfer mechanisms associated to such a flow.

Let us consider a single bubble that after inception continues to grow at a nucleation site. The bubble is immersed in the thermal boundary layer (BL) region adjacent to the superheated surface and surrounded (at least partly) by superheated liquid. The three mechanisms through which heat is attained for the growth of the single bubble are: microlayer evaporation (which assumes the existence of a thin liquid layer between superheated wall and growing bubble), three-phase contact line evaporation and heat transfer through the bubble cap (available from the superheated liquid around the bubble). A review on a myriad of both experimental work and proposed models to account for each of these mechanisms is found in ref. [23]; the results indicate that a bubble grows by obtaining the majority of the required latent heat through the bubble cap.

In the initial, or latent, bubble growth stage of a spherical bubble immersed in stagnant and uniformly superheated liquid, the radial velocity of the liquid-vapor interface is limited by the restraining effect of surface tension, nevertheless this limiting factor becomes less important as the bubble grows. If enough heat is available from the superheated liquid around the bubble, then the limiting factor of growth becomes the liquid inertia [24]. The inertia-controlled stage is followed by an intermediate one, in which both thermal and inertial effects are important. As the bubble grows bigger, the heat available for further vaporization might get depleted. In addition, the pressure inside the bubble becomes very close to the one outside it because the Laplace pressure becomes negligible. In that case the heat transfer at the interface becomes the limiting growth factor and the growth is said to be thermally controlled [25; 26]. If the thermally controlled growth (or asymptotic growth) of a bubble has a large enough growth rate, the temperature and hence the pressure in the bubble drop due to the latent heat required for evaporation. Then the temperature difference between superheated liquid and bubble wall is sustained across a liquid layer that corresponds approximately to the thermal boundary-layer thickness around the bubble. In this case the rate of heat flow in the liquid to the bubble wall is balanced by the latent heat required to supply the vapor in the bubble at the saturation temperature [25; 26]. The growth stages described are only valid for sufficiently large liquid superheats [24]. For smaller superheats, the later stage of growth might be controlled by both inertial and thermal effects. For even smaller superheats the latent stage might be directly followed by the asymptotic stage.

The most simple force-balance determining bubble detachment only considers surface tension opposing the effects of bubble buoyancy. Under this circumstances and neglecting thermal effects, the model in [27] predicts the maximal volume of a spher-

ical bubble before detachment given the contact angle between the bubble and the surface; see ref. [22] for a recent experimental validation of this model. However, if the liquid adjacent to the bubble has a bulk motion, then drag and lift forces may also act towards bubble detachment [28]. Additionally, the shape of the bubble as well as the heat flux rate, which depends on the wall superheat, can affect the bubble release process [29; 30]. The departure diameter of nucleating bubbles has been a matter of study for over 70 years and a handful of predicting models with different success levels exist, an extensive review can be found in [31].

Once a bubble detaches, liquid from both the bulk flow and the surrounding superheated layer fills the vacant volume. The thermal BL adjacent to the wall regrows by conducted heat made available through the surface, a process known as *transient conduction*. The bubble also perturbs the thermal BL as it grows, which results in energy transfer by so-called *microconvection*. The vorticity in the wake of a detaching bubble generates a high mixing zone [32], which can cause additional microconvection. It is the disrupted thermal BL (consequence of bubble growth and detachment) that has been found to be responsible for a large majority of the total heat transferred from the wall by an isolated bubble [23].

The latent heat content of a bubble is reflected in its volume (given the prevailing pressure and temperature of the system). The maximal volume that a bubble can attain before departing from the superheated surface is proportional to the amount of heat that will be transported by advection once the bubble detaches. Further, if after the detachment of a bubble, a new bubble forms at the same site and this process is perpetuated, then the heat per unit time transferred from the surface to the nucleation site, is determined by both the volume and the frequency of detachment [33].

Once free to rise (due to buoyancy) the bubble can grow or shrink, depending on whether the temperature of the liquid it encounters is larger or smaller than the saturation temperature. Condensation differs widely from bubble growth [34]. The main differences are that in condensation, the bubble surface and the outer boundary of the bubble thermal BL move in opposite directions. Additionally, the ratio between bubble area and volume increases more and more in condensation while it becomes smaller and smaller when the bubble grows. These two reasons make condensation much harder to describe than bubble growth.

Liquid inertia and heat transfer between the bubble and the liquid are the most influential factors determining the time evolution of the bubble radius [25; 35], but even in this simplified situation there is a complex interplay between fluid dynamics and heat transfer. When the bubble is not at rest, the heat transfer is influenced by the velocity field and net hydrodynamic forces on the bubble play an important role. The particular case of a bubble with varying size implies additional dynamical aspects with respect to particles of fixed shape, such as the effect of added mass which is not only affected by the relative acceleration but also by the rate of volume change [36]. Similarly, a bubble of a given volume that undergoes shape oscillations presents velocity variations due to the oscillating added mass [37]. Other hydrodynamic forces that are considered in the description of a displacing bubble include viscous drag and buoyancy [34; 38–41]. Furthermore, the drag force experienced by a bubble is augmented if its shape deviates from spherical when flattening in the direction

perpendicular to its motion [42].

Of particular interest here is the condensation of rising vapor bubbles (i.e. in the presence of a mean flow), as encountered in the Rayleigh-Bénard convective (RBC) flow studied in this thesis, in which a very large temperature drop prevailed across the thermal BL of the superheated surface such that the liquid temperature past the thermal BL, i.e. in the bulk flow, was below the saturation temperature. The fate of the vapor bubbles condensing in the bulk was determining in the advection of heat across the flow, and with their buoyancy, the effective buoyancy of the flow was enhanced, together contributing to the heat flux transfer in the RBC flow.

So far the growth and dynamics of a single bubble have been discussed. However in most real boiling situations, there are many nucleation sites close to each other and they are no longer isolated and independent from one another. The interactions between neighboring nucleation sites can be of different nature: hydrodynamical, thermal or through bubble coalescence [43; 44]. The degree to which each of these interactions influence bubble growth, departure frequency and size, and thus heat transport from the surface depends on the distance between the sites, the thermal and geometrical properties of the surface (e.g. a thicker heated surface has a larger heat capacitance than a thinner one of the same material), and the physical properties of the liquid such as viscosity and thermal dissipation coefficient. Therefore these interactions are found to be highly dependent on the specific conditions and more research is necessary to achieve a broader understanding.

1.3 Rayleigh-Bénard convection and heat transport

Buoyancy driven convection originates from an unstable density gradient, which is established by either a temperature or a concentration field or a combination of both [45]. Thermally driven convection is the process in which a source of heat drives a fluid flow so that the lighter hot fluid rises due to buoyancy and heavier cold liquid sinks. In the atmosphere, convection drives local winds and on a larger scale, the atmospheric circulation. The patterns of the atmospheric circulation, in turn, shape the landscape of our planet. The tropical or Hadley cell drives rising warm air near the equator; as this air cools down it sinks at roughly 30° latitude [46] and precipitation follows, giving rise to the world's major tropical rain-forests. Convection is key in the ocean large-scale circulation [47], where the thermohaline circulation is driven by global density gradients created by surface heat and fresh-water fluxes. Thermally driven flows are ubiquitous in nature and also in technological applications.

Rayleigh-Bénard (RB) flow is an idealized system that enables the study of fundamental aspects of thermal convection. Furthermore, RB flow was crucial for the study of pattern formation and spatial-temporal chaos [48; 49], and it was critical in the development of stability theory in hydrodynamics [50; 51]. RB convection consists of a flow confined between parallel plates, where the bottom plate is heated and the top one is cooled. RB convection is a system with well defined boundary conditions, and is described by the Navier-Stokes equations, which makes it well suited for theoretical and numerical studies. Moreover, it is experimentally accessible over a wide parameter space thanks to its simple geometry. RB convection is the classical flow to study

thermally driven turbulence: beyond a particular temperature difference (or thermal forcing) across the flow, the heated fluid rises and the cold liquid sinks, forming convection cells; if the temperature difference is further increased the well-defined cells become turbulent. Examples of turbulent convection are found in the outer core of the Earth and planets [52; 53] and in the outer layer of the sun [54; 55].

The large scale dynamics of turbulent RB flow in a sample with height equal to its diameter, is characterized by a single convection role subject to vigorous small scale fluctuations, known as *large scale circulation* (LSC). This flow structure implies that hot fluid rises on one side of the sample, while cold fluid sinks on the opposite side of it. At the sample boundaries there are viscous or kinetic boundary layers (BL) across which the fluid velocity decreases in order to meet the no-slip condition at the walls. At the bottom and top plates there are thermal BL and across these most of the temperature difference, to which the sample is subjected to, occurs. The thermal BL play a key role in the heat transfer and kinetic boundary layers provide viscous dissipation to the LSC. Another feature of the flow are thermal coherent structures known as *plumes*, which detach from the BL and contribute to the driving of the flow.

There is an extensive number of studies on turbulent RB convection; the reviews [56–60] provide a comprehensive summary of these works. Many of the studies have focused on the *heat transport* across the RB sample as the response of the system to thermal forcing given a certain geometry and fluid properties. The unifying theory of scaling in RB convection, the Grossmann-Lohse theory [61–64], relies on decomposing the flow in BL and bulk contributions, and on exact global, volume averaged, balances for the thermal and kinetic energy-dissipation rates in the system. The theory is well confirmed by experiments and numerical simulations.

In the great majority of studies on RB convection, the flow was kept far from a liquid-vapor phase transition. In this thesis the opportunity that this system offers to achieve fundamental understanding on the fluid dynamics and heat transfer of boiling, as an additional heat transfer mode, was exploited. Boiling RB flow was experimentally investigated under well-defined and controlled conditions. Moreover the contribution of the latent heat required for bubble growth at the surface was quantified.

1.3.1 Vapor-bubble nucleation in Rayleigh-Bénard flow

Having discussed vapor bubble nucleation, growth, thermal evolution and dynamics of bubbles after detachment, as well as the main features and the heat transfer mode due to convection in a turbulent RB sample, in what follows we consider what is called boiling RB flow. The later refers to a 2-phase flow originating from the heterogenous nucleation of vapor bubbles on the bottom plate. If the temperature of the top plate is set to a temperature below the saturation temperature, then boiling can be sustained in the cell, i.e. the sample remains nearly full with liquid except for the bubbles, and the system reaches statistically stable states.

The pioneering work in [65] explored turbulent 2-phase RB convection. The temperature difference across the cell spanned the liquid-vapor coexistence curve of the working fluid, and the pressure in the system was regulated and kept constant. In the parameter range where the mean temperature between top and bottom plates

remained below the saturation temperature, the effective thermal conductivity of the flow was enhanced with respect to the convective 1-phase flow by up to one order of magnitude. It was also reported that the heat flux measurements were not reproducible from one run to another for low superheat values and became reproducible but time-dependent for larger superheats. The irreproducibility could be linked to the random size and shape of the nucleation sites at the bottom plate, some of which activated or did not depending on the history of each run. For example a run measured after the system had been highly pressurized could have led to deactivation of sites, which for a run with a different history would have been active. The finding that at higher superheats the runs were reproducible could have been related to having surpassed a critical superheat (given the pressure in the system) beyond which all nucleation sites of a certain characteristic size, independent of the history of the run, became active. As will be shown in this thesis, the irreproducibility of boiling RB flow can be overcome by using bottom plates with designed cavities.

Boiling RB flow has been numerically simulated in recent years [66–71]. The simulations consider RB convection as the reference flow and compare several aspects of it with the 2-phase flow. These aspects comprise flow structure, thermal and kinetic dissipation rates, temperature and velocity fields and their fluctuations, as well as the intermittency of the thermal field. A key finding is the heat transfer enhancement of the boiling flow. Because the bubble nucleation and detachment from the bottom plate are such complex processes, the numerical simulations do not include them, but deliberately generate micron-sized bubbles next to the bottom plate, which are free to rise. Therefore, the heat transfer computed in the simulations does not account for the necessary heat to grow the bubbles to their initial size. Instead, the heat flux enhancement is due to the augmentation in both effective flow buoyancy and strength of the flow circulatory motion caused by the rising bubbles.

Whereas the heat transfer and the extent of turbulence of (1-phase) RB convection can be described in terms of thermal forcing, physical properties of the working fluid and flow geometry; in boiling RB convection there are additional modes of heat transfer that are determined by the bubble nucleation process and the intertwined thermal and hydrodynamical effects on the rising bubbles. The heat transfer in 2-phase turbulent RB convection has three main contributions: heat advection by bubbles and by the enhanced effective flow buoyancy, latent heat for the growth of bubble embryos at the superheated surface, and processes next to the superheated surface occurring as a consequence of bubble growth and departure from it, i.e. microconvection and transient conduction.

1.4 In this thesis

The experimental work on 2-phase RB convection presented in this thesis focuses on the turbulent flow when vapor bubbles nucleated at the superheated bottom plate and condensed as they rose across the flow that was kept at constant (hydrostatic) pressure. Measurements of the 1-phase flow under the same thermal forcing, i.e. with delayed bubble nucleation, were considered as the reference flow. In that way, the modifications to the 1-phase flow due to the presence of vapor-bubbles were studied

under the same temperature boundary conditions. The RB sample used in all experiments was cylindrical and its diameter equaled its height. The bottom plate upper surface consisted of a silicon wafer with cylindrical micron-sized cavities etched in a triangular pattern. The circular etched area was centrally located on the wafer and was about 15 times smaller than the top and bottom plate surface. Therefore the flow studied here deviated from classical RB flow, in which the entire bottom plate is heated and its surface area equals the one of the top plate. The deviation from classical RB flow was implemented in order to avoid uncontrolled nucleation observed in preliminary experiments that took place at the edge of the cell, where the small gap between the cell and the bottom plate provided many nucleation sites.

Chapter 2 focuses on the heat transfer: for a given bottom plate superheat the heat flux in 2-phase flow was larger than for the 1-phase case, the difference between them equaled the heat flux enhancement due to the presence of vapor bubbles in the flow. As the bubbles rose, they interacted thermally and mechanically with the flow, which was reflected by the statistical properties of local temperature measurements in the bulk flow. Several correlations between heat flux enhancement and temperature modifications in 2-phase flow were found. Heat flux enhancement and temperature modifications were investigated as a function of two independent parameters: superheat and cavity density. By placing a short ring around the area with active nucleation sites, the influence of the LSC on the nucleation process and its impact on the heat flux enhancement was investigated. Furthermore, when a cylinder nearly as tall as the sample was fixed around the etched area, it partially isolated the nucleation sites and the liquid column above the heated area from the rest of the flow. The effect of this thermal isolation on the heat flux enhancement was also explored.

Chapter 3 consists of quantitative and qualitative results obtained from high-speed flow visualization using different techniques and two different apparatuses. The first one was used for visualization of the nucleating sites through the top plate and to obtain precise heat transfer measurements. The second apparatus was specifically designed for lateral visualization of the flow. Analysis of the top view image sequences enabled to obtain bubble departure frequency from the bottom plate, as well as the bubble size at departure for three different cavity densities and for different degrees of superheat. Side visualization showed that bubbles at departure were not spherical and their volume was obtained. Knowing volume at departure and departure frequency revealed the amount of latent heat content in departing vapor bubbles per unit time. The contribution to the total enhancement of heat transfer due to vapor bubble formation was computed. Side-view shadowgraph recordings captured the large scale flow dynamics of 1- and 2-phase flow. Moreover, single bubbles were tracked along their rising paths; time-evolution of their size and both vertical and horizontal velocity components were obtained and found to be influenced by the LSC.

2

Heat-flux enhancement by vapor-bubble nucleation in Rayleigh-Bénard turbulence *

We report on the enhancement of turbulent convective heat transport due to vapor-bubble nucleation at the bottom plate of a cylindrical Rayleigh-Bénard sample (aspect ratio 1.00, diameter of 8.8 cm) filled with liquid. Microcavities acted as nucleation sites, allowing for well-controlled bubble nucleation. Only a central part of the bottom plate with a triangular array of microcavities (etched over an area with diameter of 2.5 cm) was heated. We studied the influence of the cavity density and of the superheat $T_b - T_{on}$ (T_b is the bottom-plate temperature and T_{on} is the value of T_b below which no nucleation occurred). The effective thermal conductivity, as expressed by the Nusselt number Nu, was measured as a function of the superheat by varying T_b and keeping a fixed difference $T_b - T_t \simeq 16$ K (T_t is the top plate temperature). Initially T_b was much larger than T_{on} (large superheat), and the cavities vigorously nucleated vapor bubbles, resulting in 2-phase flow. Reducing T_b in steps until it was below T_{on} resulted in cavity deactivation, i.e. in 1-phase flow. Once all cavities were inactive, T_b was increased again, but they did not re-activate. This led to 1-phase flow for positive superheat. The heat transport of both 1- and 2-phase flow under nominally the same thermal forcing and degree of superheat was measured. The Nusselt number of the 2-phase flow was enhanced relative to the 1-phase system by an amount that increased with increasing T_b. Varying the cavity density (69, 32, 3.2, 1.2 and 0.3 per mm^2) had only a small effect on the global Nu enhancement; it was found that Nu per

*Accepted as: [Daniela Narezo-Guzman, Yanbo Xie, Songyue Chen, David Fernandez-Rivas, Chao Sun, Detlef Lohse and Guenter Ahlers, Heat-flux enhancement by vapor-bubble nucleation in Rayleigh-Bénard turbulence, J. Fluid Mech.].

active site decreased as the cavity density increased. The heat-flux enhancement of an isolated nucleating site was found to be limited by the rate at which the cavity could generate bubbles. Local bulk temperatures of 1- and 2-phase flows were measured at two positions along the vertical center line. Bubbles increased the liquid temperature (compared to 1-phase flow) as they rose. The increase was correlated with the heat-flux enhancement. The temperature fluctuations, as well as local thermal gradients, were reduced (relative to 1-phase flow) by the vapor bubbles. Blocking the large-scale circulation around the nucleating area, as well as increasing the effective buoyancy of the 2-phase flow by thermally isolating the liquid column above the heated area, increased the heat-flux enhancement.

2.1 Introduction

Turbulent thermal convection is a phenomenon present in nature and in many technological applications. The idealized version is a fluid contained within adiabatic side walls and conducting horizontal top and bottom plates, cooled from above and heated from below. This system is known as Rayleigh-Bénard convection (RBC). RBC has been a model for the study of buoyancy-driven fluid turbulence and heat transfer in turbulent flows. In this system most of the temperature difference is sustained by thin thermal boundary layers (BLs), one each adjacent to the top and bottom plate, with an interior which is nearly isothermal in the time average. The thermal boundary layers play a key role in the heat transfer. Thermal plumes detach from them, initiating and contributing to the driving of a large-scale circulation (LSC) in the bulk. RBC has been extensively explored in many experimental, numerical, and theoretical studies (for reviews, see Refs. [56–60]).

In the great majority of papers on RBC, the sample was kept far away from any phase transitions so that only a single phase of the fluid was present. An exception is the experimental study of turbulent two-phase RBC using ethane at a constant pressure P near its vapor pressure curve $T_\phi(P)$ in Refs. [65]. Those authors applied a fixed temperature difference $\Delta T = T_b - T_t$ between the bottom (at T_b) and the top (at T_t) of the sample, with the mean temperature $T_m = (T_b + T_t)/2$ chosen so that $T_t < T_\phi$ while $T_b > T_\phi$. Under those conditions the bulk of the sample consisted of vapor when its temperature T_m was above T_ϕ, and liquid droplets ("rain drops") formed in the boundary layer below the top plate (where over a very thin layer T was less than T_ϕ) and fell toward the bottom, evapourating along their path and thus contributing to the heat transport. When $T_m < T_\phi$, the bulk of the sample filled with liquid, and vapor bubbles formed in the boundary layer adjacent to the bottom plate. The authors found a reproducible and history independent enhanced heat transport due to droplet condensation which increased linearly by as much as an order of magnitude with decreasing T_m. When $T_m < T_\phi$ and vapor bubbles formed near the bottom plate, the heat transport became time and history dependent. The authors concluded that the droplet formation within the liquid BL below the top plate occurred away from the solid surface and was not influenced by the surface roughness, leading to a nucleation process that was homogeneous. However, the vapor-bubble formation apparently involved heterogeneous nucleation processes which were hysteretic and irreproducible.

A similar study was carried out more recently in Ref. [72] using a nematic liquid crystal which undergoes a first-order phase transition from the nematic to the isotropic state; in this case the latent heat involved is much smaller than is typical at the liquid-gas transition but comparable to that of transitions in Earth's mantle.

Boiling is a very effective mode of heat transport and therefore it is used in various situations where a high heat-removal rate from a surface is desired. It is of fundamental interest to understand the physical mechanisms responsible for the heat-flux enhancement in a turbulent boiling flow. There already have been multiple studies of the heat-flux attained due to heterogeneous boiling in natural convection and under the influence of a forced flow (for reviews see for instance Refs. [2] and [23]). Boiling is a complex problem since it depends on liquid as well as on surface properties. For example, increasing roughness decreases the incipient boiling temperature, with a noticeable effect seen even for mean roughness as small as 10 nm, as reported in Ref. [14]. Those authors also found that wettability has an effect on the incipient boiling temperature: a larger contact angle requires a lower boiling superheat than is the case for a smaller contact angle. On the other hand, wettability also affects bubble growth and bubble departure from a surface due to buoyancy [12]. Because boiling depends on many parameters, a complete quantitative understanding has not yet been achieved.

Boiling RBC was addressed in numerical studies in Refs. [66–71]. In these studies a constant number of deliberately introduced bubbles (bubble nucleation and detachment was not simulated), with arbitrarily chosen diameters of several tens of μm, was seen to significantly change the structure of the convective flow. For a small Jakob number Ja (the ratio of sensible to latent energy, see Eq. (2.3) below) Refs. [66] and [67] reported that the bubbles take a significant amount of energy from the hot plate and release it close to or at the cold one, thus (at constant total applied heat current) decreasing the temperature difference between the plates responsible for driving the natural convection. For larger Ja, bubbles grow in hot flow regions, contributing to buoyancy and thereby leading to an overall higher heat transport. Also at larger Ja bubbles were found to augment velocity fluctuations of the liquid through mechanical forcing [67] and therefore increase the kinetic-energy dissipation-rate [68], which in turn enhances mixing of the thermal field. For all Ja values bubbles were found to increase the thermal-energy dissipation-rate [68] because bubbles create large local temperature gradients as their surface temperature is fixed at the saturation temperature. Ref. [70] found that bubbles subject the boundary layers to intense velocity and thermal fluctuations, adding to convective effects and breaking the up-down symmetry observed for the single-phase flow by considerably thickening the layer of hot fluid at the bottom. These authors studied the flow at various thermal forcing values (*i.e.* Rayleigh numbers Ra, see Eq. (2.1) below) as well as for different bubble numbers. They found that the heat-transport enhancement relative to the non-boiling RBC flow due to vapor bubbles was a decreasing function of Ra and that, given a fixed Ra, the enhancement increased with bubble number and with the degree of superheating of the bottom plate (*i.e.* with increasing T_b). They found an expression for the effective buoyancy which is an increasing function of the superheating. Strong intermittency of the temperature fluctuations originated from sharp temperature fronts. These fronts smoothened out in the presence of bubbles due to their effective heat capacity [71],

reducing the intermittency of the temperature and velocity fluctuations.

Imperfections or cavities on a surface, also called crevices, can trap gas and/or vapor and serve as nucleation sites [2; 8; 73]. Nucleating cavities reduce the superheat necessary to obtain a given heat-flux when compared to a smooth surface [11]. In such case, or if the liquid wets the surface well, heterogeneous nucleation can initiate at superheats similar to those for homogeneous nucleation [6] since all imperfections are filled with liquid. Gas and vapor entrapment in a cavity can occur when the liquid first gets in contact with the surface. Liquid vapor is more likely to be trapped if the surface is hot. Furthermore, gas dissolved in a saturated liquid might come out of solution and form gas bubbles in cavities as the temperature approaches the boiling temperature. Air dissolved in the fluid and entrapped in cavities affects the nucleation process, leading to greater heat-transfer enhancement and to a lower incipient boiling temperature [15; 16]. Vapor and gas trapped in a cavity, or so called nuclei, develop into a bubble only if several criteria are fulfilled; there are various models on the incipient wall superheat for boiling from preexisting nuclei, see Refs. [9; 10; 74]. The authors of Ref. [19] were some of the first to study boiling heat transfer using fabricated microcavities. Since then, cavity and surface fabrication methods have been refined, facilitating controlled nucleation experiments. An example of this is the recent work by Ref. [7], where the classical theory for bubble nucleation was validated for nano- to micro-size cavities.

Rough surfaces typically have random potential nucleation sites, and the number of active sites becomes larger as the heat transferred by the surface or the surface superheat $T - T_\phi$ (where T is the surface temperature) are increased. A larger number of active sites in turn, increase the heat transferred by the surface. Ref. [2] obtained a relation between the active site number and the surface superheat for a typical rough surface. The contribution to the total heat-flux of an individual site decreases with increasing heat-flux due to a drop in the spacing between active sites, see Refs. [18; 21]. Ref. [44] reported that site spacing had an essential influence on bubble coalescence characteristics, bubble departure size, departure frequency and heat-flux distribution on the heating surface. Interactions between two neighboring active nucleation sites were studied in Ref. [43], finding that the bubble release frequency depended on cavity spacing and identifying four regions in which interactions between nucleation sites were of different nature. They concluded that the influence of each interaction mechanism may be different for different liquid and surface conditions.

Many proposed mechanisms by which heat is transferred by an isolated bubble growing in a quiescent liquid at a surface and eventually departing are reviewed in Ref. [23]. He concluded that, for liquids under conditions spanning a Ja range of several orders of magnitude, the processes at the wall such as micro-layer evaporation and contact-line heat-transfer contributed less than transient conduction and micro-convection. Transient conduction is related to the wall rewetting process as a bubble grows and departs; micro-convection occurs when a bubble departs and perturbs the liquid adjacent to it, disrupting the natural convection boundary layer. The vapor-bubble energy-content (latent heat) mostly came from the superheated liquid attained through the bubble cap and not from processes at the wall. Based on experiments in water, Ref. [75] concluded that micro-layer evaporation dominantly contributed to the wall heat-transfer during the bubble-growth period and that the contribution

of the wall heat-transfer to the bubble growth declined with increasing wall superheat. The recent work in Ref. [76] on vapor-bubble growth in forced convection using water showed that most of the latent heat-content of the bubbles came through the surrounding superheated liquid and was relatively independent of the bulk liquid velocity. An increasing bulk liquid temperature led to a decrease of the ratio between heat attained from the wall and from the surrounding liquid.

In the present chapter we experimentally studied well controlled heat-flux enhancement due to heterogeneous boiling in a mostly liquid-filled turbulent RBC sample. To overcome the lack of control over nucleation sites at the superheated surface, we used silicon wafers with many identically etched micro-cavities arranged in a lattice that acted as vapor-bubble nucleation-sites. After they were deactivated by assuring that they were filled with liquid, the heat-flux of the superheated flow under the same thermal forcing conditions as for the boiling experiments was measured. We compared the heat-flux of boiling and non-boiling superheated flow and determined the heat-flux enhancement due to vapor-bubble formation. This chapter thus provides insight into heat-flux enhancement as a global flow quantity under well controlled boiling conditions, and how this enhancement depends on nucleation-site density. Supplementary local temperature measurements revealed the effect of bubbles on the temperature in the bulk of the fluid well above the nucleation sites and showed how this temperature strongly correlates with the heat-flux enhancement.

In the next section of this chapter we define various quantities needed in the further discussions. Then, in section 3.3 we describe the apparatus and measurement procedures used. In section 3.4 the experimental results are discussed and in section 3.5 a summary and our conclusions are provided.

2.2 Control and response parameters of the system

For a given sample geometry, the state of single-phase RBC depends on two dimensionless variables. The first is the Rayleigh number Ra, a dimensionless form of the temperature difference $\Delta T = T_b - T_t$ between the bottom (T_b) and the top (T_t) plate. It is given by

$$Ra = \frac{g\alpha \Delta T L^3}{\kappa \nu}. \tag{2.1}$$

Here, g, α, κ and ν denote the gravitational acceleration, the isobaric thermal expansion coefficient, the thermal diffusivity, and the kinematic viscosity, respectively. The second is the Prandtl number

$$Pr = \nu/\kappa \ . \tag{2.2}$$

Unless stated otherwise, all fluid properties are evaluated at the mean temperature $T_m = (T_b + T_t)/2$.

For samples in the shape of right-circular cylinders like those used here, a further parameter defining the geometry is needed and is the aspect ratio $\Gamma \equiv D/L$ where D is the sample diameter.

In a single-component system involving a liquid-vapor phase change the relevant

dimensionless parameter is the Jakob number

$$Ja = \frac{\rho C_p (T_b - T_\phi)}{\rho_v H} \tag{2.3}$$

where ρ and ρ_v are the densities of liquid and vapor respectively, C_p is the heat capacity per unit mass of the liquid, H is the latent heat of evaporation per unit mass, and T_ϕ is the temperature on the vapor-pressure curve at the prevailing pressure (when the dissolved-air concentration in the liquid equals zero). The limit $Ja = 0$ implies a bubble which is not able to grow or shrink because either the latent heat is infinite or the vapor and liquid are in equilibrium with each other. In our experiments, dissolved air in the liquid reduced the temperature T_{on} at the onset of nucleation below T_ϕ, and in Eq. (2.3) T_ϕ should be replaced by T_{on}, see section 2.3.6. We refer to $T_b - T_{on}$ as the bottom-plate superheat.

The response of the system to the thermal driving is reflected in the vertical heat transport from the bottom to the top plate, expressed in dimensionless form by the Nusselt-number

$$Nu = \frac{\lambda_{eff}}{\lambda} \tag{2.4}$$

where the effective conductivity λ_{eff} is given by

$$\lambda_{eff} = QL/(A\Delta T) \tag{2.5}$$

with Q the heat input per unit time to the system and λ the thermal conductivity of the quiescent fluid. In classical RBC, where the entire bottom-plate area is heated, A is the cross sectional area of the cell. In our case, however, only the central circular area A_h of 2.54 cm diameter is heated. We choose to define λ_{eff} by using only the heated area A_h instead of the total area A in Eq. (2.5).

The response of the system is also reflected in temperature time-series $T(z,x,t)$ taken at positions (z,x) in the sample interior. Here z is the vertical distance which we choose to measure from the position of the bottom plate and x is the horizontal distance from the vertical sample center-line, see figure 2.1b. We measured $T(z,x,t)$ and computed time averaged temperatures $T(z,x)$, as well as the standard deviation

$$\sigma(z,x) = \langle [T(z,x,t) - T(z,x)]^2 \rangle^{1/2} \tag{2.6}$$

and the skewness

$$S(z,x) = \langle [T(z,x,t) - T(z,x)]^3 \rangle / \sigma^3 \tag{2.7}$$

of their probability distributions $p(T(z,x,t))$, at the two locations $(z/L = 0.28,\ x/D = 0)$ and $(z/L = 0.50,\ x/D = 0)$. Here and elsewhere $\langle ... \rangle$ indicates the time average.

2.3 Apparatus and Procedures

2.3.1 The apparatus

The experiments were conducted in two different convection apparatuses that had similar features. Both were used before; the so-called “small convection apparatus”

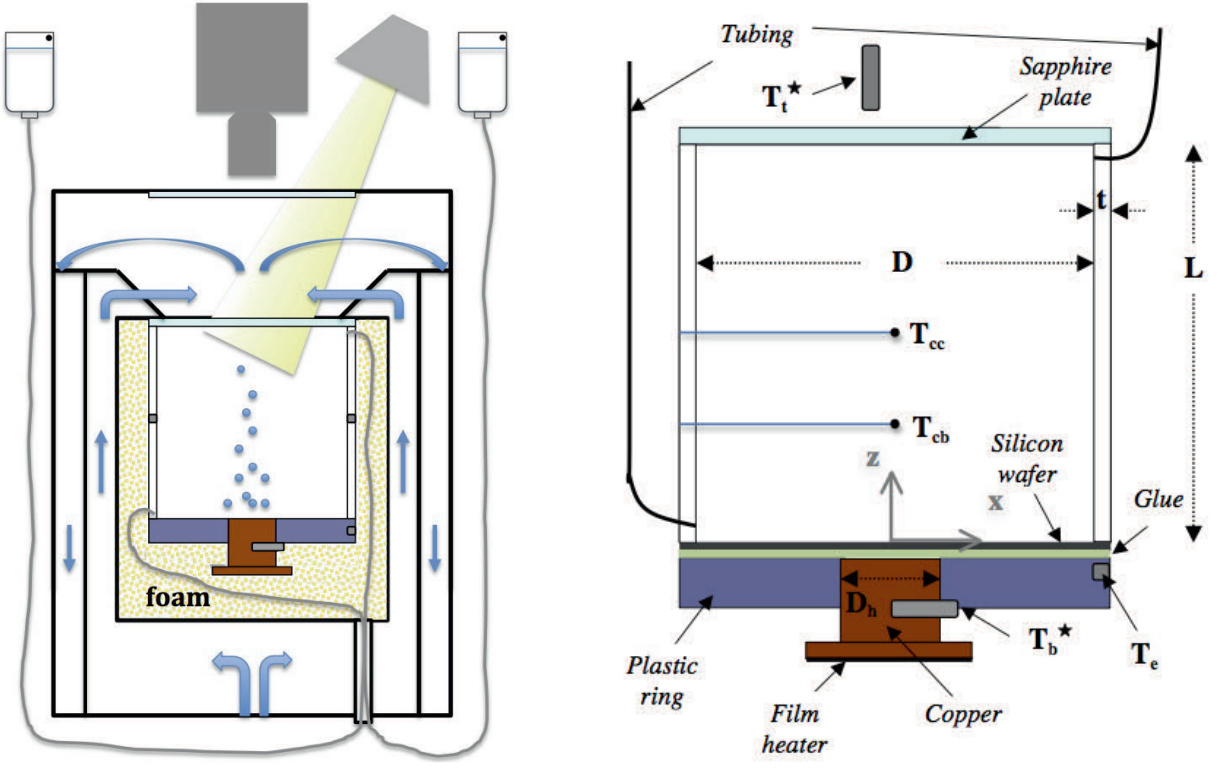

(a) (b)

Figure 2.1: (a): A sketch of the apparatus. The apparatus housed a cell connected to two reservoirs that contained liquid and were open to the atmosphere. The cell was filled with liquid except for the vapor bubbles. The apparatus top window and the transparent top plate of the cell allowed for flow imaging from the top. The arrows indicate the direction of the circulating cooling bath. (b): A sketch of the cell cross section. The locations of thermistors are indicated by the corresponding measured temperatures T_{cc} and T_{cb}.

was described in Ref. [77] and details of the other one were given in Refs. [65; 78–80]. Here a brief outline of the main features is presented and sketched in figure 2.1a.

A cylindrical convection cell was located inside a dry can. All free space surrounding the cell was filled with foam in order to prevent convective heat transport by the air. The cell was subjected to a vertical temperature difference by a water-cooled top plate and a bottom plate heated by a film heater glued to its underside. The temperatures of both plates were computer-controlled; top and bottom plate had milli-Kelvin and centi-Kelvin stability, respectively [65]. The cylindrical dry can was inside a larger cylindrical container. The bath water flowed between them: closest to the dry can the water moved upwards, reached the apparatus top where it cooled the top plate of the cell, and then flowed downwards in a cylindrical space separated from the up-flow by a wall made of low-conductivity material.

Reservoir bottles (outside the apparatus) were connected to the top and bottom of the convection cell via thin teflon tubing. The tubing and electrical leads passed through a wider tube, which went from the dry can through the bath to the laboratory. A window in the top of the apparatus and a transparent (sapphire) top plate of the cell enabled visualization of the cell interior. Two cameras (QImaging Retiga 1300 and a high-speed camera Photron Fastcam Mini UX100), two lenses (Micro Nikor 105mm, f/2.8 and AF Nikkor 50mm, f/1.4) and three desktop lamps (using 13 W, 800 lumens bulbs) that remained on throughout all measurements were used to capture images of the flow. Since we investigated *differences* of heat flux and temperature, the very small effect of the radiation from the lamps did not influence the results significantly.

2.3.2 The cell and the bottom plate

In both apparatuses a cell with the same features was used. Each cell (shown in figure 2.1b) consisted of a polycarbonate sidewall with thickness $t = 0.63$ cm, height $L = 8.8$ cm and with aspect ratio $\Gamma \equiv D/L = 1.00$ (D is the cell diameter). The fluid in the cell was confined between a bottom plate and a 0.635 cm thick, 10 cm diameter sapphire plate on the top. The bottom plate consisted of a 10 cm diameter silicon wafer on top of a copper cylinder with diameter $D_h = 2.54$ cm surrounded by a 10 cm outer diameter and 1.26 cm thick plastic ring, and a metal-film heater attached to the bottom of the copper cylinder. All silicon wafers were $L_s = 0.53$ mm thick, with nucleation cavities etched into their up-facing sides over a central circular area of 2.54 cm diameter. The copper cylinder had a T-shaped cross section that widened near its bottom from a 2.54 cm to a 5.08 cm diameter. The area in contact with and heating the silicon wafer was $A_h = 5.07$ cm^2. Either a 56 Ω or a 38 Ω round Kapton metal-film heater (with nominal diameter of 5.1 cm or 3.8 cm, respectively) was glued to the bottom of the copper piece. The wafer was glued to both the top of the copper piece and the plastic ring. In some cases the glue used was degassed epoxy (Emerson and Cuming, STYCAST 1266). In others it was acrylic pressure sensitive adhesive or PSA (Minco Nr. 19), with nominal thickness of 0.051 mm. The plastic ring provided support to hold the cell tightly while it prevented the silicon wafer from breaking. The ring was made of polycarbonate (which has a low thermal conductivity) in order to reduce the heat conducted horizontally towards the cell edge.

In preliminary experiments heating took place over the entire bottom-plate area

(diameter of 10 cm); this led to undesired nucleation sites along the spacing between the side wall and the bottom plate.

To account for the heat flux across the cell walls and for the heat lost into the apparatus we measured the heat flux at a temperature difference $T_b^\star - T_t^\star = 20$ K across the empty cell for various T_m at a pressure smaller than 0.06 bar. This heat flux was due to the heat conducted across the cell wall, to pure conductive heat-flux through air in the cell, and to any heat lost through the can (see figure 2.1a). After subtracting an estimate of the heat flux due to stagnant air, we obtained the correction. With increasing T_m the correction ranged from about 25% to about 19% of the 1-phase measured heat flux.

2.3.3 Temperature measurements

A thermistor (Honeywell type 121-503JAJ-Q01) was inserted inside the plastic ring and underneath the cell edge to keep track of the edge temperature T_e, as shown in figure 2.1b. We measured the vertical temperature difference across the edge of the plastic ring by inserting a second thermistor (not shown in figure 2.1b) at the lower edge of the ring (below the location of T_e). This temperature difference was found to be less than 1% of ΔT. Another thermistor of the same type was inserted into the copper piece approximately 1.4 cm below the upper surface and measured $T_b^\star$ (see figure 2.1b), which was controlled so as to be constant during a run.

The net thermal resistance R_w of the silicon wafers depended on the number of cavities N etched over an area A_h. We estimated it by assuming that it was the result $R_w = R_s + R_s'$ of two resistors in series. Since the conductivity of the fluid in the cavities was negligible compared to that of Silicon, we took the first part R_s to be that of the wafer near the fluid and of thickness $L_c = 100$ μm and a cross sectional area $A_h - NA_c$. Here L_c is the cavity depth and A_c the cavity cross sectional area. The second resistor R_s', representing the remainder of the wafer, had a thickness $L_s - L_c$ and a cross sectional area A_h. For the wafer etched with $N = 33680$ cavities R_w was about 5% larger than R_w for the wafer with $N = 570$ cavities.

The temperature T_b at the liquid-solid interface of the wafer was obtained by considering the temperature drop across each of the bottom-plate layers, namely the copper, glue, and silicon wafer. When epoxy was used as glue, its thickness was determined indirectly by measuring the thermal resistance across all layers (see appendix 2.A). Because of the relatively small heated area and low thermal conductivity of epoxy or PSA compared to those of copper and silicon, even a very thin layer of these materials had a significant effect on the temperature difference between $T_b^\star$ and T_b. The temperature drop $T_b^\star - T_b$ depended on the heat-flux and varied between 3 and 5 K for an applied temperature difference $T_b^* - T_t^*$ of 20 K.

The top temperature $T_t^\star$ was determined with a thermistor of the same type immersed into the cooling bath through the top side of the apparatus. It was held constant during each run. The temperature drop (of a fraction of a degree) across the top plate was estimated from the thermal conductivity of sapphire and the applied heat current in order to determine the liquid top temperature T_t.

All thermistors were calibrated against a Hart Scientific Model 5626 platinum resistance thermometer with milli-Kelvin precision.

Figure 2.2: Photograph of a Honeywell 111-104HAK-H01 thermistor assembled with its 0.8 mm diameter ceramic rod, ready for insertion into the interior of the cell.

One of the cells had two extra 0.36 mm diameter thermistors (Honeywell type 111-104HAK-H01) inserted into the interior of the cell. Each thermistor had its leads passed through 0.13 mm diameter holes embedded along a ceramic rod 0.8 mm in diameter (Omega ceramic thermocouple insulators type TRA-005132), see figure 2.2. The rods went through 0.9 mm holes drilled through the side wall so that both thermistors were on the same vertical plane, one at mid-height ($z/L = 0.50$) and the other one 2.54 cm above the wafer surface ($z/L = 0.28$). The holes were sealed to the external side of the cell using epoxy. Both thermistors were inserted half way through the cell diameter (at $x/D = 0$); the one at $z/L = 0.28$ acquired the temperature T_{cb} and the one at $z/L = 0.50$ measured T_{cc}. These thermistors were calibrated against the water-bath thermistors. More details about the use and performance of these thermistors are given by Refs. [81; 82] and in appendix 2.B. We estimate that the uncertainty of the vertical position of each thermistor is approximately $\pm 0.01L$.

2.3.4 The etched wafers

N	l [mm]	N/A_h [1/mm^2]
142	2.00	0.28
570	1.00	1.12
1570	0.60	3.10
15460	0.19	30.50
33680	0.10	66.43

Table 2.1: The total number of cavities N, center-to-center spacing l, and number of cavities per mm^2 N/A_h for the wafers used in this chapter.

We performed experiments using five different silicon wafers [Okmetic, Vantaa, Finland, crystalline orientation (100)] with micron-sized cavities on a triangular lattice (see figure 2.3a) made by a lithography/etching process on one polished wafer side. The process was carried out under clean-room conditions using a plasma dry-etching machine (Adixen AMS 100 SE, Alcatel). The wafers were plasma cleaned to remove any fluorocarbon traces remaining from the dry-plasma etching process. In each wafer the cavity lattice covered a 2.5 cm diameter circular area centered on the wafer; outside this area the wafers had a smooth surface (3.46-4.22 Å). The roughness of the cavity walls was less than 500 nm. The etched area accurately coincided with the heated area A_h. The cooling area extended over the entire top plate; thus it was 15.5 times larger than A_h. Each wafer had a different center-to-center cavity spacing l and thus a different cavity density, as listed in table 2.1. The cavities had a depth

of $L_c = 100 \pm 5\mu$m and a diameter of $2r = 30 \pm 2\mu$m. Figure 2.3b shows an image of a diagonal cut through a sample wafer with $l = 0.1$ mm. In figure 2.3c the dimensions and shape of a single cavity can be appreciated. Figure 2.4 shows a snapshot from the top of controlled boiling with $l = 0.60$ mm; note that bubble nucleation only takes place at the etched cavities over A_h.

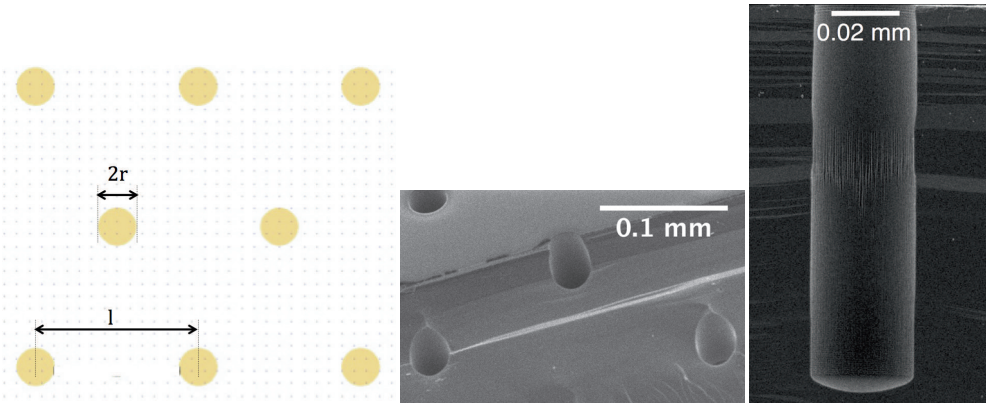

(a) (b) (c)

Figure 2.3: Schematic diagram and images of a wafer with an equilateral triangular lattice of etched cavities. In (a) the center-to-center distance between neighboring cavities is l and the cavity diameter is $2r = 30\mu$m. Shown in (b) is a scanning electron microscope image of a diagonal cut through a wafer with $l = 0.1$ mm, and (c) shows a scanning electron microscope image of a cut through a single cavity with a depth $L_c = 0.10$ mm.

2.3.5 The fluid

The working fluid was the fluorocarbon 1-methoxyheptafluo-ropropane (Novec7000$^{\text{TM}}$ manufactured by 3M$^{\text{TM}}$). We chose this liquid because it has a relatively low boiling temperature of 34°C at atmospheric pressure. At room temperature and a pressure of one bar the solubility of air is about 31% by volume. All relevant properties are given as a function of temperature by the manufacturer and they were evaluated at T_m unless stated otherwise. In the experiments presented here T_m ranged from 35°C to 18°C. The Prandtl number (see Eq. (2.2)) ranged from 7.5 to 8.2 with decreasing T_m. The resulting Rayleigh number (see Eq. (2.1)) ranged from 1.4×10^{10} to 2.0×10^{10} over the range of T_m.

2.3.6 Experimental procedure

Cell filling procedure

The cavities were active nucleation sites when they were filled with gas and inactive when filled with liquid. A carefully defined cell-filling procedure had to be followed

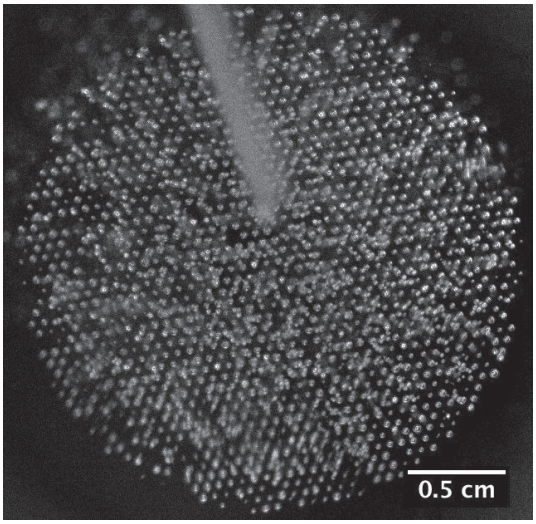

Figure 2.4: Snapshot of active nucleating cavities covering a central circular area A_h of 2.54 cm diameter of the bottom silicon plate. The cavity separation was 0.60 mm. Bright dots correspond to bubbles still attached to the cavity mouths. Detached bubbles already risen to a greater height are out of focus and appear as diffuse grey spots. The flat area outside of the central 2.54 cm diameter area contains no cavities and thus shows no bubble nucleation. A thermistor inserted well above the bottom plate, extending from the top of the image toward the center, is out of focus.

in order to produce gas-filled cavities while the entire remainder of the cell was filled with liquid.

Initially the cell contained no liquid, and the reservoir connected to the bottom part of the cell (see figure 2.1a) contained all the liquid. Both reservoirs were connected to the cell through tubing attached at their lids. The reservoirs also had short tubes at their bottom that could provide a connection to the atmosphere or be closed when for example the reservoir filled with liquid was to stand on a solid surface. In order to fill the cell, the reservoir connected to the bottom part of it was held upside-down above the bottom-plate level while the other (empty) reservoir was open to the atmosphere.

The filling speed was determined by the vertical position of the reservoir connected to the cell bottom. Filling the cell too rapidly by positioning the reservoir too high above the bottom plate led to deactivation of the cavities positioned closest to the liquid entrance. Not positioning the reservoir high enough prevented the hydrostatic pressure to overcome the excess pressure due to liquid boiling in the cell and liquid did not flow into it. During filling we used $T_b^\star = 45°\mathrm{C}$ and $T_t^\star = 15°\mathrm{C}$. Since $T_b^\star$ was larger than the boiling point of $\simeq 34°\mathrm{C}$, liquid first touching the hot wafer evaporated and the cavities trapped vapor, thus assuring activation of all cavities as more liquid continued to fill the cell. At the same time, since $T_t^\star$ was colder than 34°C, most of the vapor contained in the cell condensed on the top plate, thus reducing the loss

of material by escaping vapor. The increasing amount of liquid in the cell boiled throughout the filling time of approximately 3 hours, thus eliminating some of the air dissolved in the liquid. The air accumulating in the vapor phase could escape through the tubing connected to the top part of the cell, which remained open to the atmosphere. When the cell was nearly full, the liquid levels inside the reservoir and the cell were set at equal heights and boiling with a free surface continued for another 60 minutes. This procedure was intended to lead to a reproducible and reduced air concentration in the liquid phase. Afterwards the reservoir containing the remaining liquid was set higher above the bottom plate. This was done gradually in steps to assure that all cavities remained active; a rapid pressure change in the cell could lead to cavity deactivation.

The final liquid column of 1.16 m above the wafer exerted a constant hydrostatic pressure on the bottom plate of 16.0 ± 0.3 kPa in addition to the prevailing atmospheric pressure. The atmospheric pressure measured over a typical three-day period was 101.6 ± 0.2 kPa. The total pressure on the surface of the wafer thus was $P = 117.6 \pm 0.4$ kPa and remained constant throughout all measurements or runs.

For the wafer with $l = 2.0$ mm it was more difficult to produce active cavities. In this case we used the higher temperatures $T_b^\star = 49^\circ$ C and $T_t^\star = 16^\circ$ C while filling the cell. Nonetheless, some nucleation sites became inactive as the cell slowly filled. During the filling process the cell was tilted to prevent the drops forming under the top plate from landing on the boiling central region. Of the 142 etched cavities the number of active sites, once the cell was full, was 45 or less.

Measurement protocol

We refer to a run with no active sites as 1-phase flow and one with active sites as 2-phase flow. For all 1- and 2-phase runs presented here we used $T_b^\star - T_t^\star = 20$ K. A two-phase run typically started at $T_b^\star = 45°$C and $T_t^\star = 25°$C (in a few cases it started at $T_b^\star = 46°$C and $T_t^\star = 26°$C). Once a statistically stationary flow was reached, i.e. when the mean values (over intermediate time intervals) of heat flux and passive temperature signals did not vary in time, measurements continued for a sufficiently long time to determine the mean and standard deviation of the measured quantities over the long time iterval. Then the next data point was set by decreasing both $T_b^\star$ and $T_t^\star$ by typically 1 K (or sometimes by a larger step), waiting for statistically stationary conditions, and again measuring as long as appropriate. The process continued until all nucleation sites became inactive due to the low temperature and filled with liquid. Then $T_b^\star$ and $T_t^\star$ were increased again in steps to carry out the superheated 1-phase runs. Once all sites were inactive, $T_b^\star$ could be increased to temperatures as high as 65°C without producing bubble nucleation. In order to generate a new set of 2-phase measurements, the cell had to be emptied and then re-filled in order to re-activate the cavities.

For 2-phase flow it could take up to two days for the system to reach a statistically stationary state. For most 1-phase runs stationarity was reached within less than a day. Pictures of the active cavities were taken once the stationary state was reached. In all 1-phase runs the cell remained full of liquid. For 2-phase flow the cell also was full except for the bubbles forming at the bottom plate and condensing at the top

cold plate or along their rising motion. It was necessary to keep $T_b^\star$ equal to or below 46°C so as to avoid vapor from accumulating near the top of the cell, thus producing a free liquid surface.

Estimate of dissolved-air concentration

The solubility of air in fluorocarbons is quite high, and dissolved air is known to play an important role in the bubble-nucleation process [15; 16; 83]. If the liquid had been fully degassed, the temperature T_ϕ on the vapor-pressure curve would have been 38.5°C at the hydrostatic pressure P exerted on the bottom plate. The fact that bubbles nucleated at temperatures below 38.5°C indicates that air was dissolved in the liquid and reduced the saturation temperature.

Assuming the validity of Henry's Law and a Henry's Law constant independent of temperature over our temperature range, we made an estimate of the dissolved-air concentration. For seven 2-phase data sets we extrapolated the excess heat current due to boiling as a function of temperature to the temperature T_b where it vanished (*i.e.* where all nucleating sites became inactive, see section 2.4.2). Averaging over these sets gave 30.3 ± 1.1 °C, which we define here as T_{on}. Setting T_{on} as the vapor-liquid equilibrium temperature $T_\phi(P_v)$ gave a vapor partial pressure $P_v = 86.2$ kPa. The total pressure of $P = 117.6$ kPa and assuming that $P_a = P - P_v$ yielded an air partial pressure $P_a = 31.4$ kPa. Using the known solubility of 31% by volume of air at 25° C and atmospheric pressure (approximately 101 kPa), we estimated Henry's Law constant and used it to find that this value of P_a corresponds to an air concentration in the liquid of 23% by volume (for details of the calculation see appendix 2.C). Given the high solubility of air at ambient conditions, this estimate is reasonable, and the reproducibility of T_{on} indicates that the liquid used in our measurements had a reproducible amount of air dissolved in it.

2.4 Results

2.4.1 Visualization of the nucleating area

Here we present qualitative features of the 2-phase flow obtained by imaging the vapor-bubble-nucleating silicon wafers from above.

For wafers with $l = 0.10, 0.19$ and 0.60 mm an increasing number of nucleating sites near the rim of the etched area turned inactive as T_b decreased. This is illustrated in figure 2.5. There nine images show the same area (slightly larger than the etched area A_h of 2.5 cm diameter) of the wafer with cavity separation $l = 0.19$ mm (15460 cavities). Each image is the result of averaging over two sets of 32 snapshots taken within 8 seconds; the sets were captured at least 2 hours apart and once the system had reached a stable state. These averaged images show inactive cavities as dark dots located where, at a higher temperature, there were active cavities revealed by bright dots. Typically, at the beginning of a 2-phase run $T_b \simeq 40$°C and all cavities were active. Figure 2.5a is for $T_b = 39.60$°C ($T_b - T_{on} = 9.3$ K) where the large majority of sites were still active. As T_b was decreased, an increasing number of sites deactivated. Merging of several small bubbles resulted in larger bubbles that remained on the

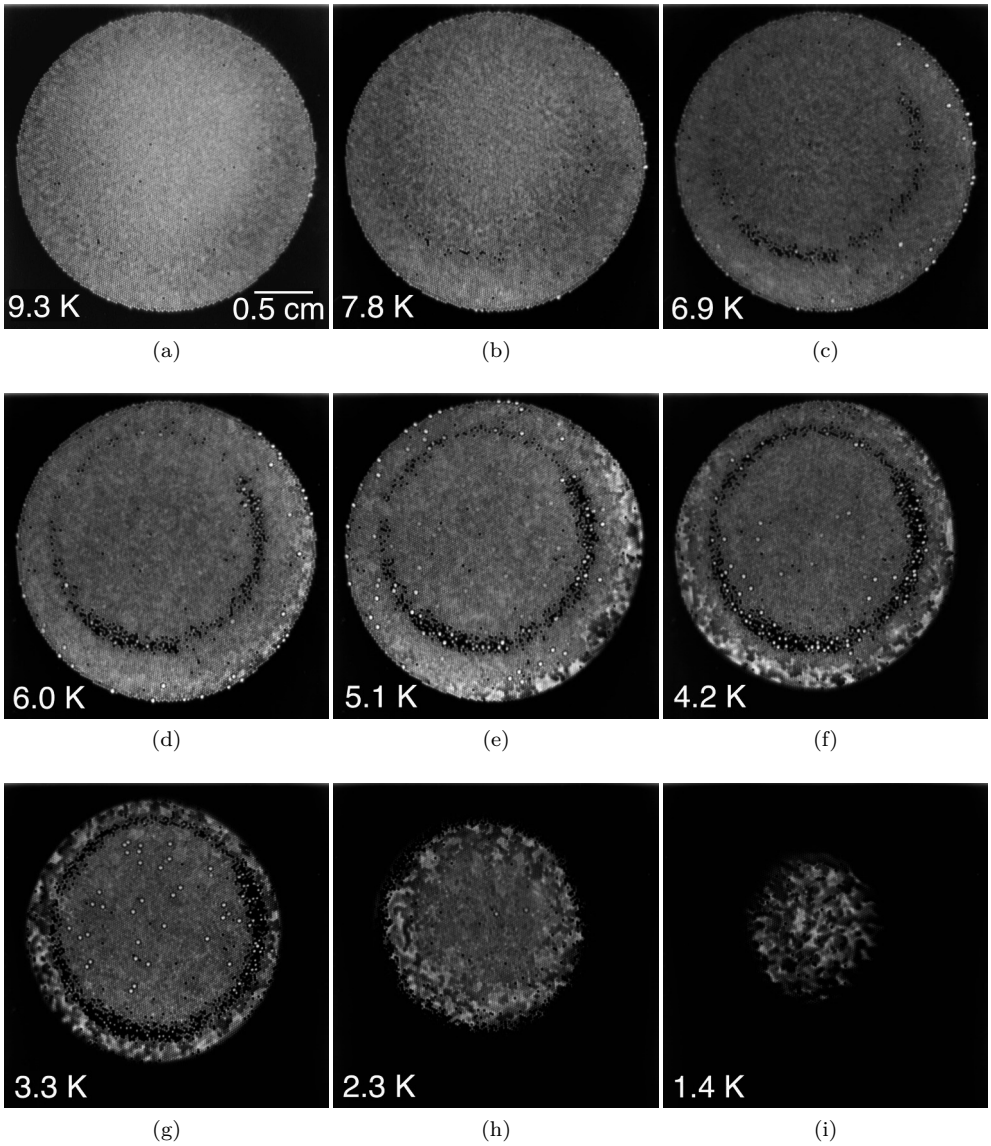

Figure 2.5: Averaged-intensity images of the wafer with cavity spacing $l = 0.19$ mm of active nucleating sites at the bottom-plate superheats $T_b - T_{on}$ given in each figure. All images cover the same area. In (a) the bright circle corresponds to the heated/etched area A_h with 2.5 cm diameter. Nearly all 15460 sites were active. Outside A_h no bubble nucleation took place and the wafer surface appears black. In (b) most sites were still active. A few larger bubbles (very bright dots) can be seen near the periphery of A_h. In (c) an inner dark circle of inactive sites started forming; a few sites at the outer rim turned inactive, similar to (d). In (e) the inner inactive circle expanded. In (f), (g), (h) and (i) more and more sites became inactive.

surface for much longer times than the departing smaller bubbles. These larger, long-lasting bubbles were identified with larger very bright spots on the images. For this wafer in particular a circle of inactive sites inside the etched area developed. However, this was not a common feature of other wafers, for which the diameter of the area covered by mostly active cavities typically simply shrank, see below and section 2.4.6. Silicon wafers processed with a plasma dry-etching processes can show structures with unexpected deviations due to non-uniform plasma density, so that individual wafers made with the same recipe can differ from each other. Similar non-uniformities have been reported in the literature [84; 85].

Bubbles that formed for $l = 0.10$ and 0.19 mm typically merged with several of their neighbours to form larger bubbles which either immediately after merging separated from the surface or remained attached to the surface for some time (see the high-speed movie number 1 in the supplemental material (or upon request) taken at 500 frames per second (fps) and displayed 20 times slower, showing the actively nucleating $l =$ 0.19 mm wafer for a superheat of 5 K). For wafers with larger l merging of more than two to three neighbouring nucleating bubbles was not observed and merging in general was less common than for $l = 0.10$ and 0.19 mm. We found that bubbles growing on a wafer with larger l, when they detached, often perturbed the surrounding liquid which then perturbed neighboring bubbles. These perturbed bubbles often were observed to oscillate laterally without detaching. The majority of detached bubbles moved horizontally a few centimeters under the influence of the LSC before becoming out of focus due to their vertical motion. Detached bubbles frequently collided and merged. The resulting larger bubble continued moving laterally with the LSC, as illustrated by the high-speed (recorded at 500 fps, slowed down 20 times for display) movie number 2 in the supplemental material (or upon request), which shows nucleation on the $l = 0.60$ mm wafer for a superheat of 9.6 K.

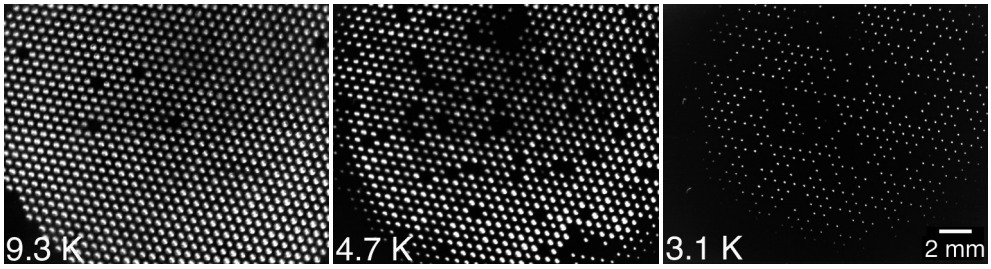

(a) (b) (c)

Figure 2.6: Average-intensity images of nucleating bubbles on a wafer with cavity spacing $l = 0.60$ mm at the $T_b - T_{on}$ values given in each figure. In (a) all sites except for 6 (6 dark dots on the lattice) were active. The edge of the etched area can be seen at the left bottom corner. In (b) and (c) an increasing number of sites became inactive.

Figure 2.6 shows three images that are each the result of averaging 500 snapshots of bubble nucleation on a wafer with $l = 0.60$ mm for different $T_b - T_{on}$ values. All

three images cover the same area of the wafer (see the scale bar on figure 2.6c). The edge of the etched area A_h can be seen at the left bottom corner of figure 2.6a. As in figure 2.5, an increasing number of sites, starting at the rim of the etched area, turned inactive as superheat was reduced. Randomly located nucleation sites inside A_h also deactivated.

The size of a bubble seen in the averaged images for $l = 0.60$ mm is close to the maximum size which is reached at departure from the nucleation site. The same is the case for bubbles formed on an $l = 1.0$ mm wafer. The size of nucleated bubbles close to the outer rim became noticeably smaller with the reduction of $T_b - T_{on}$ between figure 2.6a and figure 2.6b. Figure 2.6c shows that with a further decrease of $T_b - T_{on}$ many sites stopped nucleating and the remaining ones nucleated smaller bubbles. As superheat decreased, the bubble growth rate and detachment frequency decreased as well and a smaller frame rate was enough to capture the bubble evolution. For example, in figure 2.6a 500 fps captured the typical growth of a vapor bubble, whereas for figures 2.6b and 2.6c 50 fps were sufficient. The mean bubble diameter before departure in figure 2.6a was about 0.5 mm and in figure 2.6c about 0.2 mm.

We assume that deactivation of more and more sites with decreasing $T_b - T_{on}$ near the perimeter of the area covered by cavities was a consequence of the localized heating over A_h. Because of lateral heat flow through the polycarbonate ring and the wafer (see figure 2.1b) toward the side wall there was a horizontal temperature gradient in the wafer that influenced the bubble nucleation. This is suggested by the normalized measured temperature difference $(T_b - T_e)/\Delta T \simeq 0.6$; but it should be noted that most of this lateral temperature change was across the part of the plate outside the central area A_h across the polycarbonate ring and the wafer above it while the temperature gradient in the active area A_h above the high-conductivity copper plug remained small.

In general, the number of sites turning inactive when T_b was decreased occurred both at the rim of the etched area and inside it at randomly located nucleation sites. We also observed that, at the same superheat, cavities in wafers with larger l were more likely to stop nucleating. For example, for a data set obtained with $l = 1.0$ mm, 60% of the active sites at $T_b = 40.13°$C deactivated when $T_b = 36.63°$C. This may be compared with a data set measured with an $l = 0.60$ mm wafer, which showed deactivation of only 23% when T_b was reduced from 39.98° to 36.13°. In the case of $l = 0.19$ mm and a very similar T_b difference (compare figures 2.5a and 2.5d) far less than 23% of the active sites became inactive (see figures 2.5a). These observations indicate that nucleating sites closer to each other prevent neighboring sites from early deactivation; results obtained for $l = 0.1$ mm confirmed this as well. The extreme case was $l = 2.0$ mm which, as described in section 2.3.6, could not maintain all sites active even for a superheat larger than the highest one used for all other cavity separations. These observations suggest that interacting nucleating sites, which grow smaller bubbles than well separated sites, prevent cavities from being filled with liquid.

2.4.2 Heat-flux enhancement

Some considerations regarding the temperature environment of a growing bubble

While it is not possible to quantitatively determine the thermal environment in which bubble nucleation and growth takes place in turbulent RBC, it is possible and instructive to arrive at the semi-quantitative picture presented in this subsection.

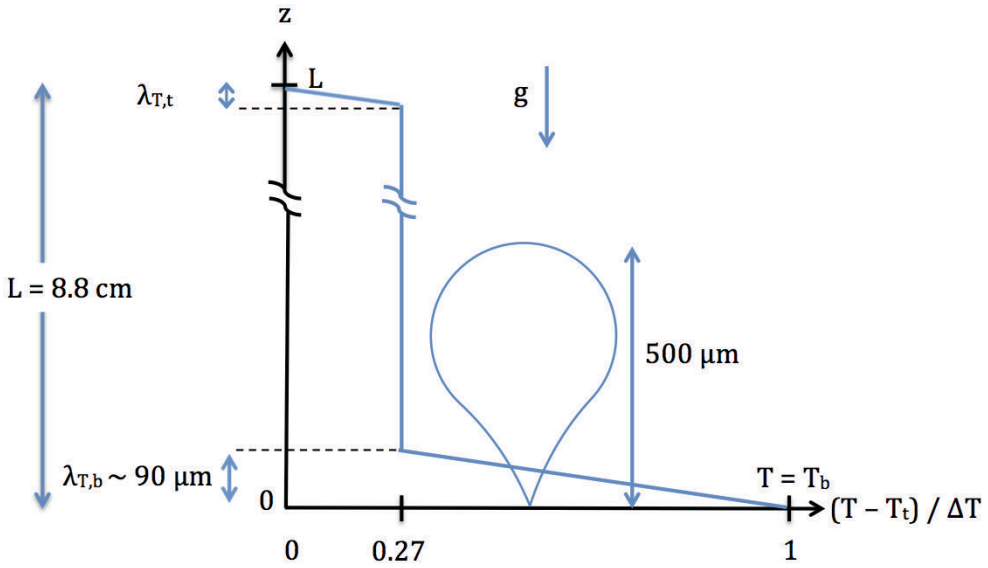

Figure 2.7: Schematic diagram of the bottom ($\lambda_{T,b}$) and top ($\lambda_{T,t}$) 1-phase boundary-layer (BL) thicknesses, given that the bulk normalized temperature was $(T_{cc} - T_t)/\Delta T \simeq 0.27$ or equivalently $(T_b - T_{cc})/\Delta T \simeq 0.73$. The bulk flow extends across most of the cell height L which is not shown to scale in the diagram. A fully grown bubble of typical size (hundreds of μm) attached to the bottom plate ($z = 0$) is displayed for comparison with the thermal BL thickness.

When $T_b > T_{on}$ bubbles are surrounded by liquid with a temperature larger than T_{on} only within part of the thermal boundary layer (BL) of thickness λ_T above the bottom plate because the bulk temperature above the BL, which is close to $T_{cb} \simeq T_{cc}$, was always below T_{on}. For 1-phase flow of classical RBC (see e.g. Ref. [57]), where the temperature drop across each BL is equal to $(1/2)\Delta T$, the BL thickness $\lambda_{T,0}$ is well represented by $\lambda_{T,0} = (1/2)L/Nu$ which, for our parameter values, is equal to about 60 μm. However, in our case the temperature drop across the bottom BL in 1-phase flow is $T_b - T_{cc} \simeq 0.73\Delta T$, and similar arguments yield a bottom BL thickness $\lambda_{T_b} \simeq 90$ μm and a thinner top BL with thickness $\lambda_{T,t}$ (see figure 2.7 for a schematic representation). It is likely that, given the composition of our bottom plates, some heat flows horizontally across the silicon wafer and outside A_h (see section 2.3.3 for the relatively high thermal conductivity of silicon relative to that of the quiescent liquid) and that it enters the flow through a wider effective area than A_h. In that

case, we would expect Nu to be smaller, as the effective area would be larger, and $\lambda_{T,b}$ to be larger. Thus $\lambda_{T,b} = 90$ μm is likely to be a low estimate at the heated area A_h of the bottom plate. Further, it is unknown how the growing vapor bubbles modify the 1-phase BL. Nonetheless, we expect that the observed maximum bubble sizes (of order several hundred μm, see the end of section 2.4.1) are significantly larger than $\lambda_{T,b}$ and that only a part of the surface of a fully grown bubble is exposed to temperatures above T_{on}. Even when bubbles are first formed, their size presumably is determined by the 30 μm diameter of the cavities (see figure 2.3), and in the BL a significant temperature drop is expected to occur over such a distance.

A bubble can grow by removing heat from the bottom-plate (silicon-wafer) surface, and from the part of the liquid adjacent to it where the temperature is above T_{on}. In the upper portion of and above the BL the time-averaged liquid temperature is below T_{on} (see figure 2.10b below for instance), bubbles release heat into the liquid, and condense. While attached to the nucleation site, the growth exceeds or is equal to the condensation; after detachment as the bubble travels upward through the bulk of the fluid there is only condensation until the bubble vanishes. For most parameter values the top plate is never reached, thus avoiding the formation of an extended vapor layer below it. Any dissolved air released into a bubble during the nucleation process then will also be recycled into the fluid and does not escape from the system.

Nusselt-number results

The Jakob number Ja (Eq. (2.3)) is the ratio of the available thermal energy to the energy ("latent heat") necessary for the liquid vaporization to occur. Although its relevance to the present process is not straightforward since we argued that much of the heat of vaporization is extracted from the bottom plate and superheated liquid within only part of the BL, we think that it still provides a useful indication of the efficiency of the process at the bottom plate and allows for comparison with results from other researchers. Thus, in figure 2.8a, Nu is plotted as a function of T_b (lower abscissa) and Ja (upper abscissa), for both 1-phase (solid symbols) and 2-phase (open symbols) flow.

We note that for 1-phase flow $Nu \simeq 700$. This is much larger than the result for classical RBC at the relevant $Ra \simeq 1.8 \times 10^{10}$, which is $Nu \simeq 156$ [79; 86]. The reason for this is that in Eq. 2.5 we used the area $A_h = 4.9$ cm^2 to define Nu, rather than the entire bottom-plate area $A = 62.1$ cm^2. If we had used A, the result would have been $Nu \simeq 61$, which is smaller than the classical result. One can argue that, at lowest order, Nu is proportional to the inverse of a thermal resistance (given by the inverse of λ_{eff}, see Eq. 2.5) which in turn is the sum of two resistances, one corresponding to that of the top and the other to that of the bottom boundary layer [87], and that in our case A should be used at the top and A_h is relevant to the bottom. In addition, in Eq. 2.5 one has to consider that the temperature drop, normalized by ΔT, across the bottom (top) BL is 0.74 (0.26), see figure 2.10b below. One then finds $Nu = 189$ which, considering the approximations involved in the lowest order model that we used, can be regarded as consistent with the classical result.

The results in figure 2.8a are for the wafers listed in table 2.1 with different cavity spacings and cavity densities. Note that 1- and 2-phase data sets plotted using the

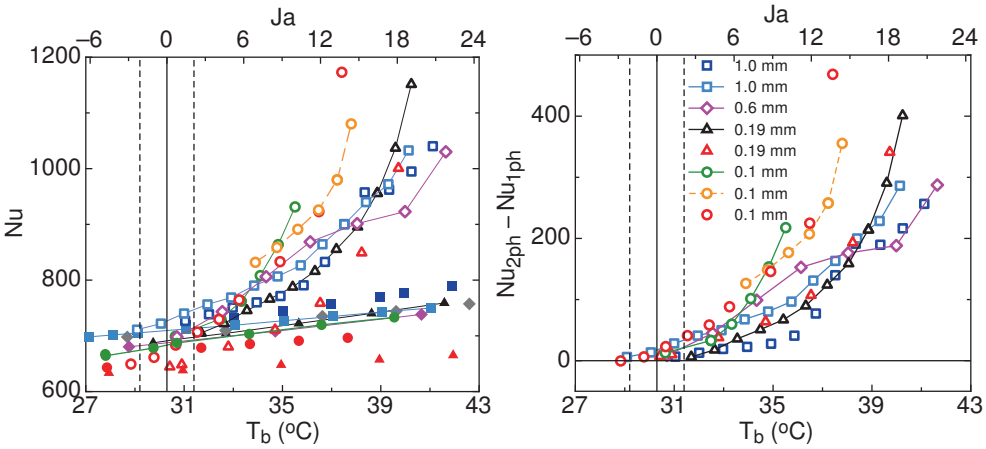

Figure 2.8: (a): The Nusselt-number Nu for 1- and 2-phase flow and (b): The Nu difference $Nu_{2ph} - Nu_{1ph}$ between 1- and 2-phase flow as a function of the bottom-plate temperature T_b and the Jakob number Ja. In (a) solid points represent 1-phase and open symbols 2-phase flow. Data points with the same color and symbol are for the same data set. Data from different cavity separations l are indicated in (b). Besides the color difference between runs, to distinguish between two data sets measured using the same wafer the points are connected by a line (solid or dashed). The vertical solid line corresponds to $T_b = T_{on}$. The vertical dashed lines correspond to $T_{on} \pm \sigma_{T_{on}}$ where $\sigma_{T_{on}}$ is the standard deviation of the T_{on} measurements.

same color and the same symbol were measured using the same liquid, since the fluid remained inside the cell throughout both sets. Two 2-phase sets each with $l = 1$ mm and $l = 0.19$ mm, three for $l = 0.1$ mm, and one for $l = 0.6$ mm were measured. Before each of these the cell had been emptied and refilled, and in going from one cavity spacing to another the cell had been taken apart and re-assembled with a different bottom plate. The 1-phase measurements showed reasonable reproducibility.

Data obtained with $l = 2.0$ mm are excluded from figure 2.8 because Nu_{2ph} was only a little larger than Nu_{1ph} due to the fact that only very few sites were active. However, these data will be shown below in figure 2.9b. As for all cavity spacings, some sites remained active as T_b was reduced and some deactivated. Interestingly, for $l = 2.0$ mm we noted that some inactive sites at a given T_b activated again at a lower T_b. This may be due to dissolved air coming out of solution and forming a new nucleating site or due to a detached bubble from a neighboring site which anchored at a nearby inactive site, activating it.

All 2-phase data sets show an enhancement of the heat transport relative to the 1-phase data. In all cases the measurements are consistent with the same onset at $T_{on} = 30.3 \pm 1.1°\text{C}$. This temperature is lower than the saturation temperature of the pure liquid at the pressure prevailing in the sample, which is $T_\phi = 38.5°\text{C}$. The

1-phase Nusselt-number results increased with T_b (or Ja) since the thermal forcing, as expressed by the Rayleigh number Ra, also became larger with increasing T_b.

Each of the eight 1-phase Nu data sets were fitted over the range $26°C < T_b < 43°C$ by a third-order polynomial and the fitted values were averaged. The standard deviation from this averaged function increased with T_b; it varied from 3.5% to 5.5% of Nu. Any small systematic differences between different sets presumably were due to differences of the dissolved-air concentration and to small variations in the bottom-plate assembly.

By taking the difference between Nu_{2ph} and the value of the corresponding polynomial fit to Nu_{1ph} we obtained the heat-flux enhancement $\delta Nu \equiv Nu_{2ph} - Nu_{1ph}$ for each data set, as shown in figure 2.8b. For all wafers the enhancement increased with T_b or, equivalently, with Ja. For instance, at $T_b \simeq 37°C$ we found $\delta Nu \simeq 250$, which is about 35% of Nu_{1ph}.

The data in figure 2.8 show that the heat-flux enhancement did not have a strong systematic dependence on the cavity density, even though this density varied by a factor of about 59 (see Table 2.1). Similarly, in the numerical work in Ref. [70], changing the number of bubbles present in boiling RB flow at $Ra = 5 \times 10^9$ by a factor of 15 did not increase the heat-flux enhancement proportionally but only increased it by a factor of approximately two. Ref. [70] also reported that the relative effect of the vapor bubbles on the heat flux was a decreasing function of Ra, where the smallest Ra in their simulations was 2×10^6. Since our measurements were made at a constant ΔT and thus an only slightly varying Ra, we have no information on the Ra dependence of $\delta Nu/Nu_{1ph}$.

In figure 2.9a we show the data from figure 2.8b as open symbols on a logarithmic scale as a function of $T_b - T_{on}$ on a linear scale. Also shown, as solid symbols, are the same data divided by the corresponding total number N of etched cavities. Note that for increasing $T_b - T_{on}$ an increasing number of sites turned inactive, at a rate that varied depending on the cavity separation. All solid-symbol curves for $l = 0.10$ mm and $l = 0.19$ mm fall on top of each other for most of the measured range. The two $l = 1.0$ mm curves are very similar above $T_b - T_{on} > 7$ K and deviate from each other for smaller superheat, probably due to the deactivation of more or less sites in each run as T_b decreased or due to a slightly different dissolved air content in the liquid. The heat-flux enhancement per cavity for $l = 0.60$ mm was between the ones for $l = 1.0$ mm and $l = 0.10, 0.19$ mm.

It is only at the largest superheat values for each cavity separation that all or nearly all etched cavities were equally active (except for $l = 2.0$ mm) and it is under this condition that the number of active sites N_a is equal or very close to the total cavity number N. We chose heat-flux-enhancement data-points obtained for superheats $T_b - T_{on} > 9.3$ K so that for wafers with $l = 1.0, 0.60$ and 0.19 mm we had $N_a \simeq N$. From images taken for each data point with $l = 2.0$, 1.0 or 0.60 mm we extracted N_a from average intensity images (similar to figure 2.5) either by subtracting from N the number of sites that were observed to be inactive, or by counting the total number of active sites directly. For $l = 0.19$ mm we assumed that all sites were active, consistent with what was observed (see figure 2.5a). In figure 2.9b the heat-flux enhancement per active site is plotted as a function of superheat. Table 2.2 contains the N_a value corresponding to each data point, as well as the number of images

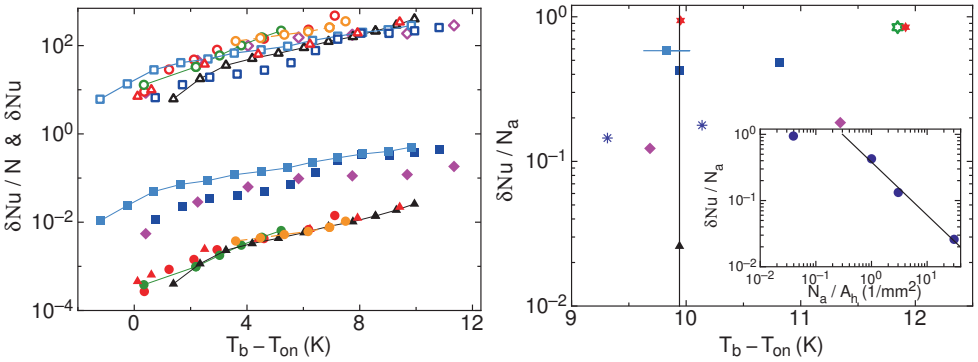

Figure 2.9: (a): The Nusselt-number difference $\delta Nu = Nu_{2ph} - Nu_{1ph}$ (open symbols as in figure 2.8b) and the corresponding Nusselt-number difference per cavity $\delta Nu/N$ (with the same symbols and colours but solid) on a logarithmic scale as a function of $T_b - T_{on}$ on a linear scale. (b): The Nusselt-number difference per active site $\delta Nu/N_a$ on a logarithmic scale as a function of $T_b - T_{on}$ on a linear scale. The vertical line indicates the value $T_b - T_{on} = 9.9$ K. Symbols: $l = 2.0$ mm (open and solid hexagonal stars), 1.0 mm (squares with and without horizontal line), 0.60 mm (diamonds), 0.60 mm with blocking ring (stars) and 0.19 mm (triangles). Inset: $\delta Nu/N_a$ at $T_b - T_{on} = 9.9$ K as a function of the active cavity density N_a/A_h on double logarithmic scales. The solid line is a power-law fit to the three points at largest N_a/A_h which yielded an exponent of -0.80.

considered and the total time over which these were acquired. For $T_b - T_{on} > 9.3$ K the typical bubble departure frequency from the bottom plate was of the order of 10 per second. Therefore taking images of the active sites for 2 seconds or more was sufficient to capture each of the active sites. Note that the superheat range of data taken with $l = 0.10$ mm did not reach such large values and the $l = 0.10$ mm data are therefore not included in the plot; the reason is that the temperature drop across the bottom plate $T_b^\star - T_b$ with $l = 0.10$ mm was larger (due to a larger heat-flux) than for the other wafers, see section 2.3.3. For $l = 2.0$ mm interference between bubbles from adjacent nucleating sites was weak or absent, and the corresponding normalized Nusselt enhancement $\delta Nu/N_a$ is essentially that of a single and isolated nucleating site under the influence of the turbulent convective flow. Also shown is one data set measured with $l = 0.60$ mm with a ring around the etched area (stars), which is discussed in section 2.4.5.

In order to study the dependence of δNu on the site density more quantitatively, we fixed the superheat at $T_b - T_{on} = 9.9$ K (the vertical line in figure 2.9b), and plotted the Nusselt-number difference per active site $\delta Nu/N_a$ as a function of active site density N_a/A_h as shown in the inset of figure 2.9b on double logarithmic scales. The three data points for the largest N_a/A_h were fitted by a power law which yielded an exponent of -0.80, showing that for decreasing active site density, or equivalently for

l [mm]	$T_b - T_{on}$ [K]	Symbol in fig. 2.9b	N_a	No. of Images / time [s]
2.0	11.85	open star	45	45 / 64
	11.92	red star	27	102 / 2
	9.95	red star	20	1811 / 7.3
1.0	10.82	square	534	64 / 22
	9.95	square	507	64 / 22
	9.83	connected square	491	521 / 2.1
0.6	11.35	diamond	1550	2 × 16 / 4 (sets 12 hours apart)
	9.68	diamond	1530	2 × 16 / 4 (sets 12 hours apart)
	10.14	purple star	1565	1031 / 2.02
	9.31	purple star	1561	1324 / 2.65
0.19	9.94	triangle	15460	32 / 8

Table 2.2: Center-to-center spacing l, the bottom plate superheat $T_b - T_{on}$, symbol used in figure 2.9b, number of active sites N_a, and the total number of images acquired over the acquisition time used to determine N_a.

increasing cavity separation, the contribution to the total heat-flux enhancement per active site becomes larger. The exponent implies that $\delta Nu \propto N_a^{0.20}$. It is interesting to note that this result is consistent with the numerical work of Ref. [70]. Those authors found that increasing the number of bubbles injected into the RB flow by a factor of 15 increased δNu only by a factor of two or so. Our result would imply a factor of $15^{0.20} \simeq 1.7$.

The data point at the smallest N_a/A_h shows that the heat-flux enhancement per active site eventually saturates for a small enough cavity density, as one would expect for a non-interacting active nucleating site. For the superheat of 9.9 K the data give a saturation value close to $\delta Nu/N_a \simeq 1.0$.

2.4.3 Temperature measurements

The thermistors inserted through the side wall into the flow (see figure 2.1b), measured local temperatures along the vertical axis ($x/D = 0$) at heights of $0.28L$ and $0.50L$. These temperatures are denoted as 'cb' (center-bottom) and 'cc' (center-center), respectively. The measurements for both wafers with $l = 1.0$ mm and $l = 0.60$ mm were sampled at a frequency of 0.25 Hz, and the data for $l = 0.19$ mm at a frequency of 16 Hz. To acquire sufficiently good statistics, the measurements at 0.25 Hz were made over typically 24 hours once a statistically stationary state was reached, which yielded of order 2×10^4 points. The 16 Hz measurements were acquired over approximately 5 hours, thus collecting 2×10^5 data points. The data were used to compute time-averaged temperatures T_{cc} and T_{cb} and the temperature probability-distribution functions.

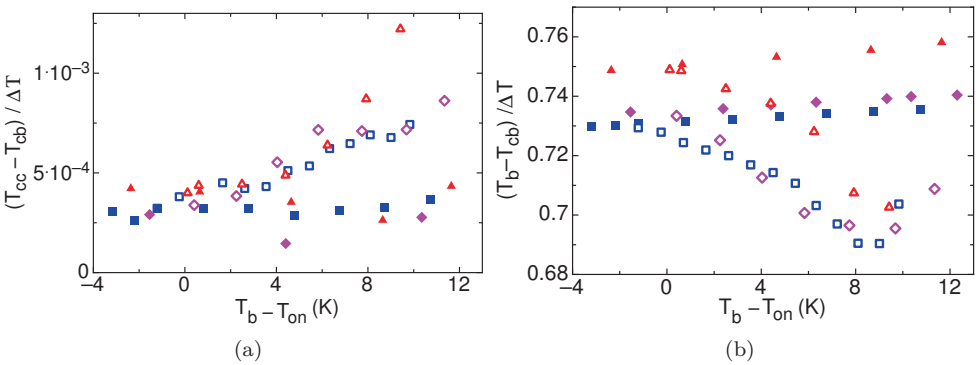

Figure 2.10: In (a) temperature difference $T_{cc} - T_{cb}$, normalized by ΔT, as a function of $T_b - T_{on}$ and (b): the normalized temperature difference across the bottom 0.28 of the cell height. Solid symbols: 1-phase data. Open symbols: 2-phase data. Triangles: $l = 0.19$ mm. Diamonds: $l = 0.60$ mm. Squares: $l = 1.0$ mm.

Time-averaged temperatures

In figure 2.10a we show the normalized temperature difference $(T_{cc} - T_{cb})/\Delta T$ in the bulk of the sample. For the 1-phase case (solid symbols) this variation is seen to be quite small (about 0.03% of ΔT), as is the case also for the classical RBC geometry [81; 88; 89]. As in classical RBC with $4.4 \lesssim Pr \lesssim 12.3$, the gradient was found to be stabilizing. The 2-phase flow enhances the gradient, with the excess, due to the heat carried by the bubbles, varying about linearly with $T_b - T_{on}$ (see also section 2.4.4 below). However, the temperature difference remained quite small and generally was below 0.1% of ΔT.

In figure 2.10b the normalized vertical temperature difference $(T_b - T_{cb})/\Delta T$ across the bottom part of the sample (up to $z/L = 0.28$) is shown as a function of $T_b - T_{on}$ for both 1-phase and 2-phase flow. It is about three orders of magnitude larger than the temperature variation in the bulk (see figure 2.10a) because it includes the bottom boundary layer which, although estimated to be thin (90 μm to lowest order), sustains a major part of the applied temperature difference. For 1-phase flow the mean temperature T_{cc} at the sample center was smaller than T_m, as opposed to classical RBC where [in the Oberbeck-Boussinesq approximation [90; 91]] the center of the sample is at T_m. For our 1-phase experiment $(T_m - T_{cc})/\Delta T \simeq 0.24$. Since the temperature difference across the bulk was small, almost all of the shift of T_{cc} relative to T_m was due to different temperature drops across the boundary layers near the top and bottom plates. The shift is, of course, almost entirely a consequence of the difference between the area over which the heat current could enter the sample at the bottom and that over which it could leave it at the top. The result also implies that in 1-phase flow both T_{cc} and T_{cb} remained on average below T_{on} over the entire range of T_b.

From figure 2.10b it is apparent that vapor bubbles increased the local mean

temperature in the bulk of the sample, or equivalently, reduced $(T_b - T_{cb})/\Delta T$. From the small values of $(T_{cc} - T_{cb})/\Delta T$ shown in figure 2.10a, as well as from the data shown in figure 2.10b, one sees that this increase was nearly the same at the two vertical positions in the bulk. Thus, the increase occured primarily in or near the boundary layer above the bottom plate. We note that the mean temperatures in the 2-phase flow at $z/L = 0.50$ and $z/L = 0.28$ were above T_{on} only for the largest $T_b - T_{on} \simeq 11.35$ K, and then only by about 0.3 K.

Standard deviations of temperatures

The standard deviations (Eq. (2.6)) of the local temperatures from their mean at $z = 0.28L$ and $0.50L$, normalized by ΔT, are plotted as a function of $T_b - T_{on}$ in figures 2.11a and 2.11b, respectively. Over the entire range of $T_b - T_{on}$ the standard deviations for the 1-phase flows were larger at $z = 0.28L$ than they were at mid-height. At both locations the standard deviation was reduced by the presence of vapor bubbles. Although this reduction was not very large at $z/L = 0.5$, at $z/L = 0.28$ it reached almost a factor of two for the largest $T_b - T_{on}$.

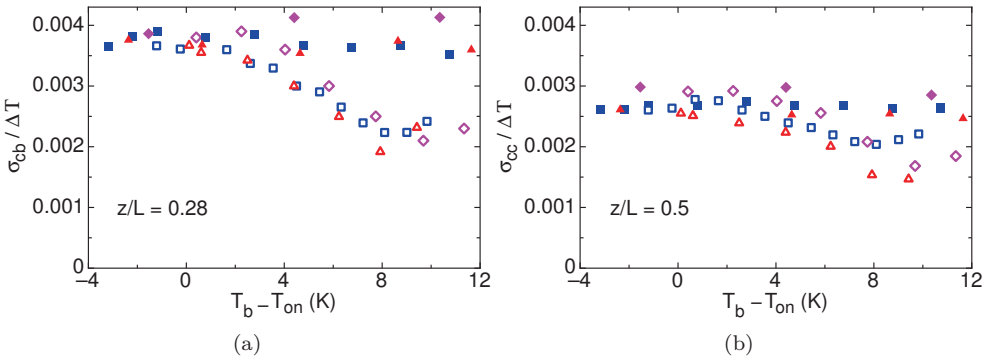

Figure 2.11: Normalized standard deviations from the mean of the temperatures on the sample center line at different heights (see labels) as a function of $T_b - T_{on}$. (a): σ_{cb} and (b): σ_{cc}. Symbols as in figure 2.10.

Comparison of the data in figure 2.11a and 2.11b with those for $(T_{cc} - T_{cb})/\Delta T$ in figure 2.10a shows that the standard deviations were larger than the differences between the mean temperatures at $0.50L$ and $0.28L$. By comparing figures 2.11a and 2.10b one sees that the normalized temperature difference across the bottom 0.28 of the cell height and the normalized temperature standard deviation at $z/L = 0.28$ had similar dependences on $T_b - T_{on}$ for both 1-phase and 2-phase flow, even though they differ in size by over two orders of magnitude.

According to Refs. [68; 71], bubbles have a two-fold effect on the flow fluctuations. On the one hand, due to their fixed surface temperature bubbles tend to smooth the liquid temperature differences by absorbing or releasing heat, thus leading to less intermittency in the thermal fluctuations [71]. On the other hand, due to their

buoyancy moving bubbles agitate the flow, thereby enhancing mixing of the thermal field, and add vertical momentum to it. The thermal feedback provided by the bubbles explains the observed temperature standard-deviation reduction as $T_b - T_{on}$ increased up to about 8 K. For even larger superheats the reduction remained about constant.

Temperature probability distributions

In classical RBC one expects on the basis of symmetry arguments and indeed finds from experiment (see, e.g., Ref. [92]) that the skewness S (see Eq. (2.7)) vanishes at the sample center. It is known to be positive along the center line closer to the bottom plate. This positive skewness is attributed to the effect of hot plumes emitted by the bottom-plate boundary layer which influence the bottom portion of the sample but then travel mostly close to the side wall where they rise toward the top while cold plumes descend near the wall on the opposite side.

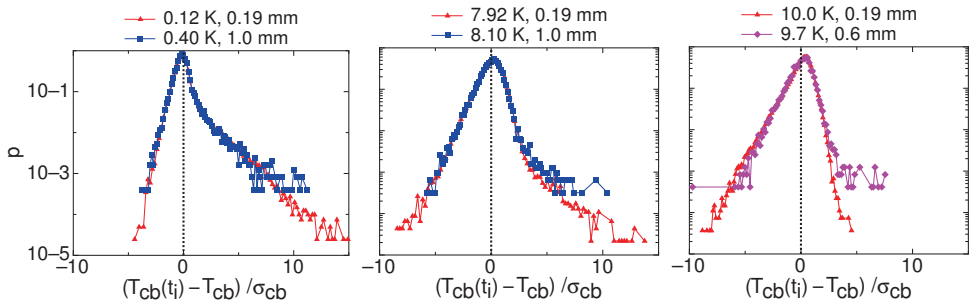

Figure 2.12: Probability-density functions p of $(T_{cb}(t_i) - T_{cb})/\sigma_{cb}$ for time series of 2-phase flow (where $T_{cb}(t_i)$ is the instantaneous value of the time series at time t_i) measured at $z/L = 0.28$ for superheats $T_b - T_{on}$ and cavity separations l as shown in the labels. The vertical dotted lines are located at $(T_{cb}(t_i) - T_{cb})/\sigma_{cb} = 0$.

Our sample was not symmetric about the horizontal mid plane and there was no reason for S to vanish at the sample center. Indeed, the time series for both T_{cc} and T_{cb} of 1-phase flow, and of 2-phase flow with modest $T_b - T_{on}$, had probability distributions with positive skewness. However, for 2-phase flow S became smaller and eventually negative at large $T_b - T_{on}$. Examples of distributions at $z/L = 0.28$ with different $T_b - T_{on}$ are shown in figure 2.12. In each subfigure two data sets at similar superheat values are shown. They were taken at different acquisition rates (see section 2.4.3) using wafers with different cavity spacings. One sees that the cavity spacing and acquisition rate had no significant influence, except that the distributions for $l = 0.19$ mm have longer tails due to the larger number of points in the time series.

In figures 2.13a and 2.13b we show S as a function of $T_b - T_{on}$ for 1-phase and 2-phase flow, respectively. For 1-phase flow and 2-phase flow with modest superheat, up to $T_b - T_{on} \lesssim 6$K, the results are very similar. Along the sample centerline $2 \lesssim S \lesssim 4$ and only weakly dependent on $T_b - T_{on}$. The reason for the relatively large value of S

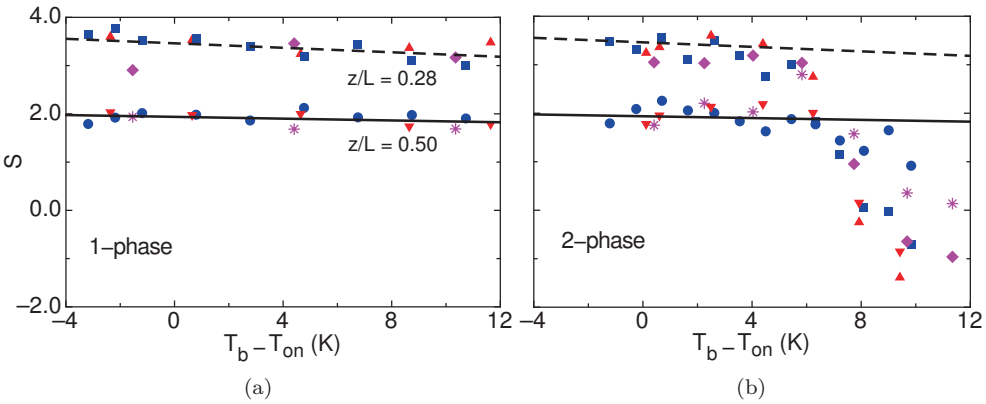

Figure 2.13: The skewness S of the probability distributions of temperature time-series measured at the locations 'cb' ($z/L = 0.28$) and 'cc' ($z/L = 0.50$) as a function of the bottom-plate superheat $T_b - T_{on}$ of (a): 1-phase flow and (b): 2-phase flow. Squares, diamonds and up-facing triangles: 'cb'. Circles, stars and down-facing triangles: 'cc'. Stars and diamonds: $l = 0.60$ mm. Squares and circles: $l = 1.0$ mm. Up- and down-facing triangles: $l = 0.19$ mm. In (a) and (b) straight-line fits to 1-phase 'cb' (dashed line) and 'cc' (solid line) data for the three l.

was, we believe, that the plumes emitted from the more localized heat source in our geometry tended to travel more nearly vertically and thus influenced the temperature distribution even at the geometric center of the sample. We note that S measured at $z/L = 0.50$ was smaller than at $z/L = 0.28$, as one would expect if the plumes disperse laterally as they travel upward. For each height S was fitted as a function of $T_b - T_{on}$ by straight lines, as shown in figure 2.13 by solid and dashed curves.

As $T_b - T_{on}$ increased beyond about 6 K for 2-phase flow, S decreased and at the largest $T_b - T_{on}$ became negative. The decrease of S (measured relative to S of 1-phase flow) was larger closer to the heated surface where bubbles were bigger. One sees that the thermal capacity of the bubbles homogenized the temperature field in the bulk, thereby reducing the temperature gradients associated with plumes. It is somewhat surprising that for all data sets the decrease of S began relatively suddenly as $T_b - T_{on}$ exceeded about 6 or 8 K, with no noticeable effect for smaller $T_b - T_{on}$. This phenomenon warrants further investigations.

2.4.4 Correlated quantities

In this section we show how the heat-flux difference between 1- and 2-phase flows (see figure 2.8b) was correlated with locally measured quantities.

The normalized local temperature increase

$$\delta T_{cc}/\Delta T \equiv ((T_b - T_{cc})/\Delta T)_{2ph} - ((T_b - T_{cc})/\Delta T)_{1ph} \tag{2.8}$$

due to bubble nucleation at the vertical location 'cc', and the similarly defined δT_{cb}

for 'cb' (see figure 2.10b), were determined by fitting straight lines to each of the 1-phase data sets and obtaining the differences between the corresponding 2-phase measurements and these fits. Note that ΔT did not have exactly the same value in 1- and 2-phase flow due to temperature corrections (see section 2.3.3). In figure 2.14a $\delta T_{cc}/\Delta T$ and $\delta T_{cb}/\Delta T$ are both plotted as a function of $T_b - T_{on}$. One sees that they are nearly indistinguishable from each other in the figure. The results obtained for the three different cavity separations were close to each other except for $T_b - T_{on} \gtrsim 8$ K, when the $l = 0.60$ and 1.0 mm data sets reversed their trends but the 0.19 mm data set kept a decreasing $\delta T_{cc}/\Delta T$ trend.

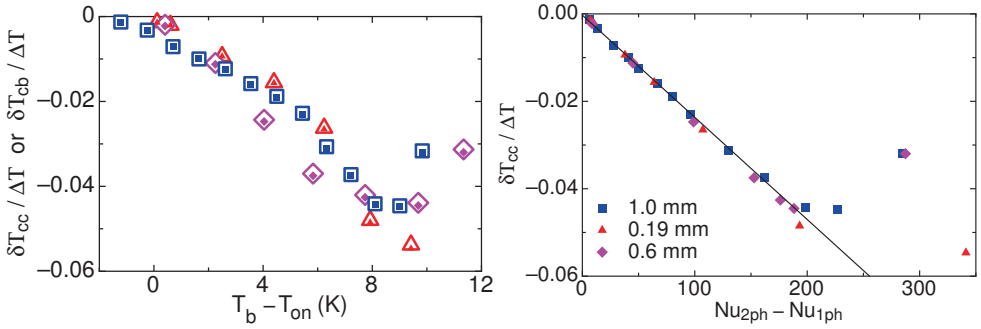

Figure 2.14: (a): The normalized differences $\delta T_{cc}/\Delta T$ (solid symbols) and $\delta T_{cb}/\Delta T$ (open symbols) between 2- and 1-phase flow of $(T_b - T_{cc})/\Delta T$ and $(T_b - T_{cb})/\Delta T$ as a function of $T_b - T_{on}$. The results for 'cb' and 'cc' are nearly identical. Symbols (open and solid) for different cavity spacings l are as in (b). (b): The normalized difference $\delta T_{cb}/\Delta T$ as a function of the Nusselt-number difference between 2-phase and 1-phase flow. The straight line in (b) is a fit (forced through the origin) to $Nu_{2ph} - Nu_{1ph} \lesssim 190$ data for $l = 1.0$ mm.

In figure 2.14b the normalized temperature difference between 2- and 1-phase flow at $z/L = 0.28$ is shown as a function of the heat-flux enhancement. One sees that these two quantities were correlated. In view of the results shown in figure 2.14a the same relationship was found also for $z/L = 0.5$. In the $\delta T_{cc}/\Delta T$ range between 0 and about -0.05 (or equivalently $T_b - T_{on} \leq 8$ K) and $\delta Nu \lesssim 190$ the data are consistent with a straight line passing through the origin. Separate fits to the data for $l = 1.0$ mm, $l = 0.60$ mm, and $l = 0.19$ mm gave slopes of $-(2.34 \pm 0.02) \times 10^{-4}$, $-(2.39 \pm 0.03) \times 10^{-4}$, and $-(2.52 \pm 0.01) \times 10^{-4}$ respectively. For $\delta Nu \gtrsim 190$, $\delta T_{cc}/\Delta T$ reversed its trend for $l = 1.0$ mm and $l = 0.60$ mm. It decreased further for $l = 0.19$ mm, albeit not with the same linear dependence as for $\delta Nu \lesssim 190$. For this case of largest $\delta T_{cc}/\Delta T$ also the largest value of δNu was reached.

In the presence of bubbles the normalized bulk temperature difference between $z/L = 0.5$ and $z/L = 0.28$ (see figure 2.10a), although quite small, increased with increasing $T_b - T_{on}$. To quantify the effect of the bubbles on the bulk temperature, a straight line was fitted to each 1-phase data set, and that straight line was subtracted

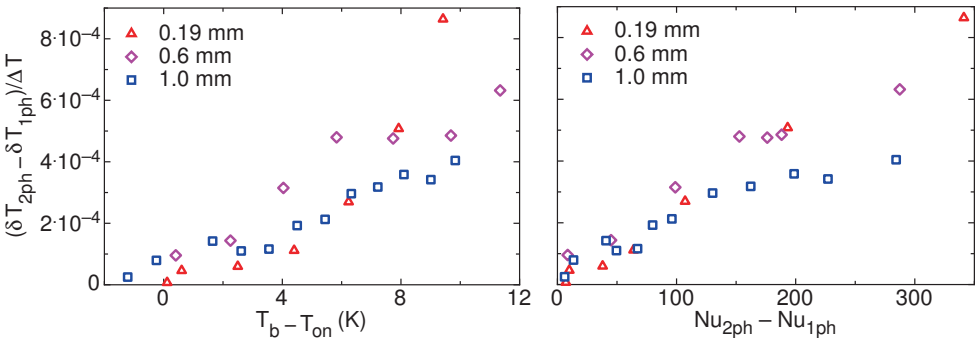

(a) (b)

Figure 2.15: (a): The normalized change $(\delta T_{2ph} - \delta T_{1ph})/\Delta T$ of the temperature difference between the two locations $z/L = 0.50$ and $z/L = 0.28$ due to the bubbles in 2-phase flow (see Eq. (2.9)). (b): The normalized change $(\delta T_{2ph} - \delta T_{1ph})/\Delta T$ as a function of the Nusselt-number difference between 2-phase and 1-phase flow. The cavity spacing l is indicated in the figures.

from the corresponding 2-phase difference. This yielded

$$(\delta T_{2ph} - \delta T_{1ph})/\Delta T \equiv [(T_{cc} - T_{cb})/\Delta T]_{2ph} - [(T_{cc} - T_{cb})/\Delta T]_{1ph} \qquad (2.9)$$

and is plotted in figure 2.15a as a function of $T_b - T_{on}$. The data point at the largest superheat measured for the $l = 0.19$ mm wafer showed a $(\delta T_{2ph} - \delta T_{1ph})/\Delta T$ value nearly twice as large as those measured for the other two wafers at nearly the same $T_b - T_{on}$ value. Figure 2.15b shows the normalized bulk temperature difference between 1- and 2-phase flow as a function of the heat-flux enhancement. The small stabilizing thermal gradient in the bulk became larger with increasing $T_b - T_{on}$ in the presence of vapor bubbles and was positively correlated with the heat-flux enhancement. Note that the largest value of $(\delta T_{2ph} - \delta T_{1ph})/\Delta T$ also corresponded to the largest δNu.

The normalized standard deviations of the temperatures measured at both vertical positions (see figure 2.11) were larger for 1-phase flow than that for 2-phase flow, and that difference was larger at $z/L = 0.28$ than at $z/L = 0.50$. We fitted the 1-phase data sets at each height with straight lines and subtracted the fits from the corresponding 2-phase values to get

$$\delta\sigma_{cc}/\Delta T \equiv (\sigma_{cc}/\Delta T)_{2ph} - (\sigma_{cc}/\Delta T)_{1ph} \qquad (2.10)$$

and similarly we defined and determined $\delta\sigma_{cb}/\Delta T$. The results are plotted as a function of $T_b - T_{on}$ in figure 2.16a. For $T_b - T_{on} \lesssim 8$ K the change due to the vapor bubbles increased with increasing $T_b - T_{on}$ at both heights. For superheats larger than 8 K $\delta\sigma_{cb}/\Delta T$ increased slightly at $z/L = 0.28$ for all l and at $z/L = 0.50$ only for $l = 1.0$ mm.

The dependence on the heat-flux enhancement is plotted in figure 2.16b. Up to $\delta Nu \simeq 200$ a larger heat-flux enhancement was correlated with a larger decrease of

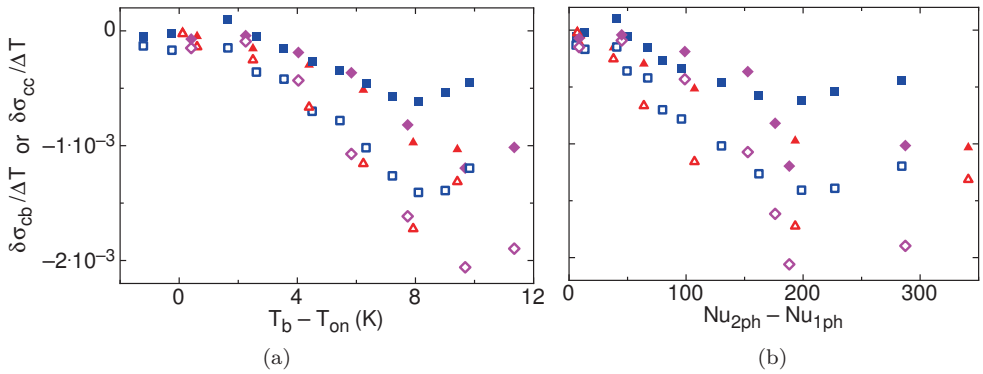

Figure 2.16: (a): The changes $\delta\sigma_{cb}/\Delta T$ and $\delta\sigma_{cc}/\Delta T$ of the normalized standard deviations due to the bubbles of 2-phase flow at $z/L = 0.28$ and at $z/L = 0.50$ as a function of $T_b - T_{on}$. (b): The same changes as a function of the Nusselt-number difference between 2-phase and 1-phase flow. In (a) and (b) open symbols stand for 'cb' and solid symbols designate 'cc' measurements, taken with a cavity spacing $l = 0.19$ mm (triangles), $l = 0.60$ mm (diamonds) and $l = 1.0$ mm (squares).

the temperature fluctuations due to the vapor bubbles. For larger δNu the slope of the correlation between these quantities changed sign.

2.4.5 Large-scale circulation effect

From images of boiling above the bottom plate it was found that, after detaching from the surface, most of the bubbles moved rapidly in nearly the same horizontal direction (see the videos in the supplementary material or upon request). The horizontal displacement found for $l = 1.0$ mm and 0.60 mm was about 2 cm before the bubbles were out of focus due to their vertical motion. The horizontal motion is attributable to the LSC. In order to test whether the bubble growth and heat-flux enhancement were affected significantly by the LSC, a 1.12 cm tall polycarbonate ring (inner diameter of 3.81 cm and wall thickness of 0.64 cm) was positioned with its axis coincident with the sample axis and glued to the $l = 0.60$ mm wafer, see figure 2.17b. In figure 2.17a the Nusselt-number enhancements are shown with and without the blocking ring as stars and open diamonds respectively. The value of T_b at which $Nu_{2ph} - Nu_{1ph}$ reached zero with the ring was larger than it was without the ring by about 2 K. This difference suggests that the dissolved-air concentration in the two cases was slightly different, being larger in the case without the ring.

Taking into account the effects that a larger air concentration in the liquid had on the system and that the data set with ring had a higher superheat value at which all sites became inactive as well as a larger δNu for $T_b - T_{on} > 6$ K as shown in figure 2.17a, we suggests that the bubble nucleation and growth processes were influenced by the LSC (which is assumed to be absent in the presence of the blocking ring). By considering $\delta Nu/N_a$ (see figure 2.9b) with and without the ring we con-

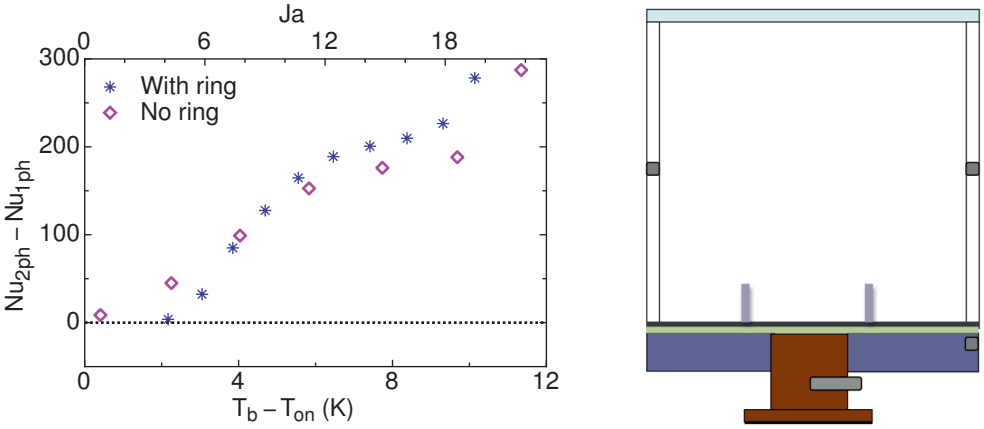

(a) (b)

Figure 2.17: (a) The Nusselt-number enhancement due to vapor bubbles nucleating on a $l = 0.60$ mm wafer as a function of $T_b - T_{on}$ in the presence and absence of a ring around the etched area of the wafer blocking the large-scale circulation, as illustrated in (b) by the thick, short lines emanating from the bottom plate.

firmed that there was an increase in the heat-flux enhancement per active site due to the presence of the ring.

2.4.6 Effect of thermally isolating a heated-liquid column

As discussed in section section 2.4.3, a consequence of having a reduced heating area at the bottom plate was that the temperature drop across the bottom BL was larger than that across the top BL. This asymmetry led to a reduction of the temperature at the sample center below the mean temperature T_m (see figures 2.7 and 2.10b) that is expected in classic RBC in the Boussinesq approximation. Rising bubbles that encounter warmer liquid on their way to the top plate would experience delayed condensation. Delayed bubble condensation would increase the effective flow buoyancy and therefore increase the heat-flux enhancement.

We investigated the effect of thermally and physically isolating the liquid column above the heated area from the liquid outside it by gluing a 0.32 cm thick polycarbonate tube (inner diameter of 2.86 cm and height of 8.5 cm, see figure 2.18b) to the silicon wafer with epoxy. The tube was shorter than the cell by 0.3 cm, thus leaving a gap below the top plate. We performed the same experiments as for the case without the tube. Each panel of figure 2.19 shows the average intensity of 40 images (taken within 56 seconds) of the etched area. In all images part of the tube can be seen in the right bottom corner. As the superheat decreased, an increasing number of sites became inactive. This process started mostly at the outer rim of A_h, but also some sites in the interior of the etched area quit nucleating bubbles. Larger and longer-lasting bubbles, identified as very bright spots, appeared within the etched

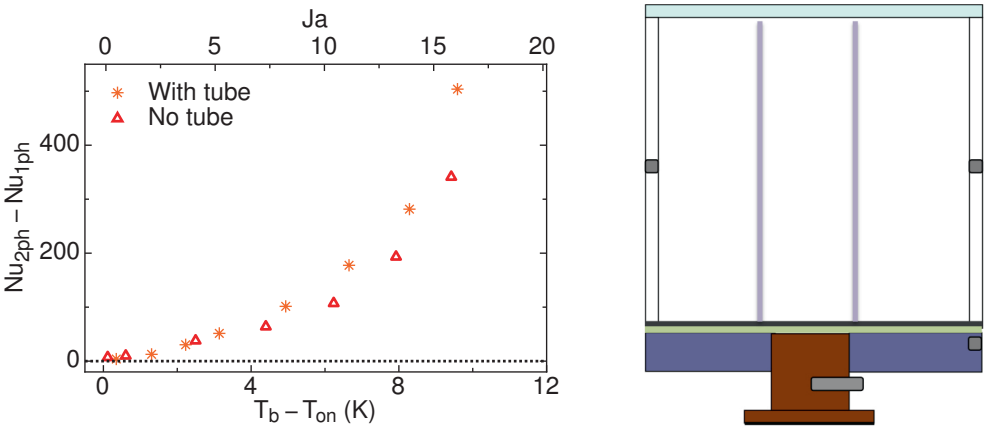

(a) (b)

Figure 2.18: (a) The Nusselt-number enhancement due to bubble nucleation in the absence and presence of a partially thermally insulating $0.97L$ tall tube around the etched area of the $l = 0.19$ mm wafer, as illustrated in (b) by the thick, long lines emanating from the bottom plate.

area. They first formed at the periphery (figure 2.19b) but, as superheat was further reduced, they only formed in the iterior (figures 2.19c and 2.19d).

This particular $l = 0.19$ mm wafer did not show the inner ring of deactivated sites inside the active area that was observed for $T_b - T_{on} = 6.9$ K in figure 2.5.

In figure 2.18a two sets of δNu are plotted as a function of $T_b - T_{on}$. One set was measured with the insulating tube and is compared with one of the data sets presented in previous sections without the tube. The data sets show very similar $T_b - T_{on}$ values at which a few sites were still active before complete deactivation took place at the next lower superheat. This indicates that the dissolved-air concentration in these sets was very similar and that any difference in the heat-flux enhancement between them was not due to a different air content but rather due to a different mechanism responsible for the larger heat transport from bottom to top. A strict comparison between these data sets is only possible for $T_b - T_{on} > 7$ K, since the ring of inactive sites developed for $T_b - T_{on} < 7$ K in the data set without the isolating tube. For 7 K $\lesssim T_b - T_{on} \lesssim 10$ K the difference between the two sets increased as $T_b - T_{on}$ became larger and reached about 160 at the largest superheat where $\delta Nu \simeq 500$ with the tube and $\delta Nu \simeq 340$ without it.

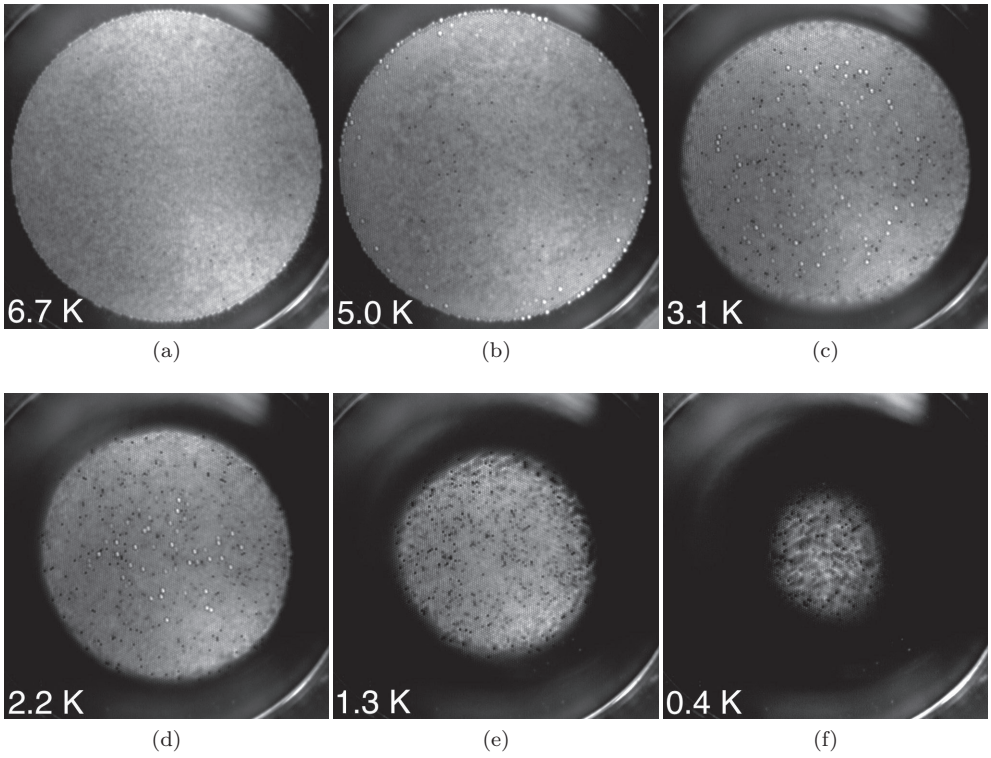

Figure 2.19: Average intensity images of nucleating sites on a $l = 0.19$ mm wafer at different superheat values (see labels). All images cover the same area and show part of the isolating tube at their bottom right corner. In (a) the bright circle corresponds to the heated/etched area A_h with 2.5 cm diameter. Nearly all 15460 sites were active. In (b), (c) and (d) a few larger bubbles (very bright dots) appeared. Starting at (c) sites at the rim of A_h deactivated and this process continued as superheat was further decreased: (d) through (f).

2.5 Summary and conclusions

In this chapter we reported on turbulent convection in an aspect-ratio $\Gamma = 1.00$ Rayleigh-Bénard (RB) cell with and without vapor-bubble nucleation at a locally heated area of the bottom plate. Cylindrical cavities of 30 μm diameter and 100 μm depth and arranged on a triangular lattice, when filled with vapor, served as nucleating sites fixed in space, allowing for well controlled boiling conditions. The working liquid (Novec7000) wetted the wafer surface well and when it filled the cavities, the nucleating sites turned inactive and did not reactivate. Thus direct comparison of 1- and 2-phase turbulent convective flow under the same thermal forcing was possible. The temperature difference across the sample was kept fixed at approximately 16 K while the bottom-plate temperature varied. The Rayleigh number (defined for

1-phase flow) ranged from 1.4×10^{10} to 2.0×10^{10} as the mean sample temperature changed.

We observed nucleating bubbles for $T_b > T_{on} \simeq 30.3$ K. Bubbles nucleating on wafers with a smaller cavity separation l were less susceptible to deactivation at a given superheat value $T_b - T_{on}$. The extreme case was found for $l = 2.0$ mm where, even for superheats larger than usual, only a few cavities randomly located (less than one third of the total number) stayed active, making the interaction with neighbouring active sites negligible. The other extreme cases were cavity separations $l = 0.1$ and 0.19 mm, for which neighbour nucleating bubbles did not grow much before interacting with their neighbours. Typically, this led to merging of several growing bubbles. The large density of the growing bubbles and/or their stronger thermal interactions led to the deactivation of a smaller fraction of cavities. For all wafers an increasing number of cavities deactivated as the superheat values became smaller. For the wafers with cavity separation large enough to optically identify single bubbles ($l = 0.60$, 1.0 and 2.0 mm) we observed that bubbles grew less before departure and the average departure frequency diminished as the superheat values became smaller, which is in accord with the decrease of the global heat flux as the superheat was reduced.

We measured the total heat-flux enhancement, defined as the difference between the Nusselt number of the 2-phase and the 1-phase flow. We found that $Nu_{2ph} - Nu_{1ph}$ depended only weakly on the cavity spacing l. The cavity density, and thus their number, varied by a factor of 59 between the second smallest ($l = 1.0$ mm) and the largest density ($l = 0.1$ mm). However, smaller cavity densities implied less nucleation sites but bigger bubbles, while larger densities meant more sites nucleating smaller bubbles. We conclude that the influence of the bubble number and size on the heat flux nearly cancelled.

The heat-flux enhancement increased with superheat (which can also be expressed in terms of the Jakob number Ja), reaching values up to 50%. The time-averaged heat-flux enhancement per active site $\delta Nu/N_a$ (measured at the higher superheats for which all or most of the sites were equally active) increased with decreasing cavity density until it saturated at $\delta Nu/N_a \simeq 1.0$ for very low density (large separation l). For the higher densities the data could be represented by the power law $\delta Nu/N_a \propto (N_a/A_h)^{-0.80}$. This result implies that $\delta Nu \propto N_a^{0.20}$, which is consistent with the numerical work of Ref. [70] who found that increasing the number of bubbles injected into the RB flow by a factor of 15 increased δNu only by a factor of two or so. Our result would imply a factor of $15^{0.20} \simeq 1.7$.

Bubbles interacted with the Large Scale Circulation (LSC) once they had detached from the hot surface and were dragged horizontally as they also rose due to their buoyancy. This was documented by high-speed movies. By blocking the LSC passage across the nucleating area with a ring around it, the heat-flux enhancement was found to be somewhat larger than measured without a blocking ring. This indicated that the bulk-liquid flow-velocity affected the bubble growth at and the detachment from the surface, which led to a reduction of the heat-flux enhancement.

Measurements of the local temperature along the center line of the sample at two different heights $z/L = 0.50$ and $z/L = 0.28$ showed a stabilizing gradient in 1-phase flow that did not depend on superheat. This normalized gradient was enhanced in the 2-phase flow and was found to be an increasing function of superheat. As a

consequence of the modified RB geometry in our experiments the bottom portion of the cell, up to $z/L = 0.28$, sustained a major part of the temperature difference across the sample. This temperature difference was reduced in the presence of vapor bubbles. The bubbles homogenized the temperature field in the bulk due to their large heat capacity. This was reflected in a decrease of the temperature deviations from the mean (especially closer to the bottom plate) and in the reduction of the positive skewness obtained from the 1-phase temperature distributions. This effect was more significant closer to the bottom plate than at mid-height, which was a consequence of the eventual disappearance of the bubbles as they reached higher levels. The vapor-bubble modification of the mean local temperatures and the temperature standard deviations was found to correlate with the net heat-flux enhancement.

By thermally insulating the liquid column above the heated area with a low thermal conductivity tube we found an even larger heat-flux enhancement. We attribute the increase to bubbles encountering warmer liquid as they rose, thus delaying their condensation and increasing the effective buoyancy of the flow.

Appendix

2.A Epoxy-layer thickness-measurement

Two of the several assembled bottom plates used in this thesis were glued using degassed epoxy. The method yielded an epoxy layer-thicknesses that was not reproducible. Without exactly knowing the epoxy layer-thickness L_e the actual liquid-wafer interface-temperature T_b, and thus the Nusselt-number, could not be determined precisely.

Direct measurements of L_e were not precise enough. Thus we measured L_e indirectly. We placed a copper cylinder with a thermistor embedded in it (acquiring temperature T_c) on top of the silicon wafer glued to the other parts, as shown in figure 2.A.1. The copper cylinder had the same diameter as A_h and its proper alignment with the heated area was secured by using a second plastic ring with the same dimensions as the one of the bottom plate. Clamps forced both the plastic rings and the two copper pieces together, assuring good thermal contact between the silicon wafer and the copper cylinder. This configuration was isolated from room temperature variations and possible convection of surrounding air by adding several layers of thick foam around it (not shown here).

The bottom-plate temperature $T_b^\star$ was controlled by the same digital feedback loop as in the 1- and 2-phase experiments. In order to achieve a significant heat per unit time Q, $T_b^\star$ was set to 35°C while the top cooled to the ambient air. The temperature difference between thermistors $T_b^\star - T_c$ was measured. The thermal resistivities R of all layers were defined in terms of A_h, assuming the heat flowed only across that area. The temperature drop measured is expressed in terms of R of each layer:

$$T_b^\star - T_c = Q(R_b + R_e + R_w + R_c) \tag{2.11}$$

where R_b, R_e, R_w and R_c correspond respectively to the copper piece part of the bottom plate, the epoxy layer, the silicon wafer and the copper cylinder where T_c was measured. Similarly as explained in section 2.3.3, R_w depended on the number N of cavities, in this case filled with air. The silicon wafer net thermal resistivity R_w was obtained by considering the thermal resistivity of the air contained in N cavities $R_a = L_c/(NA_c\lambda_a)$, where λ_a is the thermal conductivity of air. R_w was assumed to be parallel to the fraction of A_h occupied by silicon R_s over the cavities depth L_c; the thermal resistance over the length of the wafer $L_s - L_c$ over which no cavities were etched R'_s was considered to be in series with both R_a and R_s. This gave $R_w = (1/R_a + 1/R_s)^{-1} + R'_s$. No convection took place inside the cavities filled with air. Finally the epoxy layer thickness was computed by substituting $R_e = L_e/(\lambda_e A_h)$

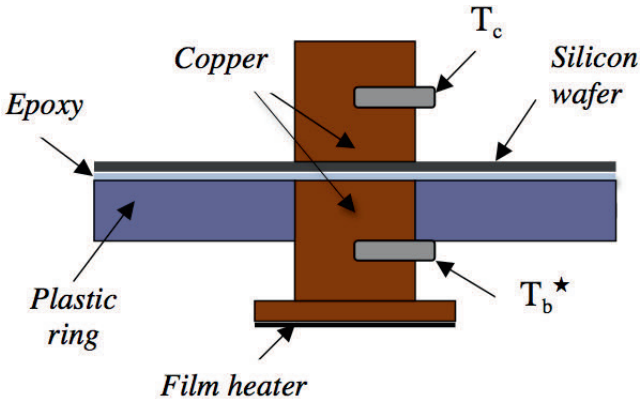

Figure 2.A.1: Sketch of the experimental configuration (vertical dimensions not to scale) for measuring the epoxy layer-thickness that glued the silicon wafer to the copper piece with the plastic ring.

into Eq. (2.11). This method was tested and found to work very well by using a bottom plate assembled with PSA where it yielded an accurate value for the known PSA layer thickness.

2.B Spectral measurements

The measurements of the temperature distribution functions require that the thermistors have a fast enough time response and spacial resolution. To check whether this is the case for the 0.36 mm thermistors used by us, we compared the normalized power spectrum $P(f)$ measured for 1-phase flow with the power spectra obtained by Ref. [82] for the same type of thermistor, and for a bigger and a smaller one with diameters of 1.13 mm and 0.18 mm. In figure 2.B.1 $P(f)$ is plotted for the three thermistors used in their work and for the thermistor we used to acquire data at $z/L = 0.50$ (our results at $z/L = 0.28$ are very similar).

Note that Ref. [82] had a Rayleigh number $Ra \simeq 10^{15}$, nearly five orders of magnitude larger than our $Ra = 2.0 \times 10^{10}$. Further, their Prandtl number was about 0.8, while we have $Pr = 8.2$. For both reasons the turbulence in the flow of Ref. [82] is expected to be more fully developed, with larger Reynolds numbers, than is the case in our experiments. Nonetheless, the spectra suggest that the characteristic time scales in physical units of the two experiments turn out to be similar.

The spectra of all three thermistors used by Ref. [82] showed the same frequency responses up to a critical value $f_{c1} \simeq 0.05$ Hz (see dotted vertical line) beyond which the spectrum of the 1.13 mm diameter thermistor (dotted curve) fell below the other two. Assuming attenuation was due to a diffusive process, the critical frequency of the smaller thermistors should be larger than f_{c1} by the square of the corresponding thermistor size. This assumption yielded the critical frequency $f_{c2} \simeq 0.5$ Hz. Indeed, for frequencies above 0.5 Hz the spectrum of the 0.36 mm thermistor fell below the

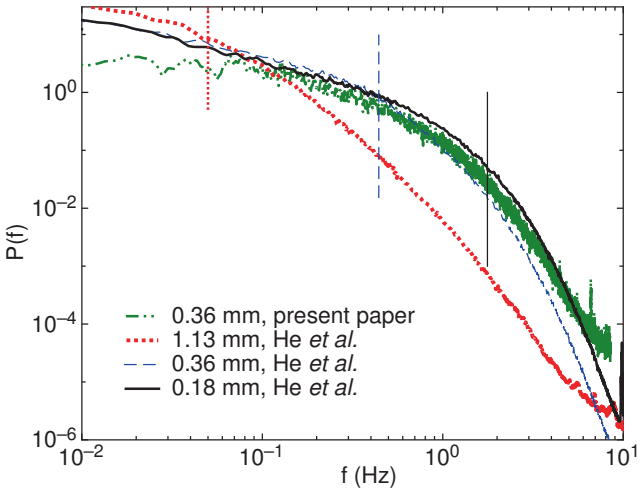

Figure 2.B.1: Normalized power spectra $P(f)$ of $(T-\langle T\rangle)/\Delta T$ from Ref. [82] for thermistors with different diameters (see label). The vertical lines show the frequencies above which the spectrum of the corresponding thermistor is noticeably attenuated due to its thermal response time or size. Also shown are our measurements with a thermistor at $z/L = 0.50$.

spectrum of the smallest one (see dashed vertical line in figure 2.B.1). Using the same argument as in Ref. [82] anticipated the critical frequency of the 0.18 mm thermistor to be $f_{c3} \simeq 2.0$ Hz (solid vertical line).

The spectra obtained from our time series lie between the curves of the 0.36 mm and the 0.18 mm thermistors up to $f \simeq 3.0$ Hz. Thus we are confident that the size of the thermistors we used did not attenuate the spectrum for frequencies below $f_{c3} \simeq 2.0$ Hz. The integral of P(f) in the frequency range $0 < f < 2$ Hz is essentially equal to the total power (the variance) of the signal.

2.C Calculation of dissolved air-concentration

The equilibrium concentration c of a gas dissolved in a liquid is proportional to the partial pressure P of its gas phase as expressed by Henry's Law

$$c = k_H(T)P \ . \tag{2.12}$$

Here k_H is known as Henry's coefficient and is a decreasing function of the temperature T and specific to each gas-liquid pair.

The liquid manufacturer (3M$^{\text{TM}}$) provided the concentration (in volume percentage) of air dissolved in the liquid (Novec7000$^{\text{TM}}$) only at $T = 25°$C and atmospheric pressure P_{atm}. Given that information, we calculated k_H. In order to obtain the concentration of air given the conditions in our experiments we assumed no dependence of k_H on temperature.

The mole number n_l of Novec7000 per unit of liquid volume V_l is

$$\frac{n_l}{V_l} = \frac{\rho_l}{m_l} \tag{2.13}$$

where ρ_l is the liquid density and $m_l = 0.2$ kg/mol is the molecular weight.

Concentration expressed by volume fraction c_V is normally defined as $c_V = V_a/(V_l + V_a)$, where V_a is the volume of air. However the manufacturer provided concentration in volume fraction defined as $c_V = V_a/V_l$. In what follows the definition $c_V = V_a/V_l$ is adopted. The concentration of air in the liquid at $T = 25°\mathrm{C}$ in volume percentage is 31% (internal communication with the manufacturer), therefore $c_V = 0.31$. The vapor pressure curve of the liquid evaluated at $T = 25°\mathrm{C}$ gives $P_v(25°) = 64.6$ kPa, and the partial pressure of air is thus $P_a = P_{atm} - P_v(25°)$.

The mole number of air n_a per unit of liquid volume is obtained from the ideal-gas law

$$\frac{n_a}{V_l} = \frac{(V_a/V_l)P_{atm}}{RT[K]} \tag{2.14}$$

where R is the universal gas constant and $T = 25.0 + 273.15$ K. For this temperature k_H is obtained as

$$k_H = \frac{(n_a/V_l)}{P_a(n_l/V_l)}. \tag{2.15}$$

Using ρ_l at $T = 25°\mathrm{C}$ and P_a, we obtain $k_H = 5 \times 10^{-8}$ mol/(Pa mol).

In our experiments the hydrostatic pressure exerted at the bottom plate was $P_{tot} = 117.6$ kPa. The average temperature at which all nucleation sites became inactive was $T_{on} = 30.3°\mathrm{C}$ ($T_{exp} = T_{on} + 273.15$). From the vapor-pressure curve of the liquid one finds that $P_v(30.3°) = 86.2$ kPa, and thus the partial pressure of air in the interior of a bubble was approximately $P_{a,exp} = 31.4$ kPa, neglecting the pressure drop across the liquid-vapor interface. The liquid in contact with the bottom plate at T_{on} had a density $\rho_{l,on}$, from which $n_{l,exp}/V_l = \rho_{l,on}/m_l$ was calculated.

From eq. 2.15 we solve for n_a/V_l and substitute $P_{a,exp}$ and $n_{l,exp}/V_l$ in the expression to obtain $n_{a,exp}/V_l$. We draw on the ideal-gas law to finally obtain an approximate value of the air concentration expressed as volume fraction for our experiments:

$$c_{V,exp} \simeq \frac{n_{a,exp}}{V_l}\frac{RT_{exp}}{P_{tot}} = 0.23\ . \tag{2.16}$$

Thus the experiments reported here were done with a concentration of air dissolved in the liquid of about 23% by volume. Since $k_H(T)$ is a decreasing function of temperature, we expect 23% to be a lower bound of the air dissolved in the liquid.

3

Vapor-bubble nucleation and dynamics in turbulent Rayleigh-Bénard convection *

Vapor bubbles nucleating at micro-cavities etched on the bottom plate of a cylindrical Rayleigh-Bénard sample (diameter $D = 8.8$ cm, aspect ratio $\Gamma \equiv D/L \simeq 1$ where L is the sample height) were visualized from the top and the side. A triangular array of micro-cavities covered the centered heated area (diameter of 2.5 cm) of the bottom plate. Bubble sizes and frequencies of departure from the bottom plate are reported for a range of bottom-plate superheats $T_b - T_{on}$ (T_b is the bottom-plate temperature, T_{on} is the onset temperature of bubble nucleation) from 3 to 12 K for three different cavity separations. The difference $T_b - T_t \simeq 16$ K between T_b and the top plate temperature T_t was kept fixed while the mean temperature $T_m = (T_b - T_t)/2$ was varied, leading to a small range of the Rayleigh number Ra from 1.4×10^{10} to 2.0×10^{10}. The inverse of the bubble departure-frequency could be described by an exponential decay with increasing superheat, independent of cavity separation. The contribution of the bubble latent heat content to the total enhancement of heat transferred due to bubble nucleation was found to increase with superheat, reaching up to 25%. The bubbly flow was examined in greater detail for a superheat of 10 K and $Ra \simeq 1.9 \times 10^{10}$. The condensation rate of departed bubbles revealed two regimes: the initial rate was associated with steep thermal gradients across the thermal boundary layer near the plate and was two orders of magnitude larger than the final condensation rate once the rising bubbles were in the bulk flow. The dynamics of thermal plumes was studied qualitatively in

*To be submitted as: [Daniela Narezo-Guzmán, Tomek Fraczek, Chris Reetz, Chao Sun, Detlef Lohse and Guenter Ahlers, Vapor-bubble nucleation and dynamics in turbulent Rayleigh-Bénard convection].

the presence and absence of nucleating bubbles. It was found that bubbles enhanced the circulatory motion of plumes across the sample (i.e. the large-scale circulation or LSC). However, the LSC had a characteristic velocity at least one order of magnitude smaller than the bubble-rise velocity in the bulk.

3.1 Introduction

Boiling mechanisms, which promote heat transfer from a hot surface to a liquid, are numerous and intertwined. As a vapor bubble grows on a surface, an increasing amount of latent heat is required to evaporate liquid at the liquid/vapor interface. The latent heat is attainable through different mechanisms: through the bubble cap in the case where the surrounding liquid is superheated, via micro-layer evaporation, and by three-phase contact-line evaporation (see the review in Ref. [23]). The contribution of each of these mechanisms to bubble growth is still a matter of research [75; 76]. As the bubble grows, it causes micro-convection, that is, it perturbs the liquid adjacent to it and disrupts the boundary layer that exists just above the surface. Once the bubble departs from the surface, colder liquid replaces it, enhancing the heat flow due to transient conduction from the hot surface as the liquid rewets it. In addition, a bubble rising in the liquid due to buoyancy carries latent heat with it, and thus effectively transfers heat by advection and augments the effective buoyancy of the flow.

Rayleigh-Bénard flow occurs in a fluid contained within (ideally) adiabatic sidewalls and conducting horizontal top and bottom plates, cooled from above and heated from below. Heat transfer and the flow characteristics of Rayleigh-Bénard turbulence have been studied extensively [56–60]. In this system there are thin boundary layers above the bottom and below the top plate which each sustain approximately half of the applied temperature difference, while the interior (or "bulk") temperature, although fluctuating vigorously, is nearly independent of the location in the time average [see, however, Refs. [81; 93; 94] for a more detailed discussion]. In the bulk there exists a large-scale circulation (LSC) which, for samples with a height similar to its width, takes the form of a single convection roll with a stochastic dynamics that is driven by the small-scale fluctuations of the velocity field [95; 96].

For boiling to occur at the heated bottom plate of a Rayleigh-Bénard convection (RBC) sample while the sample remains filled with liquid (except for the bubbles forming at the bottom plate), it is required that the temperature of the top plate T_t is below the saturation temperature T_ϕ at the prevailing pressure, and that the bottom-plate temperature T_b is above it. The temperature difference $T_b - T_\phi$ is commonly referred to as the superheat. The vapor bubbles form in a boundary layer at the bottom plate and condense as they rise through the bulk of the sample. Depending on whether the mean temperature $T_m = (T_b + T_t)/2$ is well below or close to T_ϕ, one expects the vapor bubbles to condense sooner or later along their rising motion through the bulk. If $T_m = T_\phi$ the bubbles can condense only once they are in the thermal boundary layer at the top plate.

Boiling RBC flow has been studied numerically over the Rayleigh-number (see Eq. 3.1) range $Ra = 2 \times 10^5$ to 2×10^9 and for Prandtl numbers (see Eq. 3.2) $Pr = 1.75$

and 9 [66–71] in RBC samples with aspect ratios $\Gamma \equiv D/L = 1$ and $1/2$ (D is the sample diameter and L its height). Findings of the simulations include flow-structure changes [66; 67] and an effect of the bubbles on both the temperature and the velocity field [67; 69], as well as on velocity and temperature fluctuations [68–71]. More specifically, the numerical simulations found that the mechanical forcing due to rising vapor bubbles increased the velocity fluctuations in the liquid and led to an increase of both the kinetic-energy dissipation-rate and the Reynolds number $Re = u_{rms}L/\nu$ (ν is the kinematic viscosity) based on the root-mean-square fluctuation velocity u_{rms}. The more bubbles were introduced in the flow, the more Re increased. Furthermore, the presence of bubbles in the flow augmented the thermal-energy dissipation-rate due to localized large temperature gradients associated with bubbles since their surface temperature was fixed at the saturation temperature. The bubbles subjected the boundary layers above the bottom and below the top plate to larger thermal and velocity fluctuations, adding to convective effects of the flow. Due to the large heat capacity of the bubbles, sharp temperature fronts in the flow were smoothened, reducing the intermittency of the temperature and velocity fluctuations. One common result in all these papers for Jakob numbers (see definition in Eq. 3.3) $Ja > 0$ was that the heat transfer was enhanced due to the presence of vapor bubbles (2-phase flow) with respect to the case without them (1-phase flow). Vapor bubbles significantly enhanced the heat transport by increasing the strength of the circulatory motion. The heat-flux enhancement was a decreasing function of Ra, and for a given Ra, adding more bubbles into the flow was found to increase this enhancement. All numerical studies focused on the bubble effects on the thermal convection, and the actual heat removal from the plate due to bubble formation was not simulated. Instead, a constant number of bubbles with an arbitrarily chosen initial size of tens of micro-meters was introduced at the bottom plate and the bubbles were free to rise immediately once they were created. The heat required to grow the bubbles to their initial size was assumed to be negligible since the bubbles were small.

The vast majority of experimental studies of RBC kept the sample far from a phase transition. To our knowledge the effect of a phase change on RBC was studied first near the onset of convection (see Refs. [97; 98], and references therein). Studies of *turbulent* RBC in the presence of a phase change were carried out by Ref. [65] for the case of ethane near its vapor-pressure curve. They reported an increase of the effective thermal conductivity when bubble nucleation took place at the bottom plate and, except for the bubbles, the cell was filled with liquid ($T_m < T_\phi$). The effective conductivity became nearly one order of magnitude larger than the effective thermal conductivity for the turbulent 1-phase flow. However, it tended to be irreproducible and time dependent, especially for large superheats. In these experiments, the bottom plate (where bubble formation occurred) was a finely machined copper plate with inhomogeneous-nucleation sites of uncontrolled distribution, size, and shape. Surfaces with random roughness provide an increasing number of active nucleation sites as the superheat is increased [2]; this probably explains the irreproducibility in some of the measurements in Ref. [65].

For even larger superheats and $T_m > T_\phi$, the sample of Ref. [65] was mostly filled with vapor while droplet condensation occurred at the top plate. In that case the effective thermal conductivity measurements were reproducible and time-independent,

and also presented an enhancement which could approach an order of magnitude relative to the 1-phase flow. The authors argued that the droplet formation occurred via homogeneous nucleation in the boundary layer below the top plate.

In chapter 2 heat transport in 2-phase RBC was studied; vapor-bubble formation under well-controlled boiling conditions was achieved by bubble nucleation occurring only at designed micron-sized cavities etched into a silicon wafer that was heated. The classical Rayleigh-Bénard configuration was modified by reducing the heated area to about 1/15 of the total bottom-plate surface in order to avoid uncontrolled bubble nucleation at the small gap between the bottom plate and the cell sidewall. The main focus was the global heat-flux enhancement measured in 2-phase flow with respect to 1-phase turbulent flow. The dependence of heat-flux enhancement on the cavity density and the degree of superheat at the bottom plate was investigated. It was found that the global heat-flux enhancement was an increasing function of superheat (in agreement with the numerical studies by Ref. [70]) and that it had a very weak dependence on the cavity density even though the cavity density varied by a factor of 59. Similarly, Ref. [70] varied the total number of injected bubbles by a factor of 15 at fixed Ra and found a corresponding increase in the global heat-flux enhancement by only a factor of two. The heat-flux enhancement per active nucleating site studied at a large superheat of 10 K did show a dependence on cavity density and it was suggested that the enhancement per active site increased as the cavity density decreased. In the extreme case of very dilute and non-interacting neighboring nucleation sites the enhancement per active site saturated. The local temperature time-series at two different vertical locations in the bulk flow was acquired and it was found that, as the superheat became larger, the bubbles increasingly enhanced the stabilizing thermal gradient, diminished the large temperature difference across the bottom 1/4 of the sample, reduced the temperature fluctuations around the mean value, and lessened the skewness of the temperature probability distributions.

In the present chapter we investigated further the 2-phase RBC flow reported in chapter 2 by means of high-speed imaging from a top view of the nucleation process at the bottom plate. Additionally, we visualized 1- and 2-phase RBC flow (with modified geometry) from the side in a setup especially designed for it. The lateral view of the departing bubbles added crucial information about the bubble shape and volume, and allowed the study of the bubble dynamics once the bubbles departed from the surface and started condensing; this information could not be attained by flow visualization from the top. In addition we gained relevant qualitative information on how the bubbles changed the overall flow. The high-speed recordings partly described in chapter 2 were analyzed quantitatively, carrying through the investigation of bubble growth at and departure from the bottom plate in order to determine how much of the measured global heat-flux enhancement was attributable to bubble growth at the surface; this contribution had been neglected in the numerical simulations of boiling RBC. With this information we estimate separately the actual heat removal from the plate due to bubble formation as one of the mechanisms responsible for heat-flux enhancement. It was then possible to estimate the joint contribution from the other two mechanisms: the effective buoyancy due to rising bubbles (extensively studied in numerical papers) and the micro-convection together with transient-conduction taking place as a consequence of bubble growth and departure.

In the next section of this chapter we will define various quantities needed in further discussions. Then, in section 3.3 we describe the apparatus, measurement and imaging procedures, as well as the image-analysis methods. In section 3.4 we present the results from flow visualization together with results for the bubble-growth contribution to the global heat-flux enhancement. Finally, in section 3.5 we summarize the results and give our conclusions.

3.2 Control and response parameters

For a given cell geometry 1-phase RBC flow depends on two dimensionless variables. The Rayleigh number Ra is the dimensionless temperature difference $\Delta T = T_b - T_t$ between the bottom plate (T_b) and the top plate (T_t) at their interfaces with the liquid and is given by

$$Ra = \frac{g\alpha \Delta T L^3}{\kappa \nu}. \tag{3.1}$$

Here, g, α, L and κ denote the gravitational acceleration, the isobaric thermal expansion coefficient, the cell height, and the thermal diffusivity, respectively. The Prandtl number is the ratio

$$Pr = \nu/\kappa \ . \tag{3.2}$$

Unless stated otherwise, all fluid properties are evaluated at the mean temperature $T_m = (T_b + T_t)/2$.

For samples in the shape of right-circular cylinders like those used here, a further parameter defining the geometry is the aspect ratio $\Gamma \equiv D/L$, where D is the diameter of the cell.

In a system with a single fluid involving a liquid-vapor phase change a relevant dimensionless parameter is the Jakob number

$$Ja = \frac{\rho C_p (T_b - T_\phi)}{\rho_v H} \tag{3.3}$$

where ρ and ρ_v are the densities of liquid (evaluated at T_b) and vapor (at the prevailing pressure) respectively, and C_p is the heat capacity per unit mass of the liquid (evaluated at T_b). In Eq. 3.3 H and T_ϕ are the latent heat of evaporation per unit mass and the temperature on the vapor-pressure curve (at the prevailing pressure), respectively. The Jakob number is the ratio of the sensible heat to the latent heat. The temperature difference $T_b - T_\phi$ is widely referred to as the superheat. In our case dissolved air reduced the boiling point to $T_{on} < T_\phi$. Thus in what follows T_ϕ is replaced by T_{on} in Eq. (3.3) and throughout the analysis.

The response of the system to the imposed thermal driving, or Ra, is reflected in the heat flux from the bottom to the top plate, across the horizontal cross-sectional area A of the sample. It is expressed by the dimensionless Nusselt number

$$Nu = \frac{\lambda_{eff}}{\lambda}. \tag{3.4}$$

Here the effective conductivity λ_{eff} is given by

$$\lambda_{eff} = QL/(A\Delta T) \tag{3.5}$$

where λ is the thermal conductivity of the quiescent liquid and Q is the heat per unit time input to the system. In our case, it was more meaningful to consider the system response expressed in dimensional form by Q. In classical RBC the heated area A_h covers the entire bottom-plate surface and $A_h = A$. Our system was a modified version of classical RBC since only a central circular area smaller than A was heated ($A_h < A$) while the cooling area A_c equaled A.

Another system response is a characteristic velocity amplitude v of the turbulent flow which is described by the dimensionless Reynolds number

$$Re = \frac{vL}{\nu}. \tag{3.6}$$

3.3 Apparatus and Procedures

Precise measurements of heat-flux enhancement due to vapor-bubble formation, as well as imaging of bubble nucleation at the bottom plate from the top, were carried in the apparatus that had been used in chapter 2 (apparatus 1). Bubble nucleation and flow imaging from the side were done in a new apparatus (apparatus 2). Heat-flux measurements in apparatus 2 were not as accurate as the ones in apparatus 1 because the required broad optical access from the side precluded adequate thermal shielding, and are not reported.

The global turbulent RBC flow was visualized from the side using the shadowgraph technique [99–102], which permitted the visualization of the formation and development of both plumes and thermal structures associated with the LSC, and simultaneously of the rising bubbles in the case of 2-phase flow. Focusing on the bubbles from the side provided information about the bubble growth at their nucleation sites and their eventual departure and rise through the bulk of the sample.

3.3.1 Bottom plate and liquid

Each bottom plate consisted of a 10 cm diameter silicon wafer glued to both a copper cylinder with diameter $D_h = 2.54$ cm and to a polycarbonate ring (10 cm outer diameter and 1.26 cm thick), which surrounded the copper cylinder. A metal-film heater was attached to the bottom of the copper cylinder. Nucleation cavities were etched into the up-facing sides of all silicon wafers over a central circular area of 2.54 cm diameter; outside this area the wafers had a smooth surface (3.46-4.22 Å). The roughness of the cavity walls was less than 500 nm. The etched area was located above the heated area $A_h = 5.07$ cm^2 of the copper cylinder. A thermistor (Honeywell type

N	l [mm]	N/A_h [1/mm^2]
142	2.00	0.28
570	1.00	1.12
1570	0.60	3.10

Table 3.1: The total number of cavities N, center-to-center spacing l, and number of cavities per mm^2 N/A_h with $A_h = 507$ mm^2 for the wafers used in this study.

121-503JAJ-Q01) was inserted into the copper piece approximately 1.4 cm below the upper surface and measured $T_b^\star$. For a more detailed description of the bottom-plate configuration, see section 2.3.2.

We used three different wafers with micron-sized cavities on a triangular lattice. Each had a different center-to-center cavity spacing l and thus cavity density, see table 3.1. The cavities had a depth of $100 \pm 5\mu$m and a diameter of $30 \pm 2\mu$m.

The working fluid was the fluorocarbon Novec7000$^{\mathrm{TM}}$(1-methoxyheptafluoropropane) manufactured by 3M$^{\mathrm{TM}}$. At atmospheric pressure it has a boiling temperature of 34°C, which makes it suitable for boiling experiments in our apparatuses. Relevant properties are given as a function of temperature by the manufacturer. In the experiments presented here T_m ranged from 35°C to 18°C. The Prandtl number (see Eq. 3.2) ranged from 7.5 to 8.2 with decreasing T_m. The resulting Rayleigh-number (see Eq. 3.1) ranged from 1.4×10^{10} to 2.0×10^{10}.

3.3.2 Apparatus 1: Heat-current measurements and imaging from above

The experiments for visualizing the vapor-bubble nucleation at the bottom plate from the top were conducted in the apparatus used before (see figure 3.1); details about it are given in Refs. [65; 78–80]. The convection cell consisted of a cylindrical sidewall, either of polycarbonate or acrylic, with a thickness of 0.63 cm. It had a height of $L = 8.8$ cm, and an aspect ratio $\Gamma = 1.00$. The fluid in the cell was confined between a bottom plate (see section 3.3.1) and a 0.635 cm thick, 10 cm diameter sapphire plate on the top. The cooling area extended over the entire top plate. The cell was subjected to a vertical temperature difference by means of a water-cooled top plate and a bottom plate heated over its central 2.54 cm diameter area by a film heater. The temperature of both plates was computer controlled, the top (bottom) plate had milli- (centi-) Kelvin stability.

In practice, the dissipated electrical power of the heater P_Ω equaled the heat current entering the whole system: the sidewall, the actual RBC flow, and any other part of the apparatus. The quantity of interest was the heat current entering the RBC flow. In order to determine it, we made measurements with an empty cell pumped down to a pressure of approximately 3 kPa where convection will not occur in the remaining air. After correcting for the conduction by the quiescent air in the sample cell we refer to this as Q_{sw}. The heat current entering the RBC flow was then given by $Q = P_\Omega - Q_{sw}$. Typically we found $0.16 \lesssim Q_{sw}/Q \lesssim 0.26$, where the ratio decreased for increasing superheat.

3.3.3 Apparatus 2: Imaging from the side

The apparatus for side visualization of the flow was inspired by the work of Ref. [103]. A sketch of the vertical cross section through its center is shown in figure 3.2. It consisted of a cylindrical convection cell which was embedded in a larger volume of fluid contained by square sidewalls in order to reduce the image distortion due to the curvature of the cell walls. Both walls were transparent and the setup allowed for the

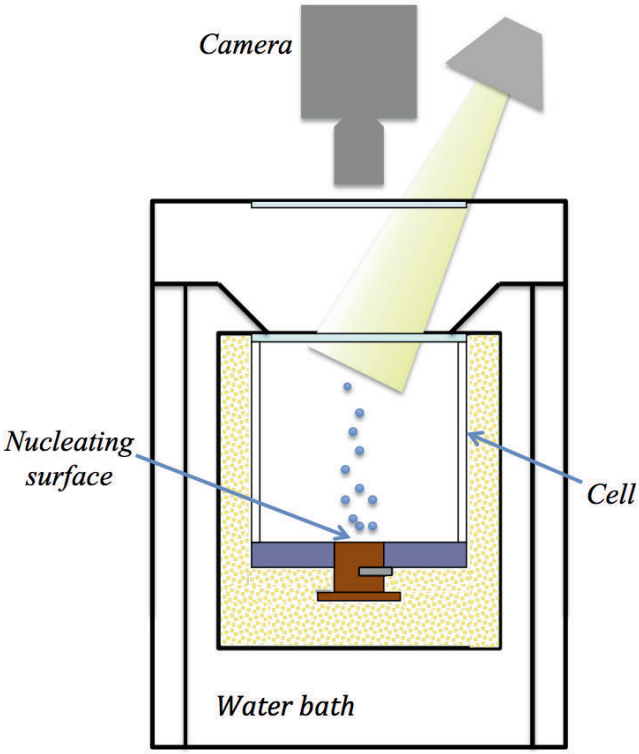

Figure 3.1: Sketch of the cross section of apparatus 1. A transparent sapphire top plate of the cell and the window at the top of the apparatus allowed the illumination and flow visualization through the top; visualization from the side was not possible in this apparatus.

exchange of the bottom plates in order to study 2-phase flow with wafers of different cavity separation l.

The cylindrical sidewall was made of acrylic. It was 8.89 cm heigh, 0.64 cm thick, and had an inner diameter of 10.16 cm ($\Gamma = 1.14$). The square sidewall was made of polycarbonate. The top and bottom round plates of the convection cell were embedded in square plastic (polycarbonate) sheets. The top plate had a diameter of 11.43 cm, was 0.64 cm thick and was made of copper.

The top plate was cooled by a water bath and its temperature was regulated by a cooler/circulator (Neslab RTE 7, Thermo Electronic Corporation) within 0.01 K. A thermistor (same type as the one which measured $T_b^\star$) was inserted into an aluminum tube (L shaped) and measured the water-bath temperature which was assumed equal to the upper-face temperature $T_t^\star$ of the top plate. Both sidewalls were compressed between the bottom and top square sheets, sealing the setup. The bottom-plate temperature was computer controlled and had centi-Kelvin stability. The setup had three adjustable legs that were used to level it.

The square sidewall had two holes close to its bottom and two close to its top on

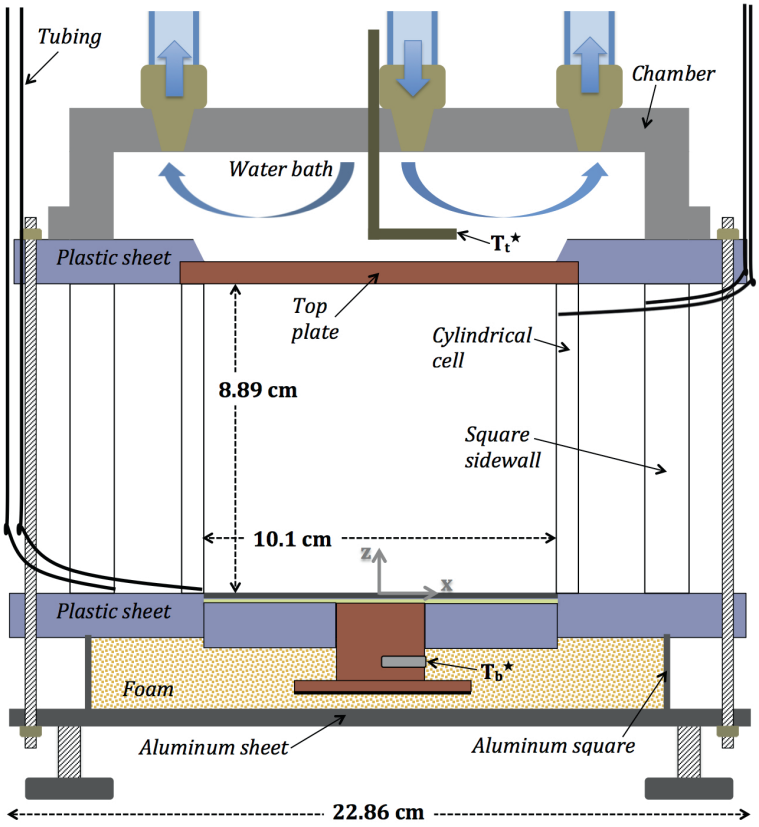

Figure 3.2: Sketch of the cross section of apparatus 2. The cylindrical cell was contained inside a square sidewall. Both cell wall and sidewall were transparent and contained liquid. The bottom plate was interchangeable, allowing for the visualization of bubble formation at wafers with different cavity separations.

opposite sides. Plastic tubes passed through each hole, and at their far ends (outside the apparatus) they could be connected to reservoir bottles. At the other end, two of the plastic tubings (one at the top and one at the bottom) ended flush at the inner side of the square sidewall and the other two were connected to the inner (cylindrical) sidewall through two holes (top and bottom and at diametrically opposed locations). Having two connectors (inlet and outlet) for both cell and sidewall enabled us to independently fill the two chambers with liquid.

3.3.4 Experimental procedure

The cell-filling procedure described in section 2.3.6 for apparatus 1 was used also for apparatus 2. It consisted of heating the bottom plate to a temperature larger than the boiling temperature of the liquid by setting $T_b^\star = 45°\mathrm{C}$ while the top plate was kept at $T_t^\star = 15°\mathrm{C}$. The reservoir bottle connected to the cell bottom and containing the

liquid was then placed at a level above that of the top plate and the cell started filling. The superheated bottom plate assured that vapor would be trapped in the cavities, turning them into active nucleation sites. At the cold top plate most of the vapor condensed, preventing the loss of a large amount of fluid. Once the cell was filled, the 1.16 m tall liquid column in the capillaries and reservoirs exerted a hydrostatic pressure of $P = 117.6 \pm 0.4$ kPa on the bottom plate.

In apparatus 2 the space between the cylindrical cell and the square sidewall was also filled with liquid. Once full, the same hydrostatic pressure was exerted on the bottom plastic sheet. The space between the cell and the sidewall, filled with liquid, helped to thermally isolate the flow inside the cell from temperature variations in the room.

The filling procedure was successful in apparatus 2 for the $l = 0.60$ mm wafer, as the great majority of sites remained active once the cell was full. However, the same procedure led to the activation of only a few tens of sites (out of $N = 1570$) randomly located on the etched area of the $l = 1.0$ mm wafer. In this case, when the cell filling started, all sites were active; but as the liquid level rose, more and more sites deactivated even after increasing $T_b^\star$ to 47°C. This differs from apparatus 1, where this filling procedure was successful also for $l = 1.0$ mm. It is apparent that the vapor trapping in the cavities is a subtle procedure the success of which can be influenced by uncontrolled small details. In section 2.4.1 it was found that the deactivation of nucleating cavities (in apparatus 1) was more susceptible the larger the cavity spacing l was, and that the filling procedure had little success for wafer with $l = 2.0$ mm. In apparatus 2 a similar but more dramatic tendency was observed, considering the different nucleation behavior between wafers with $l = 1.0$ and 0.60 mm. There were a few differences between both apparatuses that could have had an effect on the nucleation process. First, the cell diameter was larger in apparatus 2 implying a larger ratio between cooling and heating areas as compared to the cell in apparatus 1, as well as a larger liquid volume. Second, in apparatus 2 the plastic ring of the assembled bottom plate was in contact with the plastic plate which embedded it, possibly creating a larger heat flux in the horizontal direction as opposed to the situation in apparatus 1, where the bottom plate was in contact with another plastic part through a smaller surface. Third, some cavities etched in the $l = 1.0$ mm wafer could have gotten contaminated, thus reducing the cavity diameter which in turn affected the nucleation conditions. We considered the remaining active sites on the $l = 1.0$ mm wafer in apparatus 2 as non-interacting sites since the majority of their six closest neighboring cavities were inactive.

All measurements were made at a constant temperature difference $T_b^\star - T_t^\star = 20$ K. A run with actively nucleating sites will be referred to as 2-phase flow, while one with none of the sites nucleating will be called 1-phase flow.

For the heat-flux measurements in apparatus 1 a sequence of measurements started with 2-phase flow and typically $T_b^\star = 45.00$°C, $T_t^\star = 25.00$°C. Once a statistically stationary flow was reached (typically after half a day for 1-phase flow and about a day for 2-phase flow), the time-averaged heat current Q was determined (typically over about 3 to 4 hours). Also during this period a high-speed movie was taken from the top, focusing on the nucleation of bubbles at the bottom plate. Then both $T_b^\star$ and $T_t^\star$ were lowered (typically in steps of 1 K), Q was acquired, and a new movie was

recorded. The process continued until none of the sites remained active and the system had entered the 1-phase flow state. Thereafter $T_b^\star$ and $T_t^\star$ were increased (typically in steps of 2 or 3 K) and no sites reactivated; we measured Q of the superheated 1-phase flow.

The liquid in the cell was not fully degassed and thus the saturation temperature was reduced (this effect was reported also in Refs. [15; 16]). If the liquid had been fully degassed, the saturation temperature would have been $T_\phi = 38.5°\mathrm{C}$ at the prevailing pressure. From seven sets of experiments (each set consisted of 1- and 2-phase flow measurements) in apparatus 1 (see section 2.4.2), the onset temperature of boiling was estimated to be $T_{on} = 30.3 \pm 1.1°\mathrm{C}$. Based on T_{on} and assuming no temperature dependence of Henry's Law constant, the dissolved air concentration in the liquid was estimated to be approximately 23% by volume.

We focused on 1- and 2-phase flow at $T_b^\star = 45°\mathrm{C}$ and $T_t^\star = 25°\mathrm{C}$ for flow visualization in apparatus 2. The power P_Ω provided by the heater to maintain the set temperature $T_b^\star = 45°\mathrm{C}$ was 4% larger than measured in apparatus 1 (with the same wafer) for 2-phase flow, and about 3% for the case of 1-phase flow.

The temperatures T_t and T_b at the interface with the liquid of the top and the bottom plate were obtained by applying a correction for the temperature drop in the plate to the measured $T_b^\star$ and $T_t^\star$ (for details of the calculation see section 2.3.3). Typically $T_b^\star - T_b \simeq 4$ K for measurements done in apparatus 1. Note that the thermal forcing applied to the flow, expressed by Ra, was proportional to the temperature difference $\Delta T = T_b - T_t$, see eq. 3.1. Given that the differences in P_Ω in both apparatuses were relatively small, we estimated T_b for measurements done in apparatus 2 and assumed $T_t^\star = T_t$, regarding the large thermal conductivity of copper.

3.3.5 Imaging procedures

We used a high-speed camera (Photron Fastcam Mini UX100) with either one of two lenses (Micro Nikor 105 mm, f/2.8 and AF Nikkor 50 mm, f/1.4) to obtain videos of the phenomenon of interest. Two methods of visualization were employed. One of them consisted of direct illumination and recording the scattered light with the camera. This method was well suited for the visualization of bubbles but did not reveal more subtle optical phenomena associated with the the plumes and the LSC. The other was the shadowgraph method described in detail by Ref. [101]. It produces an image of the two-dimensional Laplacian of the refractive index (proportional to that of the temperature) in a plane orthogonal to the light beam, averaged over the cell width in the direction of the beam. It provided excellent visualization of the plumes and any temperature variations associated with a prevailing LSC, albeit summed over the width of the sample.

Direct illumination method

Three desktop lamps (using 13 W, 800 lumens bulbs each) were used simultaneously as the light source. In apparatus 1 only this method was used, with the camera looking and the lamps shining into the sample from above through the glass and sapphire windows as shown schematically in figure 3.1. The lamps remained on throughout all

measurements, even for the 1-phase flow where no visualization was needed, in order to not alter their small but not negligible heat input. The camera was focussed on the area of the bottom-plate wafer where the bubbles were nucleated. Typical examples of the resulting images are shown in figure 3.4a and 3.4b below. A typical video obtained by this method was provided in the supplementary material of chapter 2.

When visualizing from the side in apparatus 2, three sets of visualizations were made. In two of them, the light entered the apparatus from the side on which the camera was located and the camera recorded the back-scattered light. We shall refer to this as front illumination. The two sets differed only in the distance of the camera and lights from the apparatus, and thus in the size of the field that was recorded. They were used primarily for closeup studies of bubble nucleation and growth, as illustrated below in figure 3.5a.

For closeup movies of the nucleation process, the camera was tilted by about 5 degrees relative to horizontal in order to better capture the nucleation process. The effect of the tilt on the vertical size of the bubble was smaller than one pixel and smaller than other uncertainties. We focused on the front row of bubbles closest to the camera; nucleating sites further back were not visible as the front row blocked the view. At high enough bottom-plate temperatures ($T_b \gtrsim 38°\mathrm{C}$) qualitative observation showed that the nucleating sites at the edge of the heated area behaved in the same way as other active sites. For $T_b < 38°\mathrm{C}$ bubbles nucleating at the edge of A_h remained attached to the bottom surface for much longer times than bubbles nucleated farther away from the edge, restricting the study of the bubble-detachment process.

In the third set illumination was from the side opposite to where the camera was located, and we shall refer to it as back illumination. In that case, the light first passed through a translucent screen which gave a more diffused, uniform light field. The beam was directed toward the area of interest within the sample, and little if any of it entered the camera directly. This method worked well for the visualization of rising bubbles over a large part of the sample and yielded images such as that in figure 3.5b and in the video movie_fig5b.avi in the supplementary material (or upon request).

Shadowgraph method

For shadowgraph visualization we used a procedure described by Ref. [101]. A 5 mW Helium-Neon laser (Melles Griot, 633 nm) illuminated the flow. The beam first passed through a rotating sanded glass disk in order to destroy its coherence and prevent interference patterns due to light scattered from imperfections in the optics such as dust particles. It then passed through a beam expander (see figure 3.3). The expanded beam illuminated the entire cylindrical cell. A translucent screen was placed on the opposite side of the apparatus and the camera was focused on the screen from behind. The setup was tilted by less than 1° in such way that the LSC plane had a preferred orientation parallel to the visualization plane. The imaging area covered the cell from bottom to top. The vertical center line of the image was aligned with the center of the bottom plate. We visualized 1- and 2-phase flow by taking images at a rate of 50 fps. Typical processed shadowgraph image (see section 3.3.6) are shown below in figures 3.6a and 3.6b.

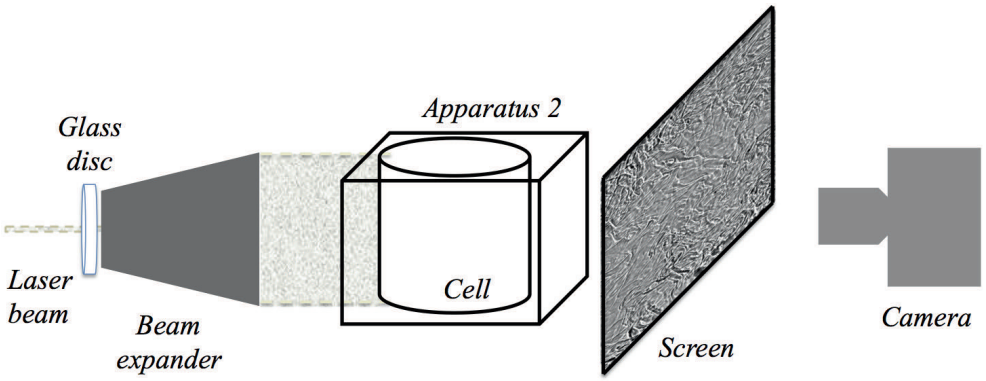

Figure 3.3: Sketch of the shadowgraph technique used with apparatus 2 for side visualization.

3.3.6 Image analysis

Shadowgraph imaging

For all shadowgraph images the intensity of each pixel on every frame was divided by the intensity of the corresponding pixel from a background image. The background image was obtained by averaging the intensity of typically 1500 unprocessed frames. The ratio was re-scaled to represent the appropriate grey levels.

Nucleating bubbles - top visualization (apparatus 1)

Sections of two images showing nucleating vapor bubbles on wafers with $l = 0.60$ mm and $l = 1.0$ mm obtained in apparatus 1 are shown in figure 3.4. They are examples of images analyzed to obtain the time series of the horizontal chord length d of the bubbles. From these time series we detected departure events, i.e. the time when a growing bubble reached a maximum size and detached from the nucleation site.

Detached bubbles were dragged horizontally by the LSC as they rose. They were out of focus and caused blurry bright spots. They blocked the view of attached growing bubbles below them as seen in the bottom left corner of figure 3.4a, where the contours of two growing bubbles can not be identified very well.

We analyzed high-speed image sequences for several T_b for $l = 2.0, 1.0$ and 0.60 mm. The various steps involved are described in appendix 3.B. For wafers with $l = 1.0$ and 0.60 mm and for most T_b values we analyzed more than 2500 departing bubbles. In the case of $l = 2.0$ mm, very few sites were active, and in addition the rate of nucleation of each active site decreased with decreasing superheat. Therefore, for $T_b - T_{on} = 11.85$ K, 9.95 K and 7.98 K, we were able to consider only 1637, 413 and 140 departing events respectively.

Images to binary form were used to count the number of active sites N_a for each T_b and l value. As T_b was reduced, N_a decreased. For the smaller superheats some sites behaved differently: they nucleated very small bubbles at a very high rate whereas other sites nucleated larger bubbles at a lower rate. For low T_b some sites nucleated

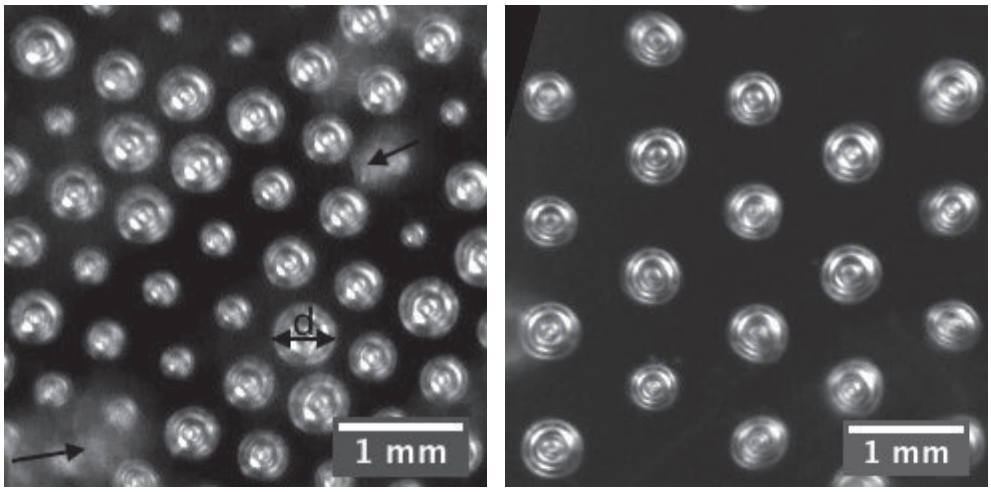

(a) (b)

Figure 3.4: Bubbles, most of them attached to the wafer, viewed from the top in apparatus 1. (a): $l = 0.60$ mm. (b): $l = 1.0$ mm. The bright round shapes in focus are the attached bubbles; their diameters were defined as the horizontal chord lengths d as indicated in (a). The cloud-like bright spots in (a) (see arrows) are bubbles that had departed from the surface and thus were out of focus. Departed bubbles blocked the view of the growing bubbles underneath.

small and large bubbles intermittently. We considered all sites for the total count of N_a, regardless of whether they nucleated larger or smaller bubbles or both.

Nucleating bubbles - side visualization (apparatus 2)

Images of vapor bubbles right before departure from the $l = 0.60$ mm wafer were selected from high-speed movies recorded in runs for $T_b - T_{on} = 9.8$, 8.8, 7.8 K using the front-illumination method (see section 3.3.5). As will be seen below in section 3.4.2, the bubble sizes and shapes within our resolution did not depend on $T_b - T_{on}$. We were able to select 70 images from the three runs with contours at time of departure that were discernible from the bubble cap down to 1/3 of the vertical bubble length d_z above the wafer or lower. We extracted d_z and the horizontal widths d_x and calculated the bubble aspect ratios $\Gamma_b = d_x/d_z$. In figure 3.5a d_x and d_z are indicated for a bubble just before departure.

The left half-contour for the bubble in the center of figure 3.5a is shown as a dotted green line, together with a vertical solid line along the rotation axis of that bubble. Each half-contour with a clear shape was considered as a surface of revolution. The results of both half-contours of a given bubble were averaged and used to calculate the bubble volume V at departure (for details see appendix 3.A).

For $l = 0.60$ mm, 31 of the 70 bubbles showed a clear contour all the way down to the attachment at the wafer at the time of departure. For those cases the contact

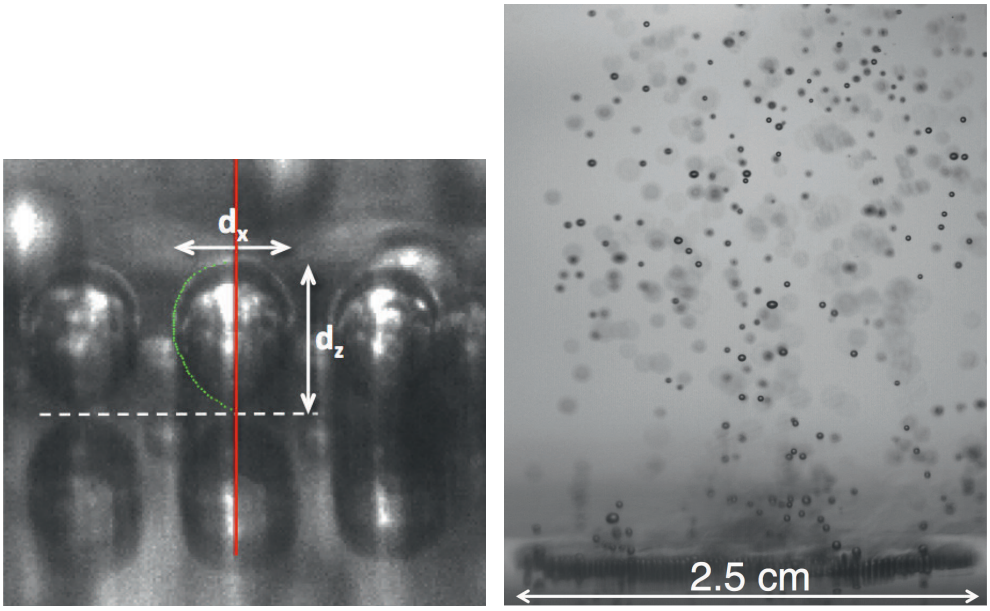

(a) (b)

Figure 3.5: Bubbles for $l = 0.60$ mm and $T_b = 40.1°$C. (a): close-up view of three bubbles obtained by the front-illumination method. The horizontal dashed line represents the liquid-wafer interface. The objects below it are the reflections of the bubbles in the wafer surface. The vertical and horizontal bubble lengths d_z and d_x are indicated. The contact angles between the bubbles and the wafer at departure were estimated from this and similar images. (b): a snapshot of 2-phase flow obtained by the back-illumination method showing a region above the wafer that was 3.2 cm high and 2.5 cm wide. A time sequence of similar images (see the video movie_fig5b.avi in the supplementary material) was used to estimate the velocity and volume of several bubbles from their departure time until they condensed or were out of view.

angle between the bubble contour and the wafer surface could be measured and was found to be $\alpha \simeq 40 \pm 5°$.

For $l = 1.0$ mm only a few sites, randomly distributed over A_h, were active. For $T_b - T_{on} = 10.6$ K we were able to use a total of 33 bubbles to obtain d_x, d_z and Γ_b. We found 19 bubbles that were sufficiently clearly visible at departure to obtain V. For those, the contact angle was estimated as well and found to be $\alpha \simeq 45 \pm 5°$, equal to the result for $l = 0.60$ mm within the uncertainties.

Bubbles rising from the wafer through the turbulent bulk

Vapor-bubbles departing the surface were identified and each one was followed along its rising-path until due to condensation it became too small (given the optical resolution) or until it reached the top plate. We tracked their horizontal and vertical

location (x, z) in a sequence of frames (a typical image is shown in figure 3.8d taken with front illumination) or equivalently, in a time sequence. Their horizontal and vertical velocity components U_x and U_z, respectively, were obtained as a function of time t or as a function of the vertical location z at a given time t_i using finite differences:

$$U_x(t_i) = U_x(z(t_i)) = \frac{x(t_i + \Delta t_i/2) - x(t_i - \Delta t_i/2)}{\Delta t_i} \ . \tag{3.7}$$

where $\Delta t_i = t_{i+1} - t_i$ was the time difference between consecutive frames i and $i+1$ with $i \in \mathbb{N}$. $U_z(t_i)$ and $U_z(z(t_i))$ were similarly defined. The origins $t = 0$ and $z/L = 0$ were taken as the time and location of a bubble immediately after detaching from the surface. Therefore $z/L = 0$ had an uncertainty about equal to the original vertical size of a bubble. Because the whole cell (from the bottom to the top plate) was captured in the images, the spatial resolution was such that the bubbles were nearly point-like objects, and thus the uncertainty in their spatial location was about the size of the bubble itself.

Departed bubbles close to the bottom plate

In order to obtain the time evolution of the velocity and diameter of a bubble right after it detached, we focused on the nucleating sites closest to the camera where the bubbles could be seen at the departure time. For $T_b - T_{on} \simeq 10$ K we recorded the range from $z/L = 0$ and $z/L \simeq 0.36$. The 2.54 cm diameter of the nucleating area (see figure 3.5b taken with back illumination) was used to calibrate the distance between pixels, which was found to be 0.025 ± 0.05 mm. Only bubbles that did not merge with other bubbles were used. They nucleated at different locations on the periphery of the etched area and thus were representative of the entire etched surface. The bubble-center location was tracked in time; the uncertainty associated with the bubble location was less than ± 0.1 mm. Both vertical and horizontal velocity components were calculated, as indicated by Eq. 3.7.

Bubbles that did not merge with other rising bubbles were (within our resolution) spherical at all times except for some bubbles that were ellipsoidal only briefly after departure. The eccentricity (major axis divided by minor axis assuming azimuthal invariance) of the ellipsoidal bubbles was typically smaller than 1.2. We fitted either a circle or an ellipsoid to each bubble and obtained the bubble diameters $2R_b$ along their rising path. In the case of elliptic shapes, we used the *equivalent* diameter, i.e. the diameter of a spherical bubble of the same volume.

3.4 Results

3.4.1 Flow visualization

Shadowgraph

Figures 3.6a and 3.6b show shadowgraph images of 2-phase and 1-phase flow respectively. They are for $T_b - T_{on} \simeq 10$ K, corresponding to $Ra \simeq 1.9 \times 10^{10}$. Corresponding movies can be found in the supplementary material (or upon request) as

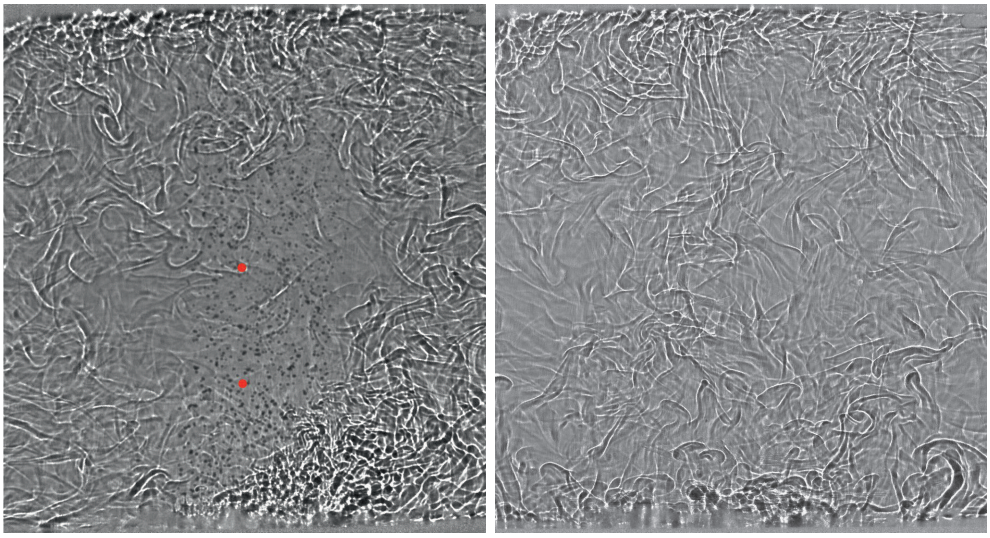

(a) (b)

Figure 3.6: Shadowgraph images of turbulent Rayleigh-Bénard flow for $T_b - T_{on} \simeq 10$ K and $Ra \simeq 1.9 \times 10^{10}$. The bottom and top plates can be seen at the very bottom and top of the images. The cell was very slightly tilted (the left side was lower than right one). (a): 2-phase flow. Hot thermal plumes rise on the right and are diminished as they travel toward the top plate. Cold plumes generated at the top plate move laterally to the left, and travel towards the bottom plate along the left side. Vapor bubbles (dark small spots) that nucleated at the central area of the bottom plate detached and rose. The vertical location of thermistors inserted into the flow is indicated by slightly larger red circles. (b): 1-phase flow. Hot plumes travelled mostly upwards and cold ones downwards without establishing a well-defined circulatory motion.

movie_1phase.mov and movie_2phase.mov. One can see that the thermal plumes and any large-scale flows had different structures and dynamics in the presence and absence of vapor bubbles. In the 2-phase flow (figure 3.6a) hot thermal plumes, mainly produced at the heated area of the bottom plate, drove and were carried by a large-scale circulation. They moved laterally to the right just above the bottom plate and then rose along the side of the cell that was higher due to the deliberately introduced small tilt of the cell. Due to thermal dissipation they became weaker along their path, with only a fraction reaching the top plate. Cold plumes were emitted along the entire top plate. They moved to the left under the influence of the tilt, and then descended along the left sidewall. They too were diminished along their path due to thermal dissipation, and very few reached the bottom plate. Only a small number of plumes were found near the sample center. The structure of the LSC is qualitatively similar to that observed for classical RBC where both plates are heated or cooled over their entire area [103]. There is, however, a quantitative difference in that the hot plumes

generate a very intense rising flow near the cell wall while the cold ones produce a much weaker descending flow just inside the opposite part of the wall.

The rising bubbles (small black solid dots), which nucleated at the central heated area of the bottom plate where the nucleation sites were located, rose with a speed that was much larger than the characteristic LSC speed. Although near the plate they were dragged sideways a short distance by the LSC, over their entire path they moved more nearly in a vertical direction and did not follow the lateral motion of the plumes and the LSC. In this particular run a large number of bubbles reached the top plate. We believe that this was due to a relatively high concentration of dissolved air that was used because it made the bubbles more visible but delayed bubble condensation. Under our standard experimental conditions in both apparatuses, most bubbles fully condensed before they came close to the top plate. The air concentration did not affect the qualitative features of the LSC.

Although heating took place only over the central area A_h, lateral heat flow through the silicon wafer and polycarbonate ring (see figures 3.1 and 3.2) assured that the temperature difference between the top plate and all lateral positions of the bottom plate was large enough to drive turbulent flow. Thus, especially in 1-phase flow, we observed hot plumes emitted over the entire bottom plate, although their abundance was greater over the central area A_h. This can be seen in figure 3.6b and the corresponding video movie_1phase.mov in the supplementary material (or upon request). In our experiment, where heating was localized over the central area A_h, 1-phase flow did not produce a well-defined LSC as can also be seen in the figure and the movie. This finding contrasts with the well known single-roll structure of the LSC for classical $\Gamma \simeq 1$ RBC where the heat input is uniformly distributed over the bottom plate (see, for instance, Refs. [57; 104]).

Interestingly, for 2-phase flow and a superheat of about six Kelvin or more a well defined single-roll LSC was found (see figure 3.6a and the movie movie_2phase.mov), similar to that of classical RBC. The transition from disordered flow to a single-roll LSC in the 2-phase case provides an explanation for relatively sharp changes in some other quantities reported in chapter 2. In section 2.4.3 it was found that the skewness S of the local temperature probability distribution measured at the two locations $z/L = 0.28$ and $z/L = 0.50$ along the vertical axis of the cell was modified by vapor bubbles. The skewness was positive for 1-phase flow, being slightly larger closer to the bottom plate. For superheat values larger than about 6 K S was reduced in 2-phase flow relative to its single-phase value, with a larger reduction closer to the plate. For the largest superheat values S became negative. Shadowgraph visualization provided insight into these results. The location of the thermistors used in chapter 2 to measure local temperature time series is indicated in figure 3.6a (red dots). The shadowgraph movie for 1-phase flow shows that the number of plumes passing by the thermistor at $z/L = 0.28$ was larger than that passing $z/L = 0.50$. This explains the larger value of S closer to the bottom plate. The shadowgraph movie for 2-phase flow explains why S was reduced in the presence of bubbles, where an LSC swept the hot plumes sideways close to the bottom plate and reduced the number of plumes rising vertically across the cell center where the thermistors were located. In 2-phase flow the probability of hot plumes passing by the thermistor at $z/L = 0.28$ was larger than it was at $z/L = 0.50$. If only hot plumes would determine S in 2-phase flow, one would

expect a larger (positive) S closer to the bottom plate than at mid-height, opposite to the results of section 2.4.3. This supports the conclusion, based on the argument of Ref. [71], that bubbles homogenized the temperature field in the bulk, especially close to the bottom plate where the bubbles are bigger (see next subsection) and thus had a larger heat capacity.

Size and velocity of bubbles after departure

In figure 3.7a the temporal evolution of the bubble diameter $2R_b$ of 15 non-merging bubbles is shown. They all present similar behavior. Within about 0.05 s after a bubble detached from the plate, its diameter $2R_b$ typically was reduced by about 1/3 of its initial diameter. The vertical location of bubbles after 0.05 s from departure was between 4 to 5 mm above the surface. However it was within about the first 0.01 seconds after departure and within about 1 mm above the surface that $2R_b$ decreased at the highest rate. We considered the rate of volume change for all 15 bubbles in the first 0.01 seconds after departure and estimated an average condensation rate of about 3 mm^3/s. The bubbles continued to decrease in size (for $t > 0.01$ s) with a nearly linear dependence on time. Two of the tracked bubbles condensed almost completely at about $t = 0.5$ s. The rest of the bubbles continued their rising motion outside of the viewed region. We estimated the condensation rate (for $t \geq 0.1$ s) to be 0.06 ± 0.02 mm^3/s by fitting $\frac{4}{3}\pi R_b^3$ to a linear dependence on time for each bubble and calculating the mean slope and its standard deviation. Note that the initial bubble-diameter values shown in figure 3.7a ($2R_b(t_0) \sim 0.5$ mm) are consistent with the horizontal chord length d_{max} right before departure obtained in section 3.4.2 below.

The initial and posterior condensation rates found in our experiments differed by nearly two orders of magnitude from each other. To grasp this behavior, the different scales of the governing parameters need to be considered. In our geometrically modified RBC flow the temperature drop across the bottom boundary layer (BL) of about $0.7\Delta T$ for 2-phase flow, was found to be three orders of magnitude larger than the temperature difference between $z/L = 0.28$ and $z/L = 0.5$ in the bulk flow (see section 2.3.3). Thus the bubbles rose across a turbulent flow in which Ja varied from $\sim$19 right above the bottom plate to about -1 in the bulk (negative sign due to sub-cooled bulk temperature smaller than T_{on}), i.e. one order of magnitude change in Ja. Theoretically [105] and experimentally [106] Ja has been shown to be a relevant parameter in bubble condensation.

We further analyze the behavior of the collapsing bubbles when taking into consideration the numerical simulations in Refs. [34; 41]. As mentioned in the previous paragraph, the bubbles were faced to the large temperature gradient sustained across the BL; the authors of Ref. [41] simulated numerically the encounter of a vapor bubble with a relatively thin region of liquid subcooled by 3.35 K. The initial bubble diameter and the thickness of the subcooled region were the same. They showed that the bubble lost 80% of its initial volume due to crossing this thin layer. Furthermore, in Ref. [34] it was found that for a condensing bubble, the evolution of R_b and the heat transfer rate crucially depend on the ratio between bubble surface radial velocity $\dot{R}_b = dR_b/dt$ and the stream-wise velocity $|v|$ (relative velocity between fluid and bub-

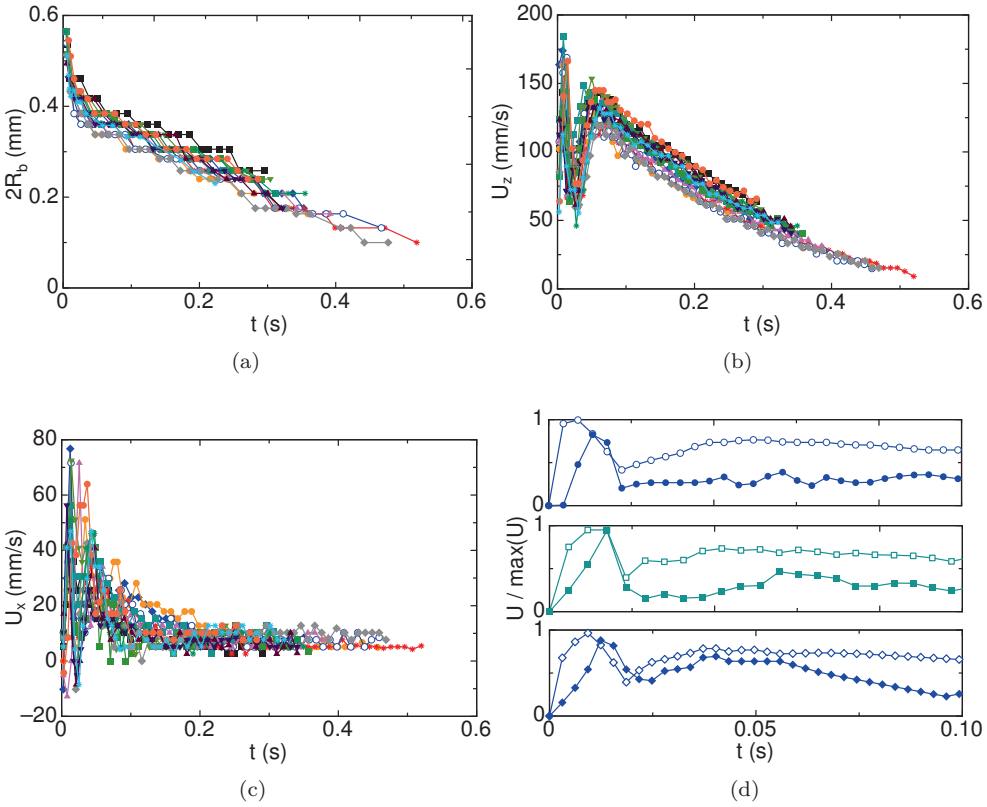

Figure 3.7: Dynamics of tracked bubbles that did not merge with others as they rose between $z/L = 0$ and $z/L \simeq 0.4$. Most of the bubbles were spherical at all times. A few were elliptical briefly right after departure. For elliptical bubbles we used the equivalent diameter instead of the spherical diameter $2R_b$. In (a) the diameter is plotted as a function of time, with $t = 0$ s the time at departure from the bottom plate. In (b) the vertical velocity component U_z of the bubbles represented in (a) is plotted (same color and symbol represent the same bubble) as function of t. In (c) the horizontal velocity component U_x of the bubbles is displayed as a function of t. Each subfigure of (d) corresponds to a single bubble and displays the time evolution of both velocity components normalized by their corresponding maximal values: $U_z/max(U_z)$ (open symbols) and $U_x/max(U_x)$ (solid symbols).

ble). If $\dot{R}_b/|v| > 1$, then the bubble condenses at the same rate as if $|v| = 0$. However, when $\dot{R}_b/|v| < 1$, the thermal boundary layer around the bubble is controlled by the stream velocity and the bubble condenses faster than for a bubble at rest. In our experiments, this ratio $\dot{R}_b/|v|$ was initially about -0.25 and decreased by one order of magnitude within the first 0.05 seconds after departure (equivalent to 4 - 5 mm above the bottom plate), whereas it remained nearly constant for later times. For this estimate $|v|$ was taken equal to the measured speed of the bubbles (see below), under the assumption that the liquid velocity equaled zero.

In view of these results, we suggest that the larger condensation rate found for $t < 0.01$ s in our experiments was a reflection of the large gradients of both Ja and $\dot{R}_b/|v|$. Numerical results indicate that even a thin subcooled region of liquid can have a strong effect on bubble condensation, and this could be similar to the situation that the bubbles in our experiments encountered as they moved across and away from the BL of the bottom plate. Moreover, the posterior condensation rate was that of a bubble moving across fluid with basically constant Ja and $\dot{R}_b/|v|$, in a fluid where large temperature gradients (as found in the BL) were no longer experienced by the bubbles.

Furthermore, throughout the bubbles condensation process we expect the dissolved air in the liquid, which was of approximately 23% in volume, to play a role. In experiments conducted with a larger air concentration we found that the time for bubble collapse or complete condensation was larger, see appendix 3.C. Therefore we expect higher condensation rates the smaller the air concentration is in the liquid. The role of dissolved air in bubble condensation has also been reported in Ref. [83].

In figure 3.7b the vertical velocity component U_z (see eq. 3.7) of all 15 bubbles is plotted as function of time after departure. All curves have a minimum in the time range 0.01 s $< t <$ 0.03 s. At later times ($t >$ 0.03 s) U_z increased again, reached a local maximum and then decreased with basically a linear time dependance as the bubble volume was reduced due to condensation.

In figure 3.7c the corresponding horizontal velocity component U_x is plotted. One sees that in the range 0.01 s $< t <$ 0.03 s the *magnitude* of U_x reached its maximum. Given the angle of tilt of the cell, a positive U_x corresponded to bubble displacement in the same direction as that of the LSC right above the bottom plate. Thus it is reasonable to associate the liquid motion due to the LSC, with a horizontal drag force exerted on the bubbles, which lead to a maximum $|U_x|$ value occurring between 1 and 4 mm above the bottom plate. As the bubbles rose further, they encountered the bulk flow (where the LSC was not as dominant as close to the cell boundaries, see section 3.4.1) and the nearly constant U_x small positive value was associated to the tilt of the cell with respect to the frame of the camera, which was horizontally aligned.

The time evolution between $t = 0$ s and $t = 0.1$ s of both velocity components normalized by the corresponding maximal values $U_z/max(U_z)$ and $U_x/max(U_x)$ of three different bubbles, is shown in figure 3.7d. In this figure we added the initial condition $U_x = U_z = 0$ at $t = 0$ s, which was omitted in figures 3.7a - 3.7c. By comparing the two curves corresponding to each bubble, a relation between U_z and U_x became clear: U_z reached its maximal value ($U_z/max(U_z) = 1$) briefly before U_x did, then U_z started decreasing as U_x increased, U_z reached its minimal value briefly

after U_x reached its maximum. These observations indicate that as the LSC dragged the bubbles horizontally, and as a consequence these slowed down in their rising motion and reached a minimum U_z. After the bubbles crossed the region in which the LSC was influential, U_z increased again due to buoyancy whereas U_x decreased and remained constant for $t \gtrsim 0.2$ s.

A detailed analysis on the forces acting on the rising bubbles with decreasing size and in some cases with changing shape (mostly bubbles were spherical but some bubbles were ellipsoidal briefly after departure) is out of scope in the present work. There are several articles on force balance models, which consider drag, added mass and buoyancy forces and manage to reproduce the dynamics of gas bubbles rising across quiescent or nearly-quiescent liquid observed in experiments. In Ref. [42] the drag of ellipsoidal bubbles was studied, the work in Ref. [37] focused on the added mass force of a rising bubble when it experienced shape oscillations and the one in Ref. [36] which investigated the added mass of an expanding bubble. In view of their models it becomes clear that for the present work, information on the turbulent liquid velocity field around a bubble would be necessary in order to quantify added mass and drag forces and possibly reproduce the observed bubble dynamics. The contribution to the added mass effect due to both the relative acceleration and the pressure gradient in the liquid, as well as the drag force depend on the relative velocity between liquid and bubble, and since we lack such information we can not ponder and quantify the proper force balance for the bubbles studied here rising across a turbulent liquid flow.

Velocity of bubbles across the whole cell

Similar to the analysis done before, we tracked 33 bubbles starting at a few frames after they detached from the surface and until they condensed or reached the top plate, see figure 3.8d. We tracked both bubbles which merged and others that did not. The vertical and horizontal velocity components for each bubble were computed and are plotted as a function of the vertical coordinate z/L (see eq. 3.7) in figures 3.8a and 3.8b, respectively. The large majority of bubbles did not reach the top plate ($z/L = 1$) and there was no general maximal value of z/L where most of the bubbles fully condensed, which was related to the fact that in some cases bubbles merged but also to the random thermal and dynamical history along each bubble rising path. Bubbles merged right after departure most of the times, determining the bubble volume and thus its vertical speed from a very early stage on and until it condensed. In general, bubbles had a horizontal component $U_x > 0$ reflecting the fact that the cell was slightly tilted.

The vertical trajectories of all bubbles had a similar shape. In figure 3.8c each of the U_z trajectories was normalized by their maximal value $max(U_z)$ and plotted as a function of height z normalized by the vertical distance that each bubble travelled before it condensed $max(z)$ or when it reached the top plate $max(z) = L$. The curves collapse on top of each other relatively well for $z/max(z) > 0.3$, showing the correlation between rising velocity and lifetime of a bubble.

Considering the number of frames per second necessary to track the motion of the rising bubbles (typically 500 fps) and comparing it to the frame rate to capture the plume dynamics (between 25 and 50 fps) it becomes clear that the timescales of these

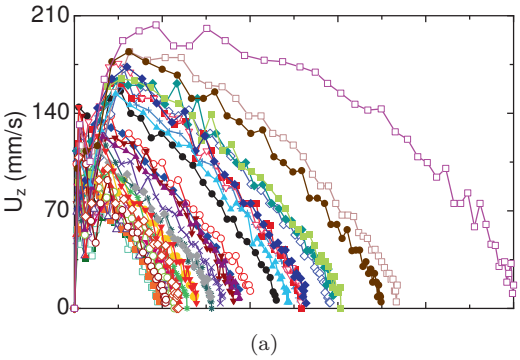

(a)

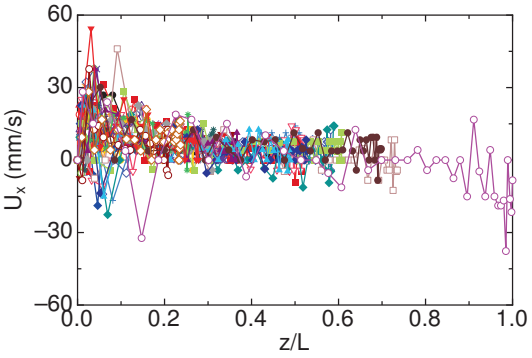

(b)

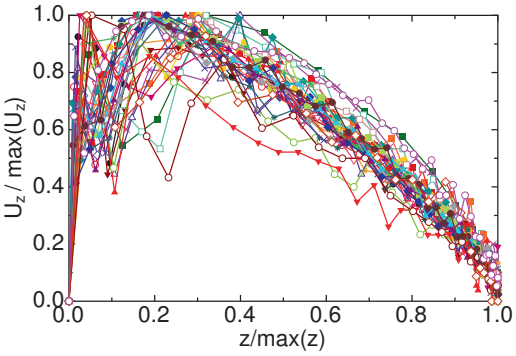

(c)

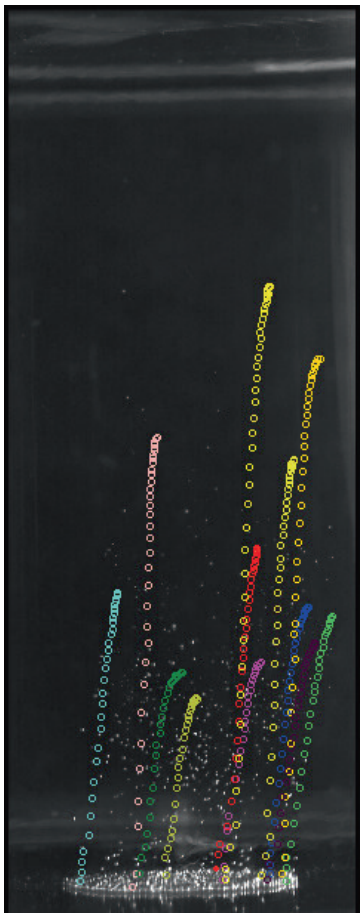

(d)

Figure 3.8: (a) The vertical velocity component U_z and (b) the horizontal velocity component U_x of 33 rising bubbles plotted as a function of the normalized height z/L. (c) U_z normalized by its maximal value along the bubble trajectory $max(U_z)$ as a function of the height z normalized by the height at which the bubble condensed $max(z)$. A bubble is represented in (a), (b) and (c) by the same symbol. (d) Snapshot of the 2-phase flow taken from the side. Wafer with cavity separation of $l = 0.60$ mm. The etched area with nucleating cavities is identified as the bright ellipse on the bottom of the image; superimposed to it are the trajectories (different color each) of bubbles from surface departure and until they condensed.

two heat transport mechanisms were at least one order of magnitude different.

Nucleation close up

The vertical and horizontal sizes of the bubbles, d_z and d_x respectively, detaching from the $l = 0.60$ mm wafer presented no significant superheat dependance in the regime between 7.8 K and 9.8 K. This superheat independence was in accordance with the measurements on bubble horizontal chord length at departure obtained from top visualization over a wider superheat range between ~ 3 K and 10 K for the same cavity separation (see section 3.4.2). Considering the 70 departing bubbles selected for $T_b - T_{on} = 9.8, 8.8$ and 7.8 K we estimated the mean and standard deviation values of the characteristic bubble lengths ($d_x = 45.0 \pm 2.0$ pixels and $d_z = 57.1 \pm 3.5$ pixels) resulting in an aspect ratio $\sigma_d = d_x/d_z = 0.79 \pm 0.03$. For the case with $l = 1.0$ mm and $T_b - T_{on} = 10.6$ K, based on 33 bubbles at departure we similarly found $\sigma_d = d_x/d_z = 0.72 \pm 0.03$.

3.4.2 Visualizations from top

Bubble detachment process

Timeseries of horizontal bubble chord length d for growing bubbles on single nucleation sites etched on the $l = 0.60$ mm wafer at two different superheat values are shown in figures 3.9a and 3.9b. In figure 3.9a with $T_b - T_{on} = 4.69$ K, five departure events or peaks (each followed by a waiting time between departure and the beginning of the next bubble growth) and four full cycles (growth from $d = 0$ to d_{max}) are shown. The inverse of the time difference δt between consecutive peaks is defined as departure frequency $f = 1/\delta t$. All bubbles which grew and departed within the 14 seconds displayed showed similar behavior, reaching about the same diameter value d_{max} right before departing from the surface. The vapor-bubble growth rate shown in figure 3.9b for a superheat $T_b - T_{on} = 8.59$ K is much larger than that for figure 3.9a with $T_b - T_{on} = 4.69$ K: within 3.5 seconds 6 bubbles departed from the surface. Figures 3.9c and 3.9d display the bubble volume estimate $\pi d^3/6$ corresponding to the timeseries of d shown in figures 3.9a and 3.9b, respectively. The volume of a spherical bubble $\pi d^3/6$ with radius $d/2$, was an approximation to the volume of the actual (non-spherical) bubbles. As shown, for both superheat values $\pi d^3/6$ increased about linearly with time.

The linear growth of $\pi d^3/6$ contrasted with existing models on vapor bubble growth [25; 26], which predict that for a spherical bubble, volume $\propto t^{3/2}$. The models are valid in the asymptotic stage of large radius, when growth is controlled by thermal energy inflow and liquid inertia is not a limiting factor. The model assumes growth occurs in stagnant and uniformly superheated liquid, and is only valid for sufficiently large liquid superheats [24]. It has successfully reproduced bubble growth in water and CCl_4 and at moderate and high pressures in ethanol and water [107]. However, in our experiments the growth conditions differ from those assumed in the models; here the temperature field around a growing bubble presented a steep gradient across the thermal BL at the bottom plate. It is not possible to determine with precision the BL thickness, but a lower estimate in 1-phase flow was about 90 μm for $Ra \sim 2 \times 10^{10}$, see

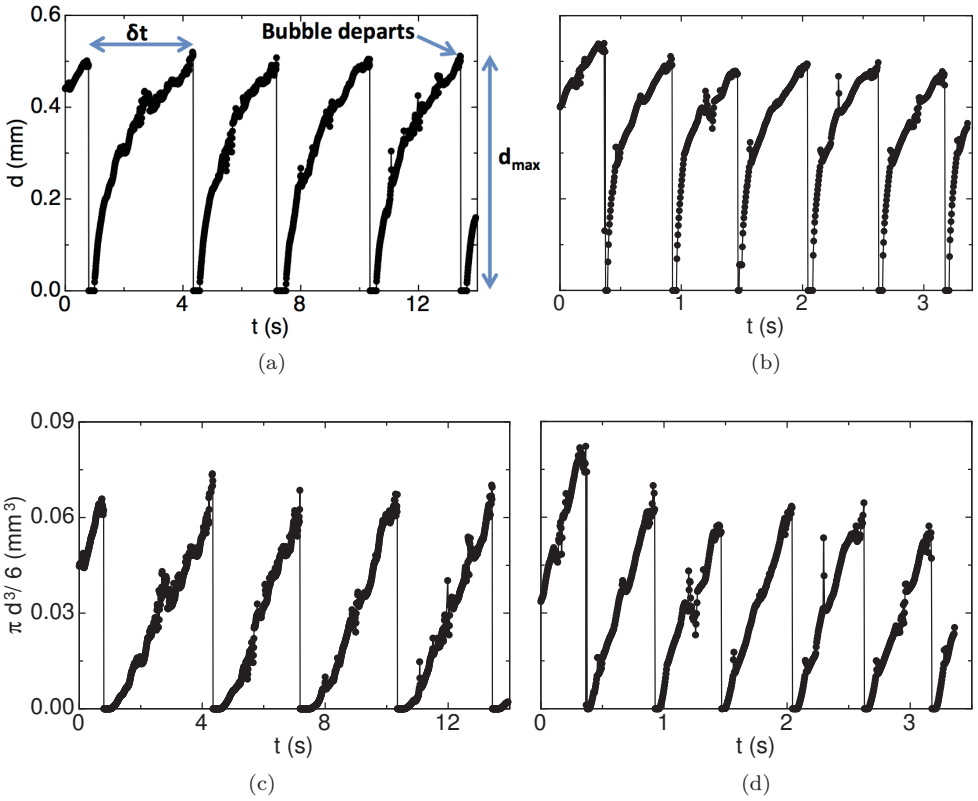

Figure 3.9: Timeseries of growing bubbles obtained from high-speed movies of a single nucleating site etched on the bottom plate ($l = 0.60$ mm wafer) and captured through the top of apparatus 1. Data are shown for two different superheat values: $T_b - T_{on} = 4.69$ K in (a) and (c), and $T_b - T_{on} = 8.59$ K in (b) and (d). Subfigures (a) and (b) present timeseries of bubble chord length d. In (a) the nucleation and growth of 4 vapor-bubbles (complete cycle) at the bottom plate can be appreciated. Right after a bubble departed $d = 0$ mm and after a certain waiting time a new bubble started growing and d increased again until it reached a (maximal) departure horizontal chord length d_{max}. The time difference between consecutive bubble departure events δt is indicated. Subfigures (c) and (d) show $\pi d^3/6$ (volume estimate) of the data displayed in (a) and (c), respectively. The time dependence of $\pi d^3/6$ is approximately linear for both superheat values.

section 2.4.2. Moreover, it is unknown how the growing bubbles modified the thermal BL and its thickness, and how it compared to the size of a growing bubble. Nonetheless we expect a large temperature drop across the BL thickness, that is smaller than the bubble size at departure $d_{max} \simeq 0.5$ mm. Major differences between the model and the situation in our experiments included non-spherical bubbles, bubble interactions with the neighboring ones and the fact that the flow was turbulent. Therefore the bubble growth rate was very different than expected from uniformly superheated conditions in a static flow assumed in the models.

The departure events obtained for all active sites at a given $T_b - T_{on}$ and cavity separation l were considered as an ensemble. For every ensemble we obtained the probability density function (PDF) of the bubble horizontal chord length at departure d_{max}, as well as the PDF of δt. Since d_{max} was positive and observed to be smaller than the cavity separation l for all cases, its PDF was calculated over the range 0 and l. The bin size for the d_{max} PDF equaled the pixel size of the images (0.016 mm). The bin size for the PDF of δt was different for every ensemble as the range between maximal and minimal values of δt varied for each l and superheat value.

In figure 3.10a the probability density functions of d_{max} for $l = 0.60$ mm at different superheat values are shown; each of them was fitted by a Gaussian function. In figure 3.10b the PDF of δt at different superheat values fitted by Gaussian functions are shown. Similarly, Gaussian distributions were fitted to the PDF of both d_{max} and δt obtained for wafers with $l = 1.0$ and 2.0 mm.

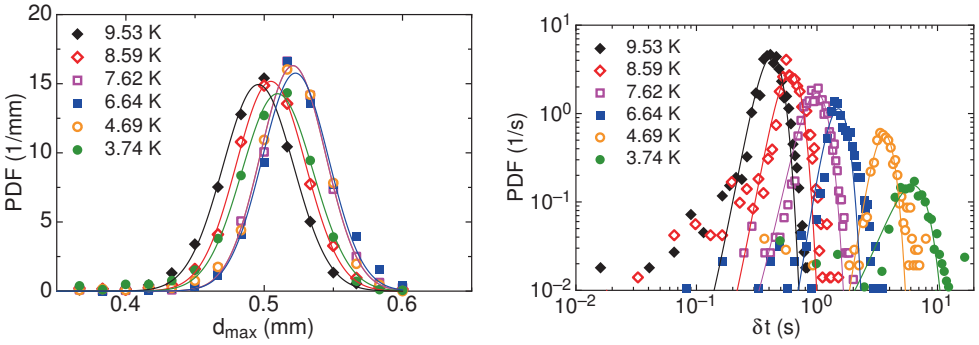

(a) (b)

Figure 3.10: In (a) probability density functions (PDF) of bubble horizontal chord length at departure d_{max} and in (b) PDF of the time difference between consecutive bubble departure events δt for various bottom plate superheat values $T_b - T_{on}$ (see labels) and $l = 0.60$ mm wafer. Each PDF was fitted by a gaussian distribution.

At the lowest superheat value presented here $T_b - T_{on} = 3.74$ K, the PDF of d_{max} and δt for the $l = 0.60$ mm wafer showed two peaks, reflecting the fact that some active nucleation sites behaved differently than others: some sites nucleated bubbles at a higher rate which departed with a much smaller size, whereas other sites nucleated bubbles that reached approximately the same d_{max} as observed for larger superheat values, that is $d_{max} \simeq 0.51$ mm. The horizontal chord length of the small departing

bubbles and the uncertainty associated to it were of the same order. For such small bubbles the departure frequency f was so large that the corresponding peak in the PDF of δt was one order of magnitude larger than the peak located at $\delta t \simeq 10$ s (see figure 3.11a), associated to the larger bubbles. In order to include the results from cavities nucleating larger bubbles obtained for $T_b - T_{on} = 3.74$ K, only departure diameters larger than 0.1 mm were considered for figure 3.10a and values for $\delta t > 3$ s for figure 3.10b. A similar behavior was found in the measurements from the $l = 1.0$ mm wafer at $T_b - T_{on} = 4.28$ K; in this case we neglected d_{max} values smaller than 0.25 mm which represented less than 15% of the 3408 departure events considered and fitted a Gaussian distribution to the PDF of $d_{max} > 0.25$ mm.

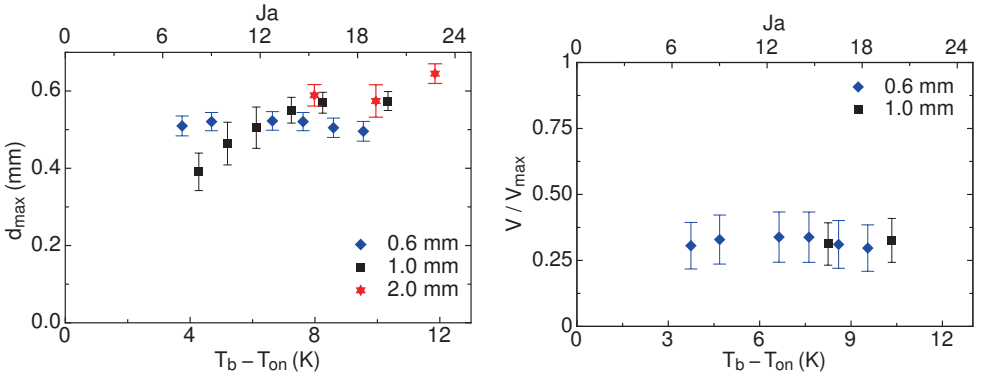

Figure 3.11: In (a) the mean values of the Gaussian fits to the (maximal) bubble chord length at departure d_{max} for all wafers with different cavity separation l are plotted as a function of the bottom plate superheat $T_b - T_{on}$ and the Jakob number Ja. The vertical bars indicate the standard deviation of the distribution. In (b) the ratio between estimated bubble volume V and the maximal bubble volume V_{max} attainable if spherical bubbles would grow in an equilibrium state balancing surface tension and buoyancy forces only, plotted as a function of superheat and Ja. In (a) and (b) l is indicated by the labels.

The mean value V of the bubble volume computed for all selected bubbles with a clear contour at departure was obtained for $l = 0.60$ mm and $l = 1.0$ mm. V was compared with the attainable maximal volume of a bubble growing at a wall under equilibrium conditions (slow growth) V_{max}, when only surface tension and buoyancy forces are considered [27]. If the bubble is spherical then V_{max} is given by

$$\frac{V_{max}}{l_c^3} = \varphi(\alpha) \tag{3.8}$$

where α is the contact angle between the surface and the bubble, and l_c is the capillary length

$$l_c = \sqrt{\frac{\gamma}{g(\rho - \rho_v)}} \tag{3.9}$$

where γ is the surface tension, ρ was evaluated at T_b and ρ_v at the vapor partial pressure. Ref. [27] reported a table for nine α values and the corresponding V_{max}/l_c^3 value. For the working liquid in our experiments l_c ranged between 0.97 and 0.95 mm, as the surface tension decreased with increasing bottom plate temperature. From side visualization we found $\alpha = 40^\circ \pm 5^\circ$ for $l = 0.60$ mm and $\alpha = 45^\circ \pm 5^\circ$ for the wafer with $l = 1.0$ mm, resulting in slightly different values of V_{max} for each case. For the wafer with $l = 1.0$ mm the majority of sites were not active when the departing bubbles were visualized from the side, and the corresponding larger value of α could have been a consequence of that.

In figure 3.11b the ratio between the estimated V and V_{max} is presented as a function of both superheat and Ja, obtained for the wafers with $l = 0.60$ mm and $l = 1.0$ mm. The vertical bars indicate the uncertainty range associated to V. In the entire range $V < V_{max}$, thus the bubbles were subjected to other forces and their shape determined by other factors. The LSC in the flow could have exerted a drag force on the bubbles, causing them to detach once they had reached a certain size. Another determining factor for $V < V_{max}$ could be the heat flux rate. The authors of Ref. [30] developed a model that appropriately predicted V/V_{max} of detaching gas bubbles from a needle, expressed in terms of the gas flow rate through the needle and into the bubble. This process has some resemblance to bubble departure in boiling. For the case in which the growth was dominated by the flow rate rather than by inertia, if the flow rate was below a certain critical value, then the bubbles detached from the needle with a volume V smaller than the volume of a spherical bubble for which buoyancy and surface tension were in equilibrium, i.e. V_{max}. For flow rates below the critical value, V decreased little as the flux decreased. If the flow rate was above the critical value, they found that V increased with an exponent of 6/5 with the flow rate. They reported that the criterion for departure for high flow rates was met when the bubble volume was past V_{max}, which explains the bubble volume being larger than V_{max}. Moreover, for flow rates below the critical value, this condition is met before V_{max} is achieved and the bubble departure is limited by surface tension, which is overcame when $V \approx V_{max}$. Important deviations from this condition ($V \approx V_{max}$) exist because the spherical bubble approximation is not very accurate for small flow rates since inertia, which promotes sphericity, is very small. Therefore the fact that in our experiments $V < V_{max}$ in the entire range could be related to the heat flux rate being below a certain critical value. Additionally, the non-sphericity of the bubbles in our experiments could be due to the small inertia, i.e. the small pressure difference between the inside and the outside of the bubble.

Mean and standard deviation values were computed from the Gaussian distributions. In figure 3.11a the mean departure diameter found for all cavity separations is plotted as a function of both superheat and Ja. The vertical bars indicate the corresponding standard deviation of the distributions. One can see that for $l = 0.60$ mm the bubble departure diameter remained nearly constant at $d_{max} \simeq 0.5$ mm in the entire superheat range. The results for $l = 1.0$ mm show a weak dependance of d_{max} on superheat; d_{max} decreased with decreasing superheat for $T_b - T_{on} < 8$ K. The results for $l = 2.0$ mm are comparable to the ones obtained for $l = 1.0$ mm at $T_b - T_{on} \simeq 10$ and 8 K; at the largest superheat the bubbles detached from the surface with the largest d_{max}.

The mean values of δt are plotted on a log-scale as a function of the bottom plate superheat and Ja in figure 3.12a for all cavity separations. All data points shown except the one for $l = 1.0$ mm at lowest superheat were fitted by a single exponential function: $\delta t = 31.0 exp(-(T_b - T_{on})/C)$ s, where $C = 2.12$ K (dashed line in figure). The mean values of δt decreased with superheat (and Ja) with the same exponential dependence, independent of cavity separation.

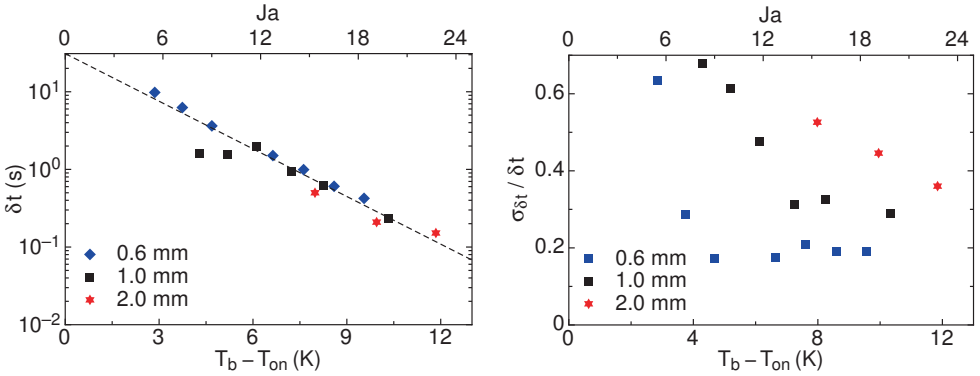

Figure 3.12: In (a) the mean values obtained from the Gaussian fits to the time difference between consecutive bubbles departures δt are plotted as a function of the bottom plate superheat $T_b - T_{on}$ and the Jakob number Ja for different cavity separations l. All data points except for the square at the lowest superheat were fitted by $\delta t = 31.0 exp(-(T_b - T_{on})/C)$ s, where $C = 2.12$ K (dashed line). In (b) the standard deviation values divided by the corresponding mean $\sigma_{\delta t}/\delta t$ are plotted as a function of $T_b - T_{on}$ and Ja. In (a) and (b) l is indicated by the labels.

On one hand, bubble growth rate and departure frequency greatly increased with increasing superheat and Ja, reflecting the larger rate at which heat was supplied to an active nucleation site and to the surrounding superheated liquid. On the other hand, a higher heat flux rate at the bottom plate did not strongly affect the volume at departure, suggesting that the heat flux rate into the bubbles remained below a certain critical value [30] in the studied superheat range. The heat flux rate into a growing bubble depended on several factors, such as thermal boundary layer thickness at the bottom plate and its relative size with respect to the bubble vertical length, bubble thermal boundary layer thickness and the temperature field around it.

The ratio of the standard deviation $\sigma_{\delta t}$ and the corresponding mean value δt of the time between consecutive departures is plotted in figure 3.12b as function of both superheat and Ja. As δt increased for decreasing superheat values, it was also subjected to increasingly larger fluctuations around the mean, thus $\sigma_{\delta t}/\delta t$ reached up to 60% at the lowest superheats. The fluctuations around the mean were the stronger the larger the separation between active sites, that is, nucleating bubbles with closer neighboring active sites departed the surface in a more regular manner in time than bubbles departing from wafers with larger cavity separation. We suggest

that these irregularities originated from deviations from a constant heat supply in time likely caused by transient colder (than average) liquid around a nucleating site. If one considers closer sites facing together transient colder liquid versus an isolated nucleating bubble in the same situation, it is reasonable to think that the impact of a certain volume of colder liquid is the less the larger the number of bubbles per area is, as they can all contribute to the increase of the temperature of that volume of colder liquid. This result supports the view that the larger the cavity separation, the more susceptible were the sites to deactivate at a given superheat (see section 3.3.4).

Bubble latent heat content

The heat per unit time Q_{2ph} for 2-phase flow was enhanced with respect to the one for 1-phase flow Q_{1ph} in the entire superheat (and thus Ja) range studied. The enhancement $Q_{2ph} - Q_{1ph}$ had three different main contributions due to different mechanisms; here we quantify the contribution of the latent heat content of bubbles growing on the heated surface. Figure 3.13 shows on a log-linear scale, $Q_{2ph} - Q_{1ph}$ divided by the corresponding number of active sites N_a, i.e. the heat per unit time enhancement due to a single active site, as function of superheat and Ja (solid symbols) measured for both $l = 0.60$ mm and 1.0 mm wafers. Over the entire superheat range depicted, $(Q_{2ph} - Q_{1ph})/N_a$ was larger for the wafer with a larger cavity separation, and for a given l it remained approximately constant for $T_b - T_{on} \gtrsim 6$ K and slightly declined for decreasing superheat values smaller than about 6 K.

Assuming that the entire heat absorbed by a bubble with volume V was used to generate vapor at the saturation density and pressure (partial pressure of vapor was 86 kPa), we estimated the latent heat H content of a single bubble. Knowing the superheat dependence of bubble departure frequency $1/\delta t$ allowed us to compute the heat per unit time associated to the departing vapor bubbles of a single nucleation site, expressed by

$$Q_{bub} = \frac{HV\rho_v}{\delta t}. \tag{3.10}$$

It is important to note that there was a considerable amount of dissolved air in the liquid (see section 3.3.4) and that the bubble volume at departure was probably a mixture of vapor and air, however the concentration of each inside the bubble is unknown. Therefore Q_{bub} was an upper bound to the actual latent heat absorbed by the growing bubbles from a single site per unit time. The contribution of bubble latent heat to the enhancement of heat per unit time $Q_{bub}N_a/(Q_{2ph} - Q_{1ph})$ is plotted as a function of superheat and Ja (open symbols) in figure 3.13 for both $l = 0.60$ mm and $l = 1.0$ mm. The vertical bars show the uncertainty range by taking into account the uncertainty value of V, as well as $\sigma_{\delta t}$. For both l values, the ratio $Q_{bub}N_a/(Q_{2ph} - Q_{1ph})$ increased with superheat basically due to the exponential decrease of δt with increasing superheat, as V had no significant dependence over the superheat ranges considered here. For $l = 0.60$ mm, at $T_b - T_{on} \simeq 4$ K the contribution $Q_{bub}N_a/(Q_{2ph} - Q_{1ph}) \simeq 0$ and it reached a maximum value of 25% at the largest superheat. The two points obtained for $l = 1.0$ mm were smaller than $Q_{bub}N_a/(Q_{2ph} - Q_{1ph})$ obtained for $l = 0.60$ mm. Considering that d_{max} and V were slightly larger for the $l = 1.0$ mm case (for $T_b - T_{on} \gtrsim 8$ K) and that δt did not vary from one cavity

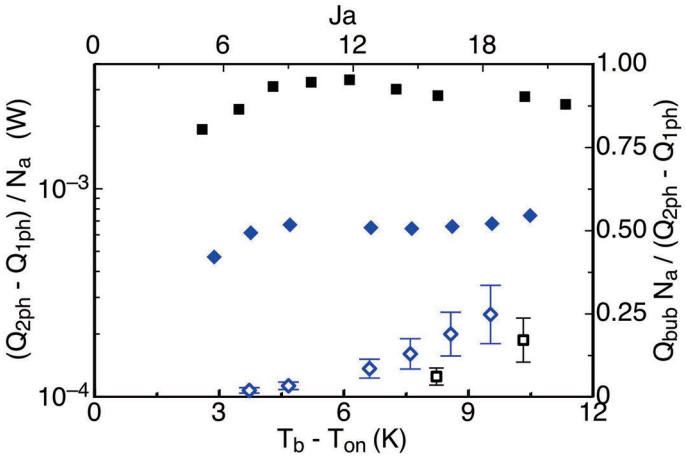

Figure 3.13: Right vertical axis: the heat per unit time difference between 2- and 1-phase flow divided by active site number $(Q_{2ph} - Q_{1ph})/N_a$ (solid symbols) is plotted on a logarithmic scale as a function of the bottom plate superheat $T_b - T_{on}$ and the Jakob number Ja. Left vertical axis: the ratio between the latent heat per unit time divided by the heat per unit time enhancement associated to a single active site $Q_{bub}N_a/(Q_{2ph} - Q_{1ph})$ is plotted (open symbols) as a function of $T_b - T_{on}$ and Ja. The vertical error bars represent the uncertainty range. Symbols: diamonds for $l = 0.60$ mm, squares for $l = 1.0$ mm.

separation to another, then the smaller $Q_{bub}N_a/(Q_{2ph} - Q_{1ph})$ calculated for $l = 1.0$ mm was a consequence of the smaller number of active sites N_a.

The larger the contribution of bubble latent heat was, the smaller became the relative contributions of the other mechanisms (processes next to the wall and enhanced buoyancy). However it does not necessarily follow that these contributions had an absolute decrease. For example if one considers the case with $l = 0.60$ mm, for which V was constant over a wide superheat range; a smaller δt implied a larger effective buoyancy since the number of bubbles rising across the flow augmented. Therefore the absolute contribution due to effective buoyancy to the total heat flux enhancement was indirectly found to increase with superheat, similar as reported by Ref. [70]. Quantifying the effective buoyancy contribution would imply knowing the absolute contribution of the processes next to the wall (micro-convection and transient conduction) as a function of superheat, which is out of scope in this chapter.

3.5 Conclusions

We studied the nucleation and growth of vapor bubbles, as well as their detachment from the bottom plate and their rise dynamics across a Rayleigh-Bénard convective sample with aspect ratio $\Gamma \simeq 1$ and modified geometry (the heated area was smaller than the bottom and top plates). For this purpose, two different setups were used; one enabled flow visualization from the top and the other from the side. The flow

dynamics was visualized by means of the shadowgraph technique and the observations for 1- and 2-phase flow were compared.

For $Ra \simeq 1.9 \times 10^{10}$ we found that in the presence of vapor bubbles the circulatory motion of the large-scale-circulation (LSC) was better defined as compared to the 1-phase flow. Furthermore, the modified geometry of our sample affected the LSC single-roll configuration found in classical (1-phase) Rayleigh-Bénard convection. In the presence of bubbles the thermal plumes mostly rose and descended along the sidewalls, and together with the bubbles heat capacity, which homogenized the thermal field in the bulk flow, reduced the skewness of the locally measured temperature in the bulk, see section 2.4.3. The detached bubbles moved vertically across the bulk flow with a velocity which was at least one order of magnitude larger than the one characteristic of the LSC. Though qualitative, this result shows that vapor bubbles are very efficient heat carriers.

The growth rate of bubble volume had a time dependence close to linear. Right before departure from the surface, bubbles were not spherical; their maximal chord length (of about 1/2 cm) at departure did not present a significant dependence on the bottom plate superheat (between 3 and 12 K) for a cavity separation of 0.60 mm, and only a small dependence for cavity separations of 1.0 mm and 2.0 mm. As the bubbles detached, their volume was significantly smaller than the one predicted from assuming equilibrium of buoyancy and surface tension during bubble growth with spherical shape and neglecting thermal effects [27]. The time difference between consecutive departures exponentially decreased for increasing superheat, independent of cavity separation. The larger the distance between cavities, the more irregular their departure frequency was, exposing the susceptibility of an isolated bubble to an inhomogeneous and time-varying thermal field around it.

Detached bubbles experienced a large volume decrease as they moved across the region closest to the bottom plate, which was associated to large gradients across the thermal boundary layer. The bubbles continued shrinking in the bulk flow at a rate that was about two orders of magnitude smaller than the initial condensation rate. The rising bubbles experienced a strong vertical deceleration at a few millimeters above the bottom plate related to their interaction with the LSC, which exerted a drag force in horizontal direction, increasing their velocity in that direction.

Assuming that the bubbles right before departure consisted of pure vapor, an upper bound to the contribution of latent heat per unit time to the total heat per unit time enhancement was found; the contribution increased with superheat and reached up to 25%. Therefore the relative contribution of the other two main heat transport mechanisms (induced next to the superheated surface by bubble growth and departure, and enhanced flow buoyancy together with latent heat advection by rising bubbles) became smaller as the superheat increased. However, the absolute contribution of the enhanced buoyancy also increased with superheat, at least within the superheat range in which bubble volume did not vary, since the bubble departure frequency exponentially increased with it, leading to a larger amount of rising bubbles per unit time in the flow.

The results found here open several questions that can be answered through further experiments: how does the Reynolds number of 1-phase flow change when vapor-bubble nucleation takes place? How does this change depend on bottom plate super-

heat and thus on the Jakob number? Does the LSC in 2-phase flow present similar features like cessations, sloshing and twisting [57] as in classical 1-phase Rayleigh-Bénard flow?

Appendix

3.A Bubble volume

Right before departure from the bottom plate, the bubbles were not spherical. Their volume was obtained by considering the contour of both halves of it as a surface of revolution, as described in section 3.3.6, which led at first hand, to a volume expressed in pixels^3, to which we refer as V_{bub}. Here the methods used to calibrate the latter in order to obtain the volume V in physical units are described.

Not all recordings taken from the side of the growing and departing bubbles presented an object of known size that could be used to calibrate the image. Some recordings captured contiguous nucleation sites and the known cavity separation l served as calibration object. In other recordings, where contiguous nucleating cavities were not on the same imaging plane, using l for calibration did not provide a precise method. Furthermore, the active nucleation sites on the $l = 1.0$ mm wafer were so few, that they had no contiguous active cavities and l could not be used for calibration. Therefore a different method was used. First, for the (non-spherical) bubbles for which V_{bub} was obtained, we also calculated the volume of the sphere with radius equal to half of the bubble vertical size (in pixels) $d_x/2$ expressed by $V_{sp} = \frac{4}{3}\pi(d_x/2)^3$. We then computed the ratio between the volume of the non-spherical shape and the volume of the spherical one V_{bub}/V_{sp}. For each of the 31 bubbles considered for $l = 0.60$ mm and for the 19 bubbles measured for $l = 1.0$ mm, we computed the ratio of the volumes and on average obtained $V_{bub}/V_{sp} = 1.18 \pm 0.05$ and 1.19 ± 0.06, respectively.

Note that for $l = 0.60$ mm, d_{max} (obtained through visualization from the top, see section 3.4.2) showed no significant dependence on $T_b - T_{on}$ over the range from ~ 3 K to 10 K; the independency of bubble size with superheat was confirmed over a smaller superheat range between 7.8 K and 9.8 K by the bubble vertical and horizontal sizes d_z and d_x (obtained through lateral visualization, see section 3.4.1), respectively. Therefore we assumed that V_{bub}/V_{sp} was constant for 3 K $< T_b - T_{on} <$ 10 K and $l = 0.60$ mm. For the case with $l = 1.0$ mm, V_{bub}/V_{sp} was only obtained at $T_b - T_{on} =$ 10.6 K. Because for $T_b - T_{on} < 8$ K d_{max} decreased as superheat became smaller and remained constant for $T_b - T_{on} > 8$ K, $V_{bub}/V_{sp} = 1.19 \pm 0.06$ was not extrapolated to be valid for superheat values smaller than 8 K. Therefore bubble volume for $l = 1.0$ mm was only calculated for $T_b - T_{on} > 8$ K.

Then, we used the mean value of the bubble horizontal chord length right before departure d_{max} (expressed in millimeters) to calculate the volume of a sphere with radius $d_{max}/2$. Finally, from the equation

$$V/(4/3\pi(d_{max}/2)^3) = V_{bub}/V_{sp} \tag{3.11}$$

we calculated the mean volume V of the departing bubbles expressed in mm^3.

3.B Bubble detection algorithm

Step 1: locate active sites. We obtained the average intensity of the whole set of images to be analyzed. After imposing an intensity threshold on the average intensity image, active sites were identified with regions that appeared bright (due to all bubbles that nucleated there) and were surrounded by a dark background. The center of mass of each bright region was identified as the cavity location of the corresponding active site. About 150 active cavities were analyzed for each temperature.

Step 2: calibrate images. We took average intensity images acquired for very low T_b values, for which d and δt were small, to find the distance (pixel number) between neighboring active cavities and used the known l to calibrate all images acquired under the same circumstances.

Step 3: analyze frames. Every frame of a given set was imposed the same intensity threshold value; bubbles appeared then bright and the background dark. Each identified bubble with its center of mass close to a cavity location (within certain threshold) was identified as a bubble growing at that specific cavity. A roundness threshold was applied to each identified bubble. The diameter of every bubble on one frame that fulfilled these requirements was saved in an array identified with a specific cavity. The bubble horizontal chord length was defined as twice the maximal distance between cavity location (obtained in step 1) and the periphery of the detected bubble. If for a given frame there was no bubble identified to a cavity, the diameter value was defined as zero. The outcome of step 3 was the timeseries of growing bubbles, which eventually departed from the surface, for each active cavity, as is shown in figure 3.B.1a (circles). These timeseries often needed further processing due to several reasons: as explained earlier, passing bubbles blocked the view often leading to a non-representative zero diameter values in the timeseries or, if all imposed requirements were fulfilled by a passing bubble, then spurious chord length values appeared in the timeseries.

Step 4: removing non-representative zero diameter values. A moving average was applied to the original timeseries (outcome of step 3) to obtain a smoother timeseries as shown in figure 3.B.1a. The moving average timeseries had positive diameter values instead of non-representative zeros. Close to bubble departure the moving average timeseries was smaller than the original timeseries. This was due to the definition of a moving average and the fact that at times near departure large values of d were averaged with $d = 0$ due to the departure. The bubble size at departure was underestimated by the moving average timeseries. Because the moving average corrected some aspects of the original timeseries but at the same time underestimated bubble size at departure, the outcome of step 4 was a combination of both original and moving average timeseries. If for a given frame or, equivalently a given time, the original timeseries value was smaller than the moving average timeseries value, then at that frame the value in the original timeseries was replaced by the moving average value, resulting in a timeseries as shown in figure 3.B.1b. After applying step 4 the timeseries became more suitable for further analysis.

Step 5: detection of departing bubbles. For each active cavity a timeseries was

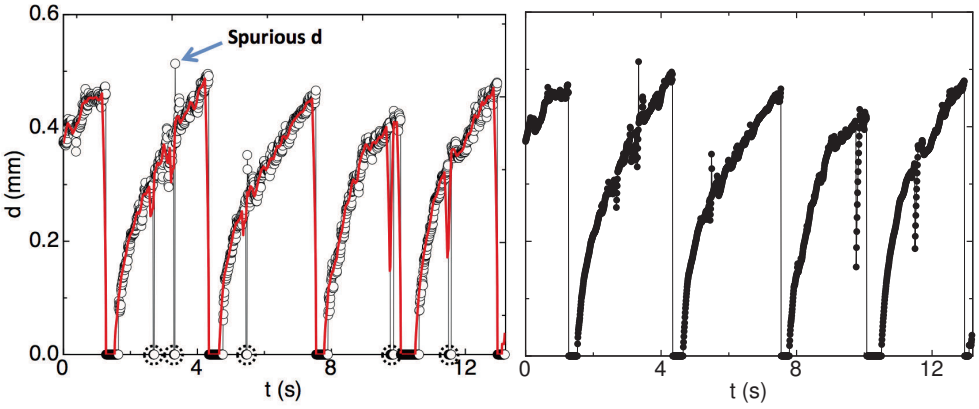

(a) (b)

Figure 3.B.1: Horizontal chord length d timeseries of growing and detaching bubbles at a single nucleating site. Each timeseries shows different steps involved in the image analysis of nucleating bubbles visualized from the top. In (a) circles present the outcome of step 3. Indicated are examples of spurious d values and of non-representative zero values which are marked by dotted circles around them. The solid line shows the moving average of the timeseries displayed in circles. The moving average replaced non-representative zeros with a positive d value, which became useful when finding a departing bubble (see figure 3.10). Displayed in (b) is the result obtained after step 4, which equals the timeseries in circles shown in (a) except for the frames when non-representative zeros were found. In such case non-representative zero values were substituted by the moving average corresponding d value.

analyzed. Departure was detected when from one frame i to the next one $i+1$ the bubble horizontal chord length decreased and was below a certain threshold at frame $i+1$. This was when step 4 was useful, otherwise departure would have been wrongly detected at one frame before a non-representative zero value. The bubble departure diameter d_{max} was saved as the value in the timeseries at frame i. Time difference between consecutive departure events δt was the difference between corresponding frame numbers and divided by the frame rate.

Step 6: manual correction. The algorithm was not successful in all cases, therefore timeseries acquired for all T_b and l values were inspected and manual correction of departing events was done when necessary. For example, out of focus passing bubbles could appear as very large diameters in the timeseries. If such a spurious bubble spatially coincided with a cavity at the departure frame then a non-physical bubble horizontal chord length would be wrongly detected as departing bubble.

3.C The role of dissolved air

Visualization of 2-phase flow from above in apparatus 1 showed that bubbles did not reach the top plate, independent on the elapsed time and superheat value. In apparatus 2 the same behavior was observed within the first day or so after filling the cell. However after a few days and at the same set temperatures $T_b^\star$ and $T_t^\star$, an increasing number of bubbles departing from the bottom plate reached the top plate and condensed there. This temporal dependence of the flow was an artifact associated to an increasing air concentration in the liquid.

We believe that the liquid inside the cylindrical cell had initially (after filling the cell) a smaller air concentration than the liquid outside it. The initial air concentration in the (apparatus 2) cell was the same as the one which led to reproducible and time independent results in apparatus 1 since the same procedure to fill it was followed. However the liquid filling the space between cell and sidewall could not be boiled in-situ and degassing by boiling was not possible, leading to a larger amount of air dissolved in it. A leak between the liquid inside and outside the cell must have existed, allowing for dissolved air to diffuse into the liquid inside the cell. In section 3.4.1 results from experiments performed directly after the cell had been filled and once the system had reached equilibrium were reported. Here we discuss the effect of a larger amount of dissolved air in 2-phase flow based on images acquired a four days after filling the cell and compare the results on bubble size and velocity after departure with the ones reported in section 3.4.1.

A close up movie of the nucleation process was captured without changing neither the camera nor the lens focus in order to compare d_x, d_z and Γ_d with the values obtained in section 3.4.1: $d_x = 45.0 \pm 2.0$ pixels, $d_z = 57.1 \pm 3.5$ pixels and $\Gamma_d = 0.79 \pm 0.03$. We analyzed 25 bubbles right before detaching from the surface and obtained: $d_x = 45.9 \pm 1.5$ pixels, $d_z = 57.5 \pm 2.2$ pixels and $\Gamma_d = 0.79 \pm 0.03$. Thus a larger air concentration in the liquid did not affect the bubble aspect ratio of bubbles right before departure.

We obtained the bubble radius $2R_b$ and vertical velocity U_z evolution in time of 8 non-merging bubbles. In figures 3.C.1a and 3.C.1b $2R_b$ is shown as a function of time for bubbles rising in liquid with different air concentrations; the latter shows $2R_b$ for the case with less dissolved air. Clearly, bubbles rising across a flow with less air dissolved condensed at a higher rate. Bubbles condensing slower in an environment with more air was also reflected in a larger instantaneous buoyancy and thus, as observed in figure 3.C.1c their vertical velocities were larger than when rising in liquid with less air, as shown in figure 3.C.1d. The heat flux current was increased by about 1.5% in the flow with larger air concentration reflecting the larger buoyancy of the bubbles due to their smaller condensation rate.

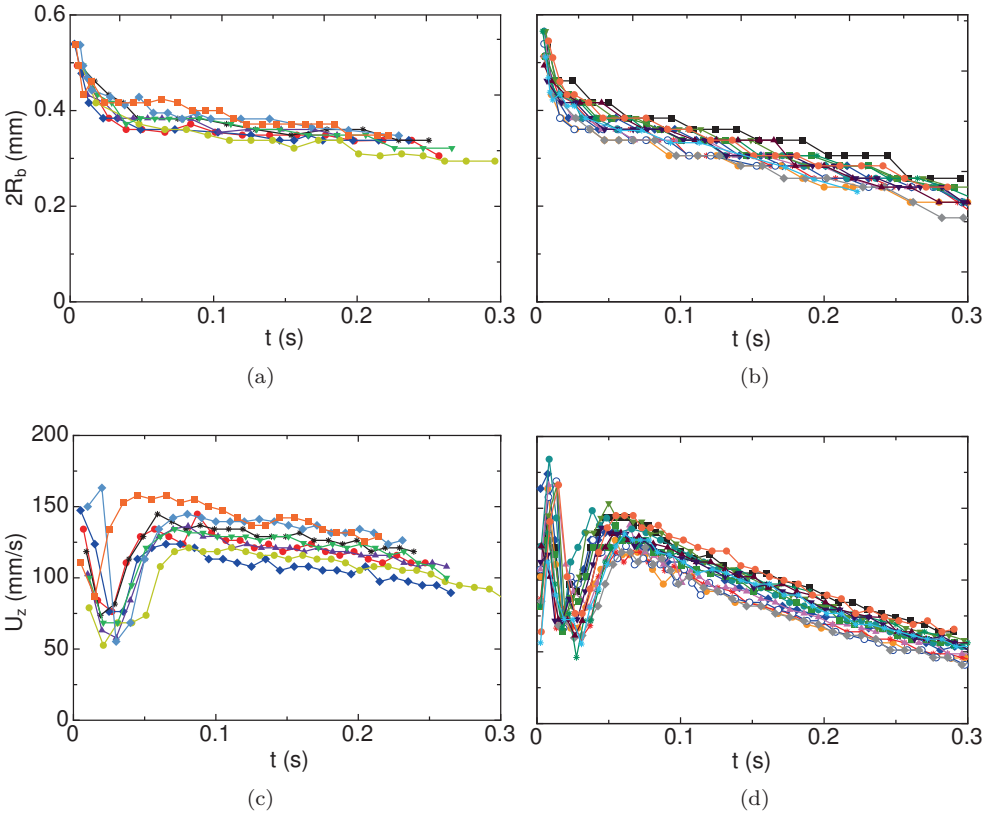

Figure 3.C.1: In (a) and (b) diameter $2R_b$ and in (c) and (d) vertical velocity U_z time evolution of bubbles which did not merge with others after detaching from the $l = 0.60$ mm wafer with $T_b - T_{on} \simeq 10$ K. (a) and (c) correspond to a larger air concentration in the liquid and (b) and (d) to an air concentration of about 23% in volume obtained from the filling procedure. Same color and symbol correspond to the same tracked bubble.

4
Summary and Outlook

In this thesis experimental work on 2-phase turbulent Rayleigh-Bénard (RB) convection was conducted. The experiments were performed under well-defined boiling conditions as vapor bubbles uniquely nucleated at pre-determined sites. These were cylindrical cavities of equal size etched on a silicon wafer used as the upper surface of the superheated bottom plate (bp). Silicon wafers with five different cavity separations l (thus different cavity densities) were used. The reference flow was the 1-phase flow, i.e. turbulent convective flow with no phase change, measured in the same RB cell and under the same thermal forcing as done for the 2-phase flow. This was possible by delaying the onset of nucleation, which was accomplished by assuring that the etched cavities were filled with (superheated) liquid.

The cell was cylindrical and its diameter equaled its height (aspect ratio $\Gamma = 1.0$). To prevent the appearance of uncontrolled nucleation sites at the edge of the cell where it was in contact with the bp, as found in preliminary experiments, the extent of the circular heated area was reduced and was located in the center of the bp. The etched area of the wafers was aligned with the heated area, and had the same diameter. The heated area was about 15 times smaller than the cooling area of the top plate. The flow studied here with modified geometry presented significant differences from the classical RB flow.

In chapter 2 the results presented quantified the effectiveness of boiling as a mode of heat transfer by measuring the system response of both 2-phase flow and the purely-convective reference flow. The non-dimensional heat-flux enhancement was expressed by the Nusselt number Nu difference between 2- and 1-phase flow. The vapor bubbles in the flow not only led to heat-flux enhancement, but also to changes in locally acquired temperature signals in the bulk flow. The heat-flux enhancement and local temperature modifications were explored in terms of some of the system parameters, namely the Rayleigh number Ra - ratio of buoyancy force to viscous

force, the Prandtl number Pr - ratio of viscous diffusion to thermal diffusion, the Jakob number Ja - ratio of sensible heat to latent heat of vaporization, the bottom plate temperature T_b and the number of nucleation sites. Increasing T_b, led to larger values of Ra and Ja, and to decreasing values of Pr.

In practice, a set of experiments started with 2-phase flow and large T_b values. As T_b was reduced, an increasing amount of nucleating sites turned inactive. The bp temperature, at which all sites deactivated was defined as the nucleation onset temperature T_{on} and the bp superheat was defined as $T_b - T_{on}$. All the experiments presented in this thesis were done for a fixed vertical temperature difference across the sample $\Delta T = T_b - T_t \simeq 16$ K, where T_t is the top plate temperature, while T_b and T_t varied.

The heat-flux enhancement was found to increase as $T_b - T_{on}$ became larger. The heat-flux enhancement presented no significant dependence on the total number of etched cavities, which varied by a factor of 59 by employing four bottom plates with a different l each. Only at the largest superheat values all or most of the nucleation sites were active and active site density was well defined. Therefore at a given large superheat value, the heat-flux enhancement per active site was considered as a function of active site density. The heat-flux enhancement per active site was found to increase with decreasing active site density and, as one would expect, it saturated for the case of a very small density.

The modifications to the bulk flow temperature due to the presence of bubbles measured at two different heights (at the mid-plane $z/L = 0.50$ and at about one-fourth of the cell height away from the bp $z/L = 0.28$) along the center-line of the sample were quantified. In general, none of the studied quantities varied significantly with superheat in 1-phase flow, and in 2-phase flow different cavity separations did not influence the results much. The stable thermal gradient measured in 1-phase flow (also found in classical RB flow) was augmented in the presence of bubbles. The temperature drop across the thermal boundary layer of the bp found in 1-phase flow (larger than in classical RB flow when the Oberbeck-Boussinesq approximation is valid) was reduced in 2-phase flow. Furthermore, at both heights the temperature standard deviation values were reduced in 2-phase flow, probably due to the fixed temperature of the bubbles, which by releasing or absorbing heat, smoothened the temperature gradients in the liquid. The skewness S of the temperature probability density function was positive in 1-phase flow at both heights, but larger at $z/L = 0.28$ than at mid-height. Positive skewness was associated to (hot) thermal plumes detaching from the bp and passing by the thermistors inserted in the flow. The positive S was the first indication that, in the modified geometry, plumes tend to travel more vertically than in classical RB flow, influencing the temperature distribution. For $T_b - T_{on} \lesssim 6$ K, S measured for 2-phase flow did not change with respect to S measured in 1-phase flow. However for $T_b - T_{on} \gtrsim 6$ K, S became a decreasing function of superheat. At $z/L = 0.28$, S became slightly negative at the largest superheat. The reduction in S was associated to the heat capacity provided by the bubbles, which reduced the large temperature gradients associated to plumes. The reduction only took place when enough detached bubbles were able to reach the location of the thermistors before condensing. This was the case at large superheat values, thus warmer bulk temperatures that allowed bubbles to reach higher, while their departure

from the bp occurred at a higher rate.

The heat-flux enhancement was found to be correlated with the modifications introduced by the vapor bubbles to the bulk temperature field. A larger heat-flux enhancement correlated with: (1) a smaller temperature drop across the thermal boundary layer, (2) a larger stabilizing temperature gradient in the bulk and (3) smaller temperature fluctuations around the mean.

Whether the LSC, observed to drag detached bubbles in one specific direction, was causing them to detach earlier, i.e. before achieving a volume, which in the absence of the LSC would have been larger, was investigated in chapter 2. By placing a short ring around the etched area in order to block the passage of the LSC, a slight increase in the heat-flux enhancement was measured, suggesting that the LSC indeed affected the nucleation and detachment of bubbles at the surface. Motivated by the fact that the modified geometry of the RB flow caused a significantly larger temperature drop across the bottom boundary layer than in the classical RB flow, a plastic cylinder nearly as tall as the cell was placed around the etched/heated area in order to partially isolate (thermally and physically) the liquid column above it. In that way the convective flow inside the column approached the classical RB flow, leading to warmer liquid in the bulk. The heat-flux enhancement showed a significant increment with respect to the case without such cylinder, especially at large superheat values. This finding indicated that the bubbles complete condensation was retarded, augmenting the effective buoyancy of the flow.

In chapter 3, the results obtained from high-speed flow visualization from the side and through the top plate of the RB sample were reported. Shadowgraph visualization of the flow showed that, given the modified geometry of the RB convective flow, the plumes detaching from both plates did not form a well defined large scale motion. Additionally, the detachment of plumes from the bp did not vary much over the entire surface, suggesting that there was a significant amount of heat transferred horizontally across the silicon wafer. The findings for 1-phase flow contrasted with the ones in 2-phase flow, in which a better defined LSC spanned the entire cell. In this case the detachment of plumes from the bp predominantly occurred from the heated area, showing that the nucleation of bubbles locally increased the effective thermal conductivity of the flow adjacent to the heated area. It was suggested that the well defined LSC in the presence of bubbles was related to the heat-flux enhancement and the increased effective buoyancy of the 2-phase flow. The dynamics of the plumes provided further insight into the reduced skewness of the local temperature probability distributions found for 2-phase flow at sufficiently large superheat values, reported in chapter 2. The skewness in 2-phase flow was not only reduced by the heat capacity of the bubbles, but also because the hot thermal plumes mostly moved horizontally close to the bp and were less likely to pass by the inserted thermistors (located in the bulk along the centerline) as compared to the 1-phase case.

The time-evolution of bubble radius right after departure showed a very large initial condensation rate associated to large gradients of the dominant parameters across the bottom boundary layer: Ja and the ratio of bubble surface radial velocity and relative stream velocity. The velocity components of the rising bubbles showed that the LSC dragged the bubbles horizontally close to the bottom plate and caused a significant decrease of their vertical velocity. Once the bubbles rose beyond the boundary

layer and out of the region of strong LSC influence, their vertical velocity increased and nearly re-established to its initial value. Once in the bulk, their condensation rate and vertical deceleration were constant. The bubble vertical velocity was at least one order of magnitude larger than the characteristic velocity of the LSC. The distance from the bp at which different bubbles fully condensed presented a wide distribution, however this height showed to be correlated to the maximal vertical velocity achieved along single bubble trajectories.

Bubble growth-departure cycles at a large number of active cavities were recorded from above for several bottom plate superheat values (from ~ 3 to 12 K). It was found that bubble volume grew about linearly with time and the proportionality constant increased the larger the superheat value was. At departure, the mean horizontal bubble chord length d_{max} was about 0.5 mm over the superheat range between ~ 3 and 10 K for the wafer with $l = 0.6$ mm; d_{max} increased up to about 0.65 mm for the case of isolated and non-interacting bubbles at the largest superheat value, and decreased up to approximately 0.4 mm for the lowest superheat and $l = 1.0$ mm.

At the moment of departure, the bubbles shape looked similar to a falling drop up side down. The volume of the bubbles at departure remained below half of the predicted maximal volume attainable V_{max} if only surface tension and buoyancy determine the departure of a spherical bubble and thermal effects are neglected. A heat flux rate into the bubble smaller than a certain critical value could have been responsible for the fact that the bubbles in the experiments presented in this thesis were smaller than V_{max}.

The mean value of the time between consecutive departures, i.e. the inverse of the departure frequency, decreased exponentially as superheat became larger and did not depend on cavity separation. As the superheat was reduced, the fluctuations around the mean time between consecutive departures became larger, reflecting the irregularity of the departure process. For a given superheat, the larger the cavity separation was, the more irregular in time departed the bubbles. Larger deviations from the mean departure frequency were associated to temperature fluctuations in the nearby liquid, which affected isolated bubbles more than bubbles surrounded by other growing bubbles. This is in accordance with the observation made in chapter 2 that, for a given superheat value, the larger the cavity separation was, the easier it was for an active site to deactivate.

The enhancement of heat per unit time transferred by the boiling surface had three contributions: (1) the latent heat required for the growth of bubbles, (2) microconvection as consequence of the thermal boundary layer disruption due to the growth of bubbles and generated by the wake of departing bubbles, as well as transient conduction necessary to rebuild the thermal boundary layer at the location from where a bubble departed, and (3) the increase in the effective flow buoyancy together with the latent heat of the bubbles transported by advection. In chapter 3, the average latent heat per unit time required for the growth of vapor bubbles at a single active nucleation site was calculated based on the bubble volume at departure and the rate of departure. The relative contribution of latent heat to the enhanced heat transferred by the surface per active site was found to be an increasing function of superheat, reaching up to 25%. Furthermore, the absolute contribution of the effective buoyancy was indirectly found to increase with superheat as the bubble volume did not

change over the studied range and that the departure frequency grew exponentially with superheat.

The results obtained in this thesis have contributed to better understand the different mechanisms responsible for the heat-flux enhancement due to vapor-bubble nucleation in RB convection. The well-defined LSC visualized in 2-phase flow could be studied in detail by performing measurements of the flow strength and dynamics as a function of superheat and see how they compare to the case without bubbles. The turn-over time of the LSC could be used to obtain a characteristic velocity to be compared with the rising velocity of the bubbles. Furthermore, it would be interesting to investigate the Reynolds number dependence on superheat as compared to the 1-phase flow. In fact these experiments are already being pursued in our laboratory.

It would also be interesting to study the flow under different constant thermal forcing or ΔT values, while varying the superheat, which would lead to expanding the Rayleigh number range investigated so far (1.4×10^{10} - 2×10^{10}). The limiting factor in the increase of superheat is the condensation rate, which if not large enough led to the accumulation of vapor in the sample, preventing the system from reaching a steady state. A larger ΔT would allow to explore a wider superheat range, since one can expect that the thermal boundary layers would sustain a larger temperature drop than for the case studied in this thesis ($\Delta T \simeq 16$ K), and that the vapor bubbles departing from a larger superheated surface would encounter bulk temperatures low enough so that they would fully condense as they rise. Considering that larger superheat values led to higher heat-flux enhancements, one could expect to access even larger heat-flux enhancement for larger ΔT.

Another interesting parameter to explore would be the aspect ratio of the cell. In 2-phase flow a smaller aspect ratio would imply longer times for the rising vapor bubbles to fully condense before reaching the top plate. This suggests that given a ΔT value, a smaller Γ could sustain a wider range of superheats before meeting the experimental limitation of accumulating vapor with respect to a smaller Γ. In this way one could pursue the study of the fully developed nucleate boiling region in a RB convective sample.

References

[1] G. Warrier, V. Dhir, and D. Chao, "Nucleate Pool Boiling eXperiment (NPBX) in microgravity: International Space Station", Int. J. Heat Mass Tran. **83**, 781–798 (2015).

[2] V. Dhir, "Boiling heat transfer", Annu. Rev. Fluid Mech. **30**, 365–401 (1998).

[3] A. Zou and S. Maroo, "Critical height of micro/nano structures for pool boiling heat transfer enhancement", Appl. Phys. Lett. **103** (2013).

[4] Jo.H., S. Kim, H. Park, and M. Kim, "Critical heat flux and nucleate boiling on several heterogenous wetting surfaces: Controlled hydrophobic patterns on a hydrophilic substrate", Int. J. Multiphas. Flow **62**, 101–109 (2014).

[5] V. Carey, *Statistical Thermodynamics and Microscale Thermophysics* (Cambridge University Press, New York, NY) (1999).

[6] V. Carey, *Liquid-Vapor Phase-Change Phenomena*, 2nd edition (Taylor and Francis, New York, NY) (2008).

[7] S. Witharana, B. Phillips, S. Strobel, H. Kim, T. McKrell, J.-B. Chang, J. Buongiorno, K. Berggren, L. Chen, and Y. Ding, "Bubble nucleation on nano- to micro-size cavities and posts: An experimental validation of classical theory", J. Appl. Phys. **112**, 064904–1–5 (2012).

[8] A. A. Atchley and A. Prosperetti, "The crevice model of bubble nucleation", J. Acoust. Soc. Am. **86**, 1065–1084 (1989).

[9] Y. Hsu, "On the size range of active nucleation cavities on a heating surface", J. Heat Transf. **84** (1962).

[10] A. Singh, B. Mikic, and Rohsenow, "Active sites in boiling", J. Heat Transf. **98**, 401–406 (1976).

[11] P. Griffith and J. Wallis, "The role of surface conditions in nucleate boiling", Chem. Eng. Prog. S. Ser. **56**, 49–63 (1960).

[12] Y. Nam, J. Wu, G. Warrier, and Y. Sungtaek Ju, "Experimental and numerical study of single bubble dynamics on a hydrophobic surface", J. Heat Transf. **131**, 121004–1–7 (2009).

[13] A. Betz, J. Xu, and D. Qiu, H. Attinger, "Do surfaces with mixed hydrophilic and hydrophobic areas enhance pool boiling?", Applied Phys. Lett. **97** (2010).

[14] B. Bourdon, R. Rioboo, M. Marengo, E. Gosselin, and J. De Coninck, "Influence of the wettability on the boiling onset", Langmuir **28**, 1618–1624 (2011).

[15] R. Murphy and A. Bergles, "Subcooled flow boiling of fluorocarbons - hysteresis and dissolved gas effects on heat transfer", Proceedings of heat transfer and fluid mechanics Inst., Stanford University Press 400–416 (1972).

[16] M. Steinke and S. Kandlikar, "Control and dissolved air in water during flow boiling in micro channels", Int. J. Heat Mass Tran. **47**, 1925–1935 (2004).

[17] I. Pioro, W. Rohsenhow, and S. Doerffer, "Nucleate pool-boiling heat transfer. i: review of parametric effects of boiling surface", Int. J. Heat Mass Tran. **47**, 5033–5044 (2004).

[18] G. Barthau, "Active nucleation site density and pool boiling heat transfer - an experimental study", Int. J. Heat Mass Tran. **35**, 271–278 (1992).

[19] H. Kubo, H. Takamatsu, and H. Honda, "Effects of size and number density of micro-reentrant cavities on boiling heat transfer from a silicon chip immersed in degassed and gas-dissolved FC-72", J. Enhanc. Heat Transf. **6**, 151–160 (1999).

[20] N. Bremond, M. Arora, C. D. Ohl, and D. Lohse, "Controlled multibubble surface cavitation", Phys. Rev. Lett. **96** (2006).

[21] A. Das, P. Das, and P. Saha, "Nucleate boiling of water from plain and structured surfaces", Exp. Therm. Fluid Sci. **31**, 967–977 (2007).

[22] O. Enríquez, C. Hummelink, G.-W. Bruggert, D. Lohse, A. Prosperetti, D. van der Meer, and C. Sun, "Growing bubbles in a slightly supersaturated liquid solution", Rev. Sci. Instrum. **84** (2013).

[23] J. Kim, "Review of nucleate pool boiling bubble heat transfer mechanism", Int. J. Multiphas. Flow **35**, 1067–1076 (2009).

[24] A. Prosperetti and M. Plesset, "Vapour-bubble growth in a superheated liquid", J. Fluid Mech. **85**, 349–368 (1978).

[25] M. Plesset and S. A. Zwick, "The growth of vapor bubbles in superheated liquids", J. Appl. Phys. **25**, 493–500 (1954).

[26] H. Forster and N. Zuber, "Growth of vapor bubbles in superheated liquid", J. Appl. Phys. **25**, 474–478 (1954).

[27] W. Fritz, "Berechnung des Maximalvolumens von Dampfblasen", Physik. Zeitschr. 379–385 (1935).

[28] J. Klausner, R. Mei, D. Bernhard, and L. Zeng, "Vapor bubble departure in forced convection boiling", Int. J. Heat Mass Tran. **36**, 651–662 (1993).

[29] L. Zeng, J. Klausner, and R. Mei, "A unified model for prediction of bubble detachment diameters in boiling systems - i. pool boiling", Int. J. Heat Mass Tran. **36**, 2261–2270 (1993).

[30] H. Oğuz and A. Prosperetti, "Dynamics of bubble growth and detachment from a needle", J. Fluid Mech. **257**, 111–145 (1993).

[31] J. Kim and M. Kim, "On the departure behaviors of bubble at nucleate pool boiling", Int. J. Multiphas. Flow **32**, 1269–1286 (2006).

[32] D. K. Hollingsworth, L. C. Witte, and M. Figueroa, "Enhancement of heat transfer behind sliding bubbles", J. Heat Transf. **131** (2009).

[33] C. Brennen, *Fundamentals of Multiphase Flows* (Cambridge University Press) (2005).

[34] D. Legendre, Borée, and J. Magnaudet, "Thermal and dynamic evolution of a spherical bubble moving steadily in a superheated or subcooled liquid", Phys. Fluids **10** (1998).

[35] M. Plesset and A. Prosperetti, "Bubble dynamics and cavitation", Annu. Rev. Fluid Mech. **9**, 145–185 (1977).

[36] C. Ohl, A. Tijink, and A. Prosperetti, "The added mass of an expanding bubble", J. Fluid Mech. **482**, 271–290 (2003).

[37] J. de Vries, S. Luther, and D. Lohse, "Induced bubble shape oscillations and their impact on the rise velocity", Eur. Phys. J. B **29**, 503–509 (2002).

[38] J. Magnaudet and D. Legendre, "The viscous drag force on a spherical bubble with a time-dependent radius", Phys. Fluids **10** (1998).

[39] Y. Hao and A. Prosperetti, "The collapse of vapor bubbles in a spatially non-uniform flow", Int. J. Heat Mass Tran. **43**, 3539–3550 (2000).

[40] D. Lohse and A. Prosperetti, "Controlling bubbles", J. Phys-Condens. Mat. **15**, 415–420 (2003).

[41] B. Yang and A. Prosperetti, "Vapour-bubble collapse in isothermal and non-isothermal liquids", J. Fluid Mech. **601**, 253–279 (2008).

[42] D. W. Moore, "The velocity of rise of distorted gas bubbles in a liquid of small viscosity", J. Fluid Mech. **23**, 749–766 (1965).

[43] L. Zhang and M. Shoji, "Nucleation site interaction in pool boiling on the artificial surface", Int. J. Heat Mass Tran. **46**, 513–522 (2003).

[44] J. Bi, D. Christopher, X. Lin, and X. Li, "Effects of nucleation site arrangement and spacing on bubble coalescence characteristics", Exp. Therm. Fluid Sci. **52**, 116–127 (2014).

[45] Y. Yang, E. P. van der Poel, R. Ostilla-Mónico, C. Sun, R. Verzicco, S. Grossmann, and D. Lohse, "Salinity transfer in bounded double diffusive convection", J. Fluid Mech. **768**, 476–491 (2015).

[46] I. Held and A. Hou, "Nonlinear axially symmetric circulations in a nearly inviscid atmosphere", J. Atmos. Sci. **37**, 515–533 (1980).

[47] S. Rahmstorf, "Thermohaline ocean circulation", in *Encyclopedia of Quaternary Sciences*, edited by S. Elias (Elsevier Science) (2006).

[48] E. Bodenschatz, W. Pesch, and G. Ahlers, "Recent developments in Rayleigh-Bénard convection", Ann. Rev. Fluid Mech. **32**, 709–778 (2000).

[49] A. Getling, *Rayleigh-Bénard convection: structures and dynamics* (World Scientific Publishing Co. Pte. Ltd.) (1998).

[50] P. Drazin and W. Reid, *Hydrodynamic stability* (Cambridge University Press) (1981).

[51] S. Chandrasekhar, *Hydrodynamic and Hydromagnetic Stability* (Dover) (1981).

[52] G. Schubert, D. Turcotte, and P. Olson, *Mantle Convection in the Earth and Planets* (Cambridge University Press) (2001).

[53] G. Glatzmaier, R. Coe, L. Hongre, and P. Roberts, "The role of the Earth's mantle in controlling the frequency of geomagnetic reversals", Nature **401**, 885–890 (1999).

[54] D. Hathaway, L. Upton, and O. Colegrove, "Giant convection cells found in the sun", Science **342**, 1217–1219 (2013).

[55] F. Cattaneo, T. Emonet, and N. Weiss, "On the interaction between convection and magnetic fields", Astrophys. J. **588**, 1183 (2003).

[56] L. P. Kadanoff, "Turbulent heat flow: Structures and scaling", Phys. Today **54**, 34–39 (2001).

[57] G. Ahlers, S. Grossmann, and D. Lohse, "Heat transfer and large scale dynamics in Rayleigh-Bénard convection", Rev. Mod. Phys. **81**, 503–537 (2009).

[58] G. Ahlers, "Turbulent convection", Physics **2**, 74–1–7 (2009).

[59] D. Lohse and K.-Q. Xia, "Small-scale properties of turbulent Rayleigh-Bénard convection", Annu. Rev. Fluid Mech. **42**, 335–364 (2010).

[60] F. Chillà and J. Schumacher, "New perspectives in turbulent Rayleigh-Bénard convection", Eur. Phys. J. E **35**, 58–1–25 (2012).

[61] S. Grossmann and D. Lohse, "Scaling in thermal convection: a unifying theory", J. Fluid Mech. **407** (2000).

[62] S. Grossmann and D. Lohse, "Thermal convection for large Prandtl numbers", Phys. Fluids **16** (2004).

[63] S. Grossmann and D. Lohse, "On geometry effects in Rayleigh-Bénard convection", Phys. Fluids **486** (2004).

[64] S. Grossmann and D. Lohse, "Fluctuations in turbulent Rayleigh-Bénard convection: the role of plumes", Phys. Fluids **16** (2004).

[65] J. Zhong, D. Funfschilling, and G. Ahlers, "Enhanced heat transport by turbulent two-phase Rayleigh-Bénard convection", Phys. Rev. Lett. **102**, 124501–1–4 (2009).

[66] P. Oresta, R. Verzicco, D. Lohse, and A. Properetti, "Heat transfer mechanisms in bubbly Rayleigh-Bénard convection", Phy. Rev. E **80**, 026304–1–11 (2009).

[67] L. Schmidt, P. Oresta, F. Toschi, R. Verzicco, D. Lohse, and A. Prosperetti, "Modification of turbulence in Rayleigh-Bénard convection by phase change", New J. Phys. **13**, 025002–1–10 (2011).

[68] R. Lakkaraju, L. Schmidt, P. Oresta, F. Toschi, R. Verzicco, D. Lohse, and A. Prosperetti, "Effect of vapor bubbles on velocity fluctuations and dissipation rates in bubble Rayleigh-Bénard convection", Phys. Rev. E **84**, 036312–1–7 (2011).

[69] L. Biferale, P. Perlekar, M. Sbragaglia, and F. Toschi, "Convection in multiphase fluid flows using lattice Boltzmann methods", Phys. Rev. Lett. **108**, 104502–1–5 (2012).

[70] R. Lakkaraju, R. Stevens, P. Oresta, R. Verzicco, D. Lohse, and A. Prosperetti, "Heat transport in bubbling turbulent convection", P. Natl. Acad. Sci. USA **110**, 9237–9242 (2013).

[71] R. Lakkaraju, F. Toschi, and D. Lohse, "Bubbling reduces intermittency in turbulent thermal convection", J. Fluid Mech. **745**, 1–24 (2014).

[72] S. Weiss and G. Ahlers, "Nematic-isotropic phase transition in turbulent thermal convection", J. Fluid Mech. **716**, 308–328 (2013).

[73] E. Harvey, D. Barnes, W. McElroy, A. Whiteley, D. Pease, and K. Cooper, "Bubble formation in animals", J. Cell Compar. Physl. **24**, 1–22 (1944).

[74] C.-Y. Han and P. Griffith, "The mechanism of heat transfer in nucleate pool boiling", Int. J. Heat Mass Tran. **8** (1965).

[75] T. Yabuki and O. Nakabeppu, "Heat transfer characteristics of isolated bubble nucleate boiling of water", Proceedings of the ASME/JSME 2011 8th Thermal Engineering Joint Conference T10196–T10196 (2011).

[76] C. H. M. Baltis and C. W. M. van der Geld, "Heat transfer mechanisms of a vapour bubble growing at a wall in saturated upward flow", J. Fluid Mech. **771**, 264–302 (2015).

[77] G. Ahlers, D. Cannel, L. Berge, and S. Sakurai, "Thermal conductivity of the nematic liquid crystal 4-n-pentyl-4'-cyanobiphenyl", Phys. Rev. E **49**, 545–553 (1994).

[78] X. Xu, K. M. S. Bajaj, and G. Ahlers, "Heat transport in turbulent Rayleigh-Bénard convection", Phys. Rev. Lett. **84**, 4357–4360 (2000).

[79] G. Ahlers and X. Xu, "Prandtl-number dependence of heat transport in turbulent Rayleigh-Bénard convection", Phys. Rev. Lett. **86**, 3320–3323 (2001).

[80] D. Funfschilling, E. Brown, A. Nikolaenko, and G. Ahlers, "Heat transport by turbulent Rayleigh-Bénard convection in cylindrical cells with aspect ratio one and larger.", J. Fluid Mech. **536**, 145–154 (2005).

[81] P. Wei and G. Ahlers, "Logarithmic temperature profiles in the bulk of turbulent Rayleigh-Bénard convection for a Prandtl number of 12.3", J. Fluid Mech. **758**, 809–830 (2014).

[82] X. He, D. van Gils, E. Bodenschatz, and G. Ahlers, "Logarithmic spatial variations and universal f^{-1} power spectra of temperature fluctuations in turbulent Rayleigh-Bénard convection", Phys. Rev. Lett. **112**, 174501–1–4 (2014).

[83] O. Shpak, L. Stricker, M. Versluis, and D. Lohse, "The role of gas in ultrasonically driven vapor bubble growth", Phys. Med. Biol. **58**, 2523–2535 (2013).

[84] A. Nagy, "Radial etch rate nonuniformity in reactive ion etching", J. Electrochem. Soc. **131**, 1871–1875 (1984).

[85] A. Kao and H. Stenger, "Analysis of nonuniformities in the plasma etching of silicon with cf 4/0", J. Electrochem. Soc. **137**, 954–960 (1990).

[86] R. J. A. M. Stevens, E. P. van der Poel, S. Grossmann, and D. Lohse, "The unifying theory of scaling in thermal convection: the updated prefactors", J. Fluid Mech. **730**, 295–308 (2013).

[87] G. Ahlers, E. Brown, F. Fontenele Araujo, D. Funfschilling, S. Grossmann, and D. Lohse, "Non-Oberbeck-Boussinesq effects in strongly turbulent Rayleigh-Bénard convection", J. Fluid Mech. **569**, 409–445 (2006).

[88] A. Tilgner, A. Belmonte, and A. Libchaber, "Temperature and velocity profiles of turbulence convection in water", Phys. Rev. E **47**, R2253–R2256 (1993).

[89] E. Brown and G. Ahlers, "Temperature gradients, and search for non-Bousinesq effects, in the interior of turbulent Rayleigh-Bénard convection", Europhys. Lett. **80**, 14001–1–6 (2007).

[90] A. Oberbeck, "Über die Wärmeleitung der Flüssigkeiten bei Berücksichtigung der Strömungen infolge von Temperaturdifferenzen", Ann. Phys. Chem. **7**, 271–292 (1879).

[91] J. Boussinesq, *Theorie analytique de la chaleur, Vol. 2* (Gauthier-Villars, Paris) (1903).

[92] A. Belmonte, A. Tilgner, and A. Libchaber, "Turbulence and internal waves in side-heated convection", Phys. Rev. E **51**, 5681–5687 (1995).

[93] G. Ahlers, E. Bodenschatz, D. Funfschilling, S. Grossmann, X. He, D. Lohse, R. J. A. M. Stevens, and R. Verzicco, "Logarithmic temperature profiles in turbulent Rayleigh-Bénard convection", Phys. Rev. Lett. **109** (2012).

[94] G. Ahlers, E. Bodenschatz, and X. He, "Logarithmic temperature profiles of turbulent Rayleigh-Bénard convection in the classical and ultimate state for a Prandtl number of 0.8", J. Fluid Mech. **758**, 436–467 (2014).

[95] E. Brown and G. Ahlers, "Large-scale circulation model of turbulent Rayleigh-Bénard convection", Phys. Rev. Lett. **98** (2007).

[96] E. Brown and G. Ahlers, "A model of diffusion in a potential well for the dynamics of the large-scale circulation in turbulent Rayleigh-Bénard convection", Phys. Fluids **20** (2008).

[97] G. Ahlers, "Experiments on thermally driven convection", in *Pattern Formation in Liquid Crystals*, 165–220 (Springer) (1996).

[98] S. Sakurai, A. Tschammer, W. Pesch, and G. Ahlers, "Convection in the presence of a first-order phase change", Phys. Rev. E **60** (1999).

[99] F. Busse and J. Whitehead, "Instabilities of convection rolls in a high Prandtl number fluid", J. Fluid Mech. **47**, 305–320 (1971).

[100] S. Rasenat, G. Hartung, B. Winkler, and I. Rehberg, "The shadowgraph method in convection experiments", Exp. Fluids **7**, 412–420 (1989).

[101] J. Bruyn, E. Bodenschatz, S. Morris, S. Trainoff, Y. Hu, D. Cannell, and G. Ahlers, "Apparatus for the study of Rayleigh-Bénard convection in gasses under pressure", Rev. Sci. Instr. **67** (1996).

[102] S. Trainoff and D. Cannel, "Physical optics treatment of the shadowgraph", Phys. Fluids **14**, 1340–1363 (2002).

[103] H. Xi, S. Lam, and K. Xia, "From laminar plumes to organized flows: the onset of large-scale circulation in turbulent thermal convection", J. Fluid Mech. **503**, 47–46 (2004).

[104] H. Xi and K. Xia, "Azimuthal motion, reorientation, cessation, and reversal of the large-scale circulation in turbulent thermal convection: A comparative study in aspect ratio one and one-half geometries", Phys. Rev. E **78** (2008).

[105] A. Okhotsimskii, "The thermal regime of vapour bubble collapse at different Jacob numbers", Int. J. Heat Mass Tran. **31** (1988).

[106] Y. Chen and F. Mayinger, "Measurements of heat transfer at the phase interface of condensing bubbles", Int. J. Multiphas. Flow **18**, 877–890 (1992).

[107] W. Sluyter, P. Slooten, C. Copraji, and A. Chesters, "The departure size of pool-boiling bubbles from artificial cavities at moderate and high pressures", Int. J. Multiphase Flow **17**, 153–158 (1991).

Samenvatting

In dit proefschrift wordt het experimentele werk van 2-fase turbulente Rayleigh-Bénard (RB) convectie gepresenteerd. De experimenten zijn uitgevoerd onder goed begrensde kokende condities doordat dampbellen alleen ontstonden op vooraf bepaalde posities. Dat waren cilindervormige holtes van gelijke vorm en grootte geëtst in een silicium plaat die werd gebruikt als het oppervlak van de verwarmde bodemplaat (bp). Er zijn silicium platen met vijf verschillende afstanden l tussen de holtes, dus met vijf verschillende dichtheden, gebruikt. De vloeistofstroming die ter referentie is gebruikt, is de 1-fasestroming, dus turbulente convectiestroming zonder faseovergangen gemeten in dezelfde RB cel en met hetzelfde temperatuurverschil als voor de 2-fasestroming. Dit was mogelijk door het ontstaan van nucleatie te vertragen door ervoor te zorgen dat de geëtste holtes gevuld waren met (oververhitte) vloeistof.

De cel was cilindrisch met een diameter die gelijk was aan de hoogte (aspectverhouding $\Gamma = 1.0$). Uit voorgaande experimenten was gebleken dat er ongecontroleerde nucleatieplekken waren bij de rand van de cel, waar de bp aan de zijkant van de cel grensde. Om dit te voorkomen, was het verwarmde oppervlak verkleind tot een cirkelvormig gebied in het midden van de bp. Het geëtste deel van de silicium plaat bevond zich precies op dezelfde plaats als het verwarmde deel en had dus dezelfde diameter. Het verwarmde oppervlak was ongeveer 15 keer kleiner dan de koude topplaat. De bestudeerde stroming met gewijzigde geometrie gaf significante verschillen in vergelijking met de klassieke RB-stroming.

In hoofdstuk 2 werden de resultaten van de effectiviteit van het koken als functie van de warmteoverdracht gekwantificeerd door de respons van het systeem van zowel 2-fasestroming als de puur convectieve referentiestroming te meten. De toename van de niet-dimensionale warmtestroom was uitgedrukt in het verschil in het getal van Nusselt Nu tussen de 2- en 1-fasestroming. De dampbellen in de stroming zorgden niet alleen voor toename van de warmtestroom, maar ook voor veranderingen in de verkregen temperatuursignalen in de bulkstroom. De toename van de warmtestroom en de lokale temperatuurveranderingen zijn onderzocht afhankelijk van de systeemparameters. Te weten het getal van Rayleigh Ra - de verhouding tussen de gravitatiekracht en viskeuze kracht, het getal van Prandtl Pr - de verhouding tussen impulsoverdracht en warmteoverdracht, het getal van Jakob Ja - de verhouding tussen voelbare warmte en latente warmte van verdamping, de temperatuur T_b van de bodemplaat en het aantal nucleatieplekken. Een toenemende T_b zorgde voor grotere waarden van Ra en Ja en voor afnemende waarden van Pr.

In de praktijk werd een meetserie gestart voor 2-fasestroming met een hoge T_b. Vervolgens werd T_b verlaagd waardoor er steeds meer nucleatieplekken inactief werden. De temperatuur T_b waarbij alle nucleatieplekken inactief waren, was gedefinieerd

als de begin van nucleatie temperatuur T_{on} en de oververhitting van de bodemplaat was gedefinieerd als $T_b - T_{on}$. Alle experimenten die in dit proefschrift gepresenteerd worden, waren uitgevoerd met een constant temperatuurverschil over de cel $\Delta T = T_b - T_t \simeq 16$ K, waarbij T_b en T_t dus elke keer evenveel aangepast werden en waar T_t de temperatuur van de topplaat is.

Uit de experimenten bleek dat de warmtestroom toenam wanneer $T_b - T_{on}$ groter werd. De toename van de warmtestroom bleek niet significant af te hangen van het totale aantal geëtste holtes, die varieerden met een factor van 59 door vier bodemplaten te gebruiken met elk een andere l tussen de holtes. Alleen bij de hoogste waarden van T_b waren alle of bijna alle nucleatieplekken actief en was de holtedichtheid dus een goede graadmeter. Daarom was voor een gegeven temperatuur, die veel groter was dan de begintemperatuur van nucleatie T_{on}, de toename van warmtestroom per actieve nucleatieplek beschouwd als functie van actieve holtedichtheid. De toename van warmtestroom per actieve plek bleek toe te nemen met afnemende actieve holtedichtheid en, zoals men zou verwachten, was het verzadigd in het geval van een hele lage dichtheid.

De verandering van de temperatuur van de bulkstroom als gevolg van de aanwezigheid van dampbellen is bepaald in het midden van de cel voor twee verschillende hoogtes (in het middenvlak $z/L = 0.50$ en op een hoogte van $z/L = 0.28$ boven de bp). Geen van deze bestudeerde waarden veranderde significant bij oververhitting in 1-fasestroming, in de 2-fasestroming beïnvloedde de holtedichtheid de resultaten niet veel. De stabiele thermische gradiënt gemeten in 1-fasestroming, die ook aanwezig is in klassieke RB convectie, was uitgebreid voor de aanwezigheid van bellen. Het temperatuurverval over de thermische grenslaag van de bodemplaat in 1-fasestroming (groter dan klassieke RB stroming wanneer de Oberbeck-Boussinesq benadering geldig is) was kleiner in 2-fasestroming. Daarnaast waren op beide hoogtes de waarden voor de standaarddeviatie van de temperatuur kleiner in de 2-fasestroming, waarschijnlijk door de constante temperatuur van de bellen, die door het opnemen of vrijlaten van warmte, de temperatuurschommelingen verminderden. De scheefheid S van de kansdichtheid van de temperatuur was positief in 1-fasestroming op beide hoogtes, maar groter op $z/L = 0.28$ dan in het middenvlak. Positieve scheefheid werd verklaard door (warme) thermische pluimen die omhoog kwamen van de bp en de thermistors in de vloeistof passeerden. De positieve waarde van S was de eerste indicatie dat, in de aangepaste geometrie, de pluimen zich relatief meer verticaal voortbewogen dan in klassieke RB stroming, wat de temperatuurverdeling beïnvloedde. Voor waarden van $T_b - T_{on} \lesssim 6$ K, veranderde S in de 2-fasestroming niet ten opzichte van S in de 1-fasestroming. Maar voor waarden van $T_b - T_{on} \gtrsim 6$ K, nam de waarde van S af als een functie van de oververhitting. Op de hoogte $z/L = 0.28$ werd de waarde S nipt negatief op de grootste oververhitting. De verlaging van S kan verklaard worden door de warmtecapaciteit van de bellen, die de grote temperatuurgradiënten van de pluimen neutraliseren. De verlaging vond alleen plaats wanneer er genoeg bellen de hoogte van de thermistors bereikten voordat ze gecondenseerd waren: een grotere oververhitting van de bp zorgde voor een warmere bulktemperatuur, waardoor de bellen hoger kwamen en met een hogere frequentie loslieten van de bp. De toename van warmtestroom bleek gecorreleerd te zijn met de veranderingen van de bulktemperatuur als gevolg van de aanwezigheid van dampbellen. Een grotere toename van

warmtestroom correleerde met: (1) een kleiner temperatuurverval over de thermische grenslaag, (2) een grotere stabiele temperatuurgradiënt in de bulk en (3) kleinere fluctuaties van de temperatuur.

In hoofdstuk 2 was onderzocht of de LSC, die de losgelaten bellen in eenzelfde richting duwde, ervoor zorgde dat de bellen eerder loslieten voordat ze een bepaald volume bereikt hadden ten opzichte van wanneer de LSC afwezig zou zijn. Door een korte ring om het geëtste oppervlak te plaatsen om de stroming van de LSC tegen te houden, was een kleine toename van de warmtestroom gemeten, wat erop duidde dat de LSC inderdaad de nucleatie en het loslaten van de bp beïnvloedde. Ingegeven door het feit dat de gewijzigde geometrie van de RB stroming een groter temperatuurverval over de thermische grenslaag bij de bodemplaat veroorzaakte dan in de klassieke RB stroming, was er een plastic cilinder, die bijna even hoog was als de cel, om het geëtste/verwarmde oppervlak geplaatst om een vloeistofkolom gedeeltelijk te isoleren (zowel thermisch als fysiek). Zodoende benaderde de convectiestroming in de smalle cilinder de klassieke RB stroming, wat zorgde voor een warmere vloeistof in de bulk. De warmtestroom met cilinder was significant groter dan zonder een dergelijke cilinder en in het bijzonder bij grotere waarden van oververhitting. Dit resultaat wees erop dat de gehele condensatie van de bellen vertraagd werd, waardoor het effectieve drijfvermogen van de stroom verhoogd werd.

In hoofdstuk 3 werden de resultaten uitgelegd van de hoge-snelheidsvisualisatie van stromingen door de zijkant en bovenkant van een RB cel. Visualisatie van de vloeistofstroom met behulp van de shadowgraph-techniek bracht de thermische pluimen van zowel de bodemplaat als de topplaat en de dynamieken in beeld. Hieruit bleek dat in de aangepaste geometrie de pluimen, die van beide platen vertrekken, op grote schaal geen duidelijke stroming vormden. Daarnaast bleek dat de pluimen die van de bp vertrokken, niet veel varieerden over het gehele oppervlak, wat erop duidde dat een significante hoeveelheid warmte horizontaal over de silicium plaat geleid werd. De resultaten voor de 1-fasestroming staken af tegen die van de 2-fasestroming, waarin een duidelijkere LSC de gehele cel vulde. Daarnaast lieten de pluimen voornamelijk los op de plaats van het verwarmde oppervlak, wat laat zien dat lokaal de effectieve thermische geleidbaarheid van de stroming langs het verwarmde oppervlak verhoogd werd door de nucleatie van dampbellen. Het is mogelijk dat de goed gedefinieerde LSC in de aanwezigheid van bellen gerelateerd is aan de toename van de warmtestroom en het verhoogde effectieve drijfvermogen van de 2-fasestroming. De dynamica van de pluimen gaf een verbeterd inzicht in de scheefheid van de kansverdeling van de lokale temperatuur voor de 2-fasestroming bij voldoende grote waarden van oververhitting, wat in hoofdstuk 2 behandeld werd. De scheefheid in de 2-fasestroming was niet alleen verkleind door de warmtecapaciteit van de bellen, maar ook omdat de warme thermische pluimen zich voornamelijk horizontaal dicht bij de bp verplaatsten, waardoor het in vergelijking met de 1-fasestroming minder waarschijnlijk was dat ze de thermistors (bevestigd in de bulk op de cilinderas) zouden passeren. De ontwikkeling van de straal van de bellen in tijd laat direct na het loslaten van de bodem een grote initiële condensatie zien door de grote gradiënten in de dominante parameters in de bodemlaag: Ja en de verhouding tussen de radiale snelheid van het beloppervlak en de relatieve stroomsnelheid. De snelheidscomponenten van de stijgende bellen liet zien dat de LSC de bellen horizontaal mee sleepte dicht langs de bodemplaat en een

significante afname van de verticale snelheid veroorzaakte. Wanneer de bellen eenmaal de grenslaag overstegen en buiten de regio van de sterke LSC kwamen, nam de verticale snelheid toe en bereikte bijna zijn oorspronkelijke waarde. Als de bel de bulk bereikt had, waren de condensatie en verticale vertraging constant. De verticale snelheid was minimaal één ordegrootte groter dan de karakteristieke snelheid van de LSC. De afstand vanaf de bp waar de verschillende bellen volledig condenseerden, lieten een brede spreiding zien, alhoewel de hoogte wel gecorreleerd was aan de maximale verticale snelheid van de betreffende bel.

De cycli van groei en vertrek van de bellen bij een grote hoeveelheid actieve holtes waren van bovenaf in beeld gebracht voor verschillende waarden van oververhitting (van ~ 3 tot 12 K). Het volume van de bellen nam lineair toe met de tijd en de evenredigheidsconstante werd groter naarmate de oververhitting groter was. Bij het loslaten van de bp was de gemiddelde horizontale doorsnede d_{max} van de bel ongeveer 0.5 mm voor het bereik van oververhitting van ~ 3 tot 10 K bij het gebruik van de silicium plaat met $l = 0.6$ mm; d_{max} was maximaal ongeveer 0.65 mm bij de grootste waarden van oververhitting voor de geïsoleerde bellen zonder interactie en minimaal ongeveer 0.4 mm voor de laagste waarden van oververhitting en $l = 1.0$ mm.

Op het moment van vertrek leek de vorm van de bel op een vallende druppel, maar dan ondersteboven. Het volume van de bellen bij vertrek bleef onder de helft van het verwachte maximaal bereikbare volume V_{max} wanneer het vertrek van een sferische bel alleen bepaald werd door de oppervlaktespanning en het drijfvermogen en thermische effecten verwaarloosd werden. Een warmtestroom de bel in, kleiner dan een bepaalde kritieke waarde, zou de oorzaak kunnen zijn dat de bellen in de experimenten, die in dit proefschrift gepresenteerd worden, kleiner zijn dan V_{max}.

Het gemiddelde interval tussen twee achtereenvolgende vertrektijden, dus de inverse van de vertrekfrequentie, nam exponentieel af als de oververhitting groter werd en hing niet af van de afstand tussen de holtes. Voor een lagere oververhitting werden de fluctuaties rondom het gemiddelde tijdsinterval tussen twee achtereenvolgende vertrekkende bellen groter, wat de onregelmatigheid van het vertrekproces laat zien. Voor een gegeven oververhitting gold dat hoe groter de afstand tussen de holtes was, des te onregelmatiger de bellen vertrokken. Grotere afwijkingen van de gemiddelde vertrekfrequentie werden in verband gebracht met fluctuaties in de temperatuur in de nabije vloeistof, wat meer invloed had op de geïsoleerde bellen dan op de bellen die omgeven waren door andere groeiende bellen. Dit was in overeenkomst met de observatie die gemaakt is in hoofdstuk 2 dat, voor een gegeven waarde van oververhitting, bij een grotere afstand tussen de holtes het makkelijker was voor een actieve nucleatieplek om inactief te worden.

Er waren drie factoren die bijdroegen aan de toename van warmteoverdracht per tijdseenheid door het kokende oppervlak: (1) de latente warmte voor de groei van de bellen, (2) microconvectie als gevolg van de verstoring van de thermische grenslaag door de groei van de bellen en veroorzaakt door zowel het kielzog van vertrekkende bellen als de kortstondige geleiding die nodig was om de thermische grenslaag, waar de bel vertrok, te herstellen en (3) de toename in de effectieve drijfstroom gecombineerd met de latente warmte van de bellen werden meegevoerd door advectie. In hoofdstuk 3 was de gemiddelde latente warmte per tijdseenheid, die benodigd was voor de groei van dampbellen op een enkele nucleatieplek, berekend met behulp van

de vertrekfrequentie en het volume van de bel op het moment van vertrek. De relatieve bijdrage van de latente warmte aan de toegevoegde warmte van het oppervlak per actieve nucleatieplek bleek een toenemende functie van oververhitting, die kon oplopen tot 25%. Verder bleek dat de absolute bijdrage van het effectieve drijfvermogen toenam bij oververhitting, aangezien het volume van de bel niet veranderde over het bestudeerde domein, en dat de vertrekfrequentie exponentieel groeide bij oververhitting. De resultaten in dit proefschrift hebben bijgedragen aan een beter begrip van de verschillende mechanismen die verantwoordelijk zijn voor de toename van de warmtestroom door nucleatie van dampbellen in RB convectie. De goed gedefinieerde LSC die gevisualiseerd is in de 2-fasestroming kan in detail bestudeerd worden door de stroomsterkte en dynamica te meten als een functie van de oververhitting om te zien hoe deze zich verhouden tot de situatie zonder aanwezigheid van bellen. De omwenteltijd van de LSC kan gebruikt worden om een karakteristieke snelheid te krijgen die vergeleken kan worden met de snelheid van de stijgende bellen. Verder zou het interessant zijn om de afhankelijkheid van het getal van Reynolds voor de oververhitting te onderzoeken in vergelijking met de 1-fasestroming. Deze experimenten worden reeds uitgevoerd in ons laboratorium. Het zou ook interessant zijn om de stroming te onderzoeken onder verschillende waarden van een constante temperatuurverschil, dus waarden van ΔT, terwijl de oververhitting gevarieerd wordt, wat zou leiden tot het vergroten van het domein van het getal van Rayleigh dat tot op heden onderzocht is (1.4×10^{10} - 2×10^{10}). De limiterende factor voor het verhogen van de oververhitting is de snelheid van condensatie die, wanneer deze niet groot genoeg was, leidde naar opbouw van damp in de cel, wat ervoor zorgde dat het systeem niet in een stabiele staat raakte. Een grotere ΔT maakt het mogelijk om een groter domein van oververhitting te onderzoeken, aangezien men kan verwachten dat de thermische grenslagen dan een groter temperatuurverschil beslaan dan dat hier in dit proefschrift bestudeerd is ($\Delta T \simeq 16$ K) en dat dampbellen die van een oppervlak met een hogere oververhitting vertrekken in de bulk een temperatuur tegenkomen die laag genoeg is om de stijgende bellen compleet te laten condenseren. In beschouwing nemende dat grotere waarden van oververhitting leidden tot een grotere toename van de warmtestroom, zou men kunnen verwachten dat men op deze manier grotere toenames van warmtestroom voor grotere ΔT zou kunnen bereiken.

Een andere interessante parameter om te onderzoeken zou de aspectverhouding zijn van de cel. In 2-fasestroming zou een kleinere aspectverhouding inhouden dat de stijgende dampbellen langer de tijd hebben om volledig te condenseren voordat ze de topplaat bereiken. Dit zou betekenen dat, voor een gegeven ΔT, met een kleinere Γ een groter domein van oververhitting bereikt kan worden zonder dat experimentele beperking van damp opbouw in de cel bereikt wordt. Zodoende kan men de studie voortzetten naar volledig ontwikkelde nucleatie in een RB cel.

Acknowledgements

I am very grateful to my supervisors Guenter Ahlers, Detlef Lohse and Chao Sun for giving me the opportunity to do this research and for their guidance, support and encouragement throughout my Ph.D.

I want to thank Guenter for welcoming me into his laboratory at the University of California, Santa Barbara (UCSB). Throughout the nearly four years I spent here, your comments were always very insightful and helped me gain a deeper understanding of the experiments. I really admire your dedication, enthusiasm for new discoveries, thorough thinking and vast knowledge. I have learnt many things from you, which have made me a better experimentalist, and I am glad you insisted I learn to use the machines in the shop to make myself parts for experiments. As you said several times, this is an important skill that diversifies what one can do as an experimentalist.

Thank you Detlef for having me as part of the Physics of Fluids (PoF) group and providing many of the means needed for my experiments. In our discussions, you always pointed out interesting physics, which served as inspiration and triggered my curiosity. I admire your varied and interesting research with collaborators all around the globe, without which my Ph.D. project would not be what it is today. I learnt much from the discussions you, Guenter and I had when you visited us in Santa Barbara.

Thank you Chao for all the discussions we had in spite of living in different time zones and for your guidance, support and friendship. Your input and feedback helped me see aspects of the experiments that were crucial for this thesis. Your support kept me going in the toughest times of my Ph.D. I admire your sharpness and experimental expertise, and I always enjoy your joyful character. I am really thankful to have had you as a supervisor during both my MSc. and Ph.D. projects.

I would like to thank all the members of my graduation committee who took the time to read my work and give me feedback.

To my paranymphs and friends Julieta Matos Castaño and Rianne de Jong, thank you for being there with me on the day of my defense. It is great to have you as friends and confidants. Since the very early stages of our friendship, you have been caring and supportive and in spite of the distance and busyness of Ph.D. life, our connection has remained very strong.

I would like to thank my colleagues at UCSB, Stephan Weiss, James Hogg and Ping Wei. Stephan and James helped me get started with my experiments and were always willing to answer questions. Also, thank you Stephan for showing me the beautiful hike to Cathedral Peak. After Stephan and James left I was the only person in the lab for a couple of months so when Ping joined the group from Hong Kong as a postdoc I was very happy. We shared our views of the world and I learnt many

things about Chinese culture which I found fascinating. Ping, thank you for all your support and kindness and for cheering me up when my wafers broke or something else went wrong in the lab. I enjoyed talking to you about our projects and results. I admire your capacity for work and your knowledge about turbulent Rayleigh-Bénard convection.

I am grateful to the students I had the opportunity to work with and mentor. Thank you Daniel Suto for choosing the project I proposed for the Research Mentorship Program. This program provides high-school students from around the world a hands-on summer research experience in a wide variety of topics. This program motivated me to design and build an apparatus, and the first tests were done together with Daniel. Thank you Tai Rodrig, computer science undergraduate student at the UCSB College of Creative Studies (CCS), for your valuable input to my image analysis code. I am also grateful to the physics undergraduate students at the UCSB CCS, Tomek Fraczek and Chris Reetz, who helped me build the apparatus and made sure it worked as it was intended to. Your enthusiasm and creativity inspired me and it was great to see our joint effort be transformed into a paper yet to be published.

Special thanks to my colleagues at PoF, Federico, Sander W. and Enrique, who helped me arrange things in the Netherlands while I have been in the U.S.A, and who have supported and shared their Ph.D. experiences with me.

I want to thank Paul Hoefnagels, a master's student from PoF, who is doing his internship in our lab at UCSB. Paul, first of all, thank you very much for translating the summary of my thesis. I have enjoyed working with you and am very glad that you are continuing the research on boiling Rayleigh-Bénard convection.

I would also like to acknowledge the personnel at the Institute for Terahertz Science and Technology at UCSB. Rob Marquez, Rita Makogon and Elizabeth Strait were always friendly and helpful when it came to visa issues, paper work and computer problems. On the other side of the world were Joanita Leferink, Gert-Wim Bruggert, Martin Bos and Bas Benschop also kindly giving me a hand whenever I contacted them. Thank you all.

I want to thank the highly experienced machinists at the UCSB Physics Machine Shop, Jeff Dutter, Doug Rehn, Guy Patterson, Andy Segale and Mark Sheckherd for the very many parts that they made for my experiments. They were always very efficient, friendly and willing to rush a piece when it was urgent. A special thanks to Guy who runs the student's machine shop and taught me all I know about these machines. I am also grateful to David Prine and Daniel Stack who run the Department of Physics store-room at UCSB. They were always kind and willing to help.

This thesis would not have been what it is without the love and support of my dear family and friends. I am very grateful to my parents, Yolanda Guzmán and Manuel Narezo, who have always taken care of me and supported me in my decisions. In spite of the vast distances between where we live, you have been very close to me. The same goes for my brother Pablo, thank you for your excellent advise throughout my Ph.D., with every conversation I moved a step forward. You made me see things that I had believed impossible, to be possible. Madre, Padre, Pablo, Lisa y Martha: gracias por venir desde lejos para estar conmigo en esta ocasión tan especial.

A very special thank you is reserved for my partner Daniel; thank you for always being there for me without exception and for your understanding and care. Your

personal support and scientific insight over the last three years have been invaluable in helping me carry out my Ph.D. Together with you, the years in Santa Barbara have been some of the happiest of my entire life and this amazing adventure shall continue.

Thanks to my friends for the experiences, interesting discussions, adventures, hikes, travels, shows, and many other dear memories we share. My days in Santa Barbara are memorable thanks to Christine, Dave, Tomás, Eddie, Julián, Sarah, Devin, Ali, Lisa, Eric, Antonio, Kelsey, Lili, Olivia, Alejandra, Ana, Nicole, Monze, Austin, Brenda Velázquez, Jade, Will, Kim, Max, Yanitsa, Sergio, Yunuen, Lola, Natalia, Angélica, Pablo, Unai, Paula, Christian K., Melika, Bruno, Alaina, Thomas, Niva, Netta, Sarah and David Lunn, JJ, Kaila, Christian P., Saemi, Justin, Maximilian, Jasin, Chelsey, Renato, Olaf, Bruno and Sofia. To the people who came to visit from other parts of the world, thank you for sharing precious time with me: Andrea, Sylvia, Ingrid, Susanna, Rosa, Nadia, Adriana y Sergio, Niki, Steffi, Christian S., Stephan, Cathy, my parents, and finally Pablo and Lisa, together with meine liebe kleine Martha!

About the author

Daniela Narezo Guzmán was born in Mexico City. As a child, she enjoyed learning and doing homework but also getting into mischief with her friends. Childhood career aspirations included becoming a marine biologist and then through her love of reading, to study literature and write her own books. A great physics teacher during high school changed this and it became absolutely clear that she was going to go to the Universidad Nacional Autónoma de México (UNAM), where her parents had also studied, to get a physics degree. She had never learnt such a fascinating subject in her entire life. Her interest in fluid dynamics originated through her love of music and interest in acoustics. Her Mexican degree (licenciatura) thesis subject was the nonlinear propagation of waves in a slide trombone resonator.

Daniela knew she wanted to do her master's research project in the Physics of Fluids group, at the University of Twente, so excited for new places and experiences, she arrived in the Netherlands. Through the master's program she learnt many things about fluid dynamics, among which experimental techniques became the one she turned most to her advantage. Her master's thesis was an experimental study on the crucial role of bubble deformability for strong drag reduction in bubbly turbulent Taylor-Couette flow. Daniela was then given the opportunity to continue her experimental work with the Physics of Fluids group while being able to enjoy much warmer weather than that of Northern Europe. She joined Prof. Ahlers group at the University of California in Santa Barbara where she conducted her Ph.D. work, as a joint graduate student between both research groups.

In her free time she likes visiting nature, climbing, running, practicing yoga, dancing, reading, cooking, listening to music, and being with family and friends.